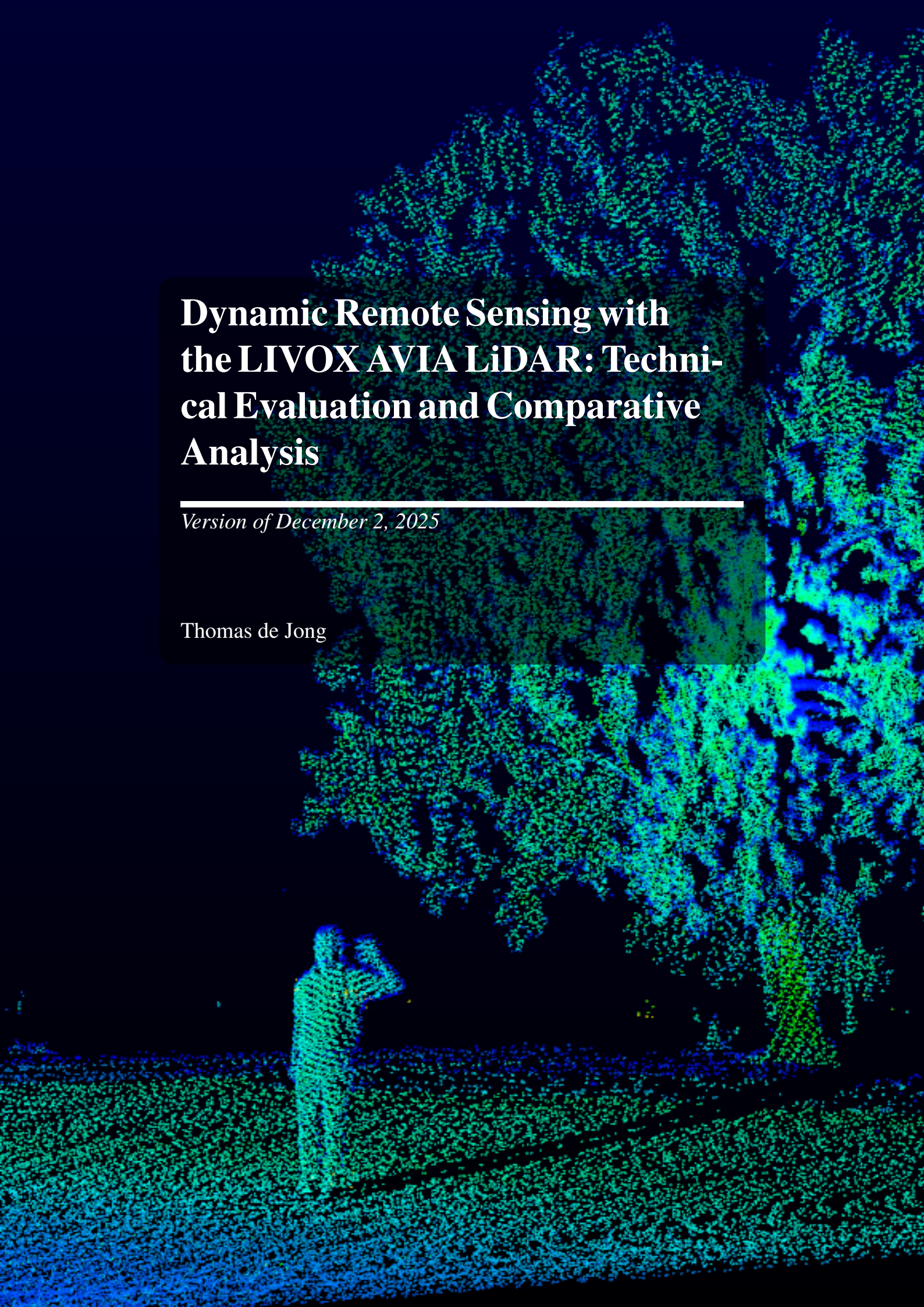

Dynamic Remote Sensing with the LIVOX AVIA LiDAR: Technical Evaluation and Comparative Analysis

Version of December 2, 2025

Thomas de Jong

Dynamic Remote Sensing with the LIVOX AVIA LiDAR: Technical Evaluation and Comparative Analysis

THESIS

submitted in partial fulfilment of the
requirements for the degree of

MASTER OF SCIENCE

in

APPLIED EARTH SCIENCE

by

Thomas de Jong

Faculty of Civil Engineering and Geosciences, Delft University of Technology
Delft, the Netherlands
Project Duration: January 2025 – December 2025

Dynamic Remote Sensing with the LIVOX AVIA LiDAR: Technical Evaluation and Comparative Analysis

Author: Thomas de Jong
Student id: 4825136

Abstract

Compact, affordable LiDAR sensors such as the Livox AVIA offer new opportunities for autonomous monitoring of dynamic natural environments. This thesis evaluates the Livox AVIA's suitability for static, manual, and stand-alone applications in environmental sensing. The research investigates the added value of the Livox AVIA by assessing its real-world performance, testing and validating manufacturer specifications, and developing a portable monitoring setup tested on wind-induced tree motion and beach morphology changes.

A series of controlled field-based experiments is conducted to measure field-of-view (FOV) coverage, point-density distribution, range precision, and sensitivity to vibrations. Python tools are used to estimate FOV coverage and density over time, while PCA-based plane fitting determines the distance random error at 20 m. Additional analysis tests the influence of external forces causing vibrations and assess long-term stability using data from the Internal Measurement Unit (IMU). To achieve practical deployment, a portable Central Observations Recorder (COR) integrating a Raspberry Pi controller, power management, and anemometer connectivity is designed, developed and tested. Time series derived from point clouds are processed into 3D motion fields using PlantMove to analyse tree displacement patterns in order to showcase the AVIA's dynamic scanning capabilities.

Results show that the AVIA achieves approximately 92% FOV coverage within 1000 ms (contrasting the manufacturer's 800 ms claim) and maintains high range precision ($\sigma \approx 0.8$ cm at 20 m), exceeding stated specifications. Point density is found to be strongly non-uniform over the FOV, with the central half of the FOV exhibiting a roughly 2.4 times higher density. Small, irregular vibrations increase range noise by less than 1 mm, while airborne particles and heavy precipitation further reduce return intensity and point density. Scans made with hours of time in between showed negligible drift between them, confirming the sensor's stability for longer-term monitoring setups.

Overall, the findings demonstrate that the Livox AVIA is a reliable, precise, and low-cost LiDAR sensor that can be used for near to mid range (2–100 m) static environmental monitoring. When appropriately configured and keeping in mind its non-uniform FOV density and full FOV coverage time, the system performs effectively in both manual and autonomous operations for monitoring dynamic processes.

Thesis Committee:

Chair:	Dr. R.C. Lindenbergh.
Second supervisor:	Dr.ir. S. de Vries
Committee Member:	D. Hulskemper

Preface

When I planned my first meeting with Roderik, to ask about interesting thesis topics, I had not imagined I would be walking out of the meeting with the small LiDAR scanner my entire thesis would end up being about. It was a great experience to think about and shape the topic of my research at the start, and throughout the work I have had amazing opportunities to meet new people, plan and go on numerous fieldwork trips and even present my work at Virtual Geoscience Conference in Lausanne.

I would like to thank Roderik and Daan for their guidance and time, the conversations during our meetings were very helpful and something I looked forward too every week. I also want to thank Sierd for his help, feedback, our nice talks and bringing me along to the beach at the start of my thesis to show me, and help with putting together one of the fieldwork plans.

For the inspiration end help on the work involving the moving trees, I would like to thank Steven, whose ideas and research helped with visualizing the data. I am also thankful for the experience of the people at the WaterLab who helped with thinking about and putting together parts of the electronics.

Between starting in January until the end in December, a lot of things have happened in my life. I have had some amazing new experiences as a result of my thesis, and thanks to the support of my family and friends I have been able to really try my best and enjoy it, even during the harder times.

Thomas de Jong
Delft, the Netherlands
December 2, 2025

Contents

List of Figures

Chapter 1

Introduction

The remote sensing of dynamic natural environments is a rapidly evolving field, where advancements in sensor technology enable more detailed and efficient data collection. LiDAR (Light Detection and Ranging) sensors have been widely used for various environmental monitoring applications, offering high-resolution 3D point clouds that capture the structure and movement of natural elements. Traditionally, LiDAR systems have been used to measure static environments, such as landscape mapping [1] or hydrographic surveying [2], but there is a growing interest in using their capabilities for monitoring dynamic phenomena like their use in self driving cars or robotics.

This paper will focus on two dynamic applications: the movement of trees in response to environmental factors and morphological changes on beaches. Monitoring these dynamic processes will require sensors that can operate autonomously, stay reliable over extended periods, and maintain accuracy and precision in challenging outdoor environments. These requirements highlight the need for compact, energy-efficient LiDAR setups that can sustain long-term operation in remote or exposed field sites.

In the past decade, LiDAR technology has seen a lot of development aimed at different applications [3]. This led to the development of more compact, cost-effective systems like the Livox AVIA sensor (see Figure 1.1), a small form-factor LiDAR sensor the faculty has recently acquired. Unlike traditional bulky and expensive LiDAR systems, the Livox AVIA can offer a more accessible solution for easy to work with and portable setups resulting in it being used in more widespread applications.

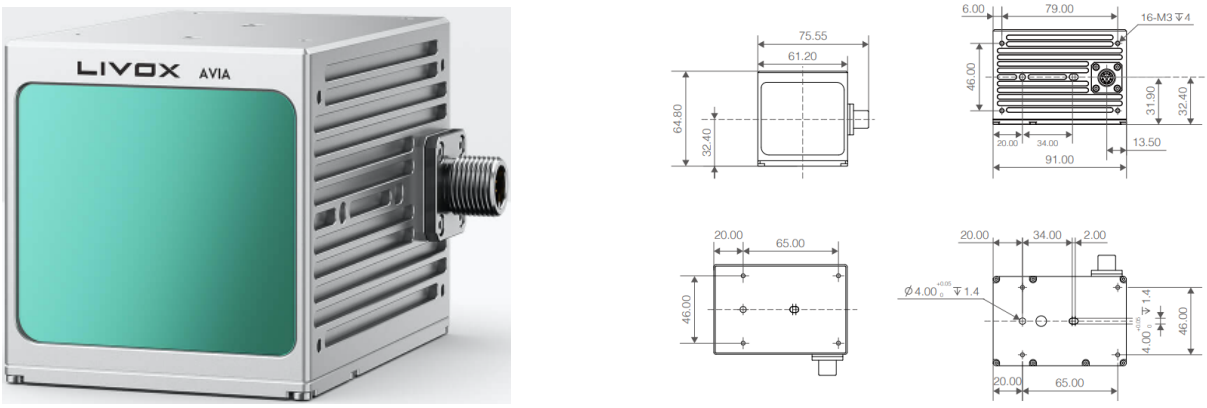

(a) Livox AVIA LiDAR sensor

(b) Livox AVIA Dimensions

Figure 1.1: Livox AVIA LiDAR sensor and its dimensions [4].

The relevance for this thesis is based on the growing trend of smaller, more affordable LiDAR systems and the necessity of understanding how to optimise their use in practical real-world applications. Like for example done in this dynamic portable setup using an AVIA sensor [5] for dynamically mapping caves or urban areas. Or a static autonomous setup for monitoring snow depth variations in an avalanche release area [6], which would normally be difficult and expensive to do with larger sensors at hard to reach locations.

With cheap LiDAR sensors like the AVIA becoming more common, understanding their capabilities and limitations is required to find out their potential in measuring challenging environmental settings. The EC&T faculty, currently owns a second AVIA sensor that can be found in the 'Yellowscan Mapper plus' drone attachment [7] and has been used, for example, by Brandwijk (2023) [8]. This however is not a stand-alone sensor as a drone is required to use and operate it. It means that a validation helping to understand the AVIA's limitations and added value for its use in various environmental applications is still required. The sensor's specifications and affordability make it a promising candidate for applications that require prolonged stand-alone operation in remote or vulnerable locations where theft or damage to expensive equipment is a concern. The exploration of its potential as a well understood and versatile piece of equipment for measuring dynamic environments forms the core motivation of this thesis.

The general rise in development, production and popularity of small LiDAR sensors highlights the importance of assessing models like the Livox AVIA. While most larger terrestrial LiDAR scanner deployments focus on static applications like landscape or infrastructure mapping, this paper aims to investigate specifically how the AVIA performs in measuring terrestrial dynamic environments. Furthermore, it will look at the practical challenges and configurations necessary to optimise the sensor's performance in these stand-alone setups. The ability of the AVIA to deliver high quality point-clouds, while offering advantages like portability and cost-effectiveness is significant for its broader adoption in more studies.

Despite its promising design and specifications [9], questions remain regarding the AVIA's real-world practical accuracy, especially when subjected to less ideal field conditions like external vibrations or in varying environmental factors like wind and rain. This research therefore addresses the challenge of determining whether compact LiDAR sensors can function as reliable tools for monitoring dynamic natural environments. By validating how the AVIA's factory specs like operational range, range accuracy, and IMU capabilities compare to inside and outside conditions, this work establishes a clear picture of the sensor's practical performance. In addition to assessing the AVIA on its own, a comparison of its design and capabilities with other LiDAR systems provides context for its position within the broader terrestrial LiDAR landscape. Together, these evaluations identify where the AVIA performs as specified, where its limitations emerge, and how it can be effectively configured for manual and stand-alone terrestrial scanning. This not only evaluates the AVIA's added value for the faculty but also helps with the development of affordable and self-contained LiDAR systems that are capable of monitoring dynamic environmental processes.

1.1 Research Questions

Main research question:

What is the added value of the LIVOX AVIA LiDAR sensor for terrestrial application in *dynamic* environments?

Sub-questions:

1. How do the factory-provided specs compare to the real-world performance?
This question motivates the need to verify whether the AVIA performs as advertised when used in expectable inside and outside conditions. By testing manufacturer specifications like accuracy, coverage rate, and range it becomes possible to find out if the sensor can be used for dynamic environmental monitoring.

2. What are the main use cases for the AVIA sensor in environmental sensing applications?
This question helps with finding applications for which the AVIA is most suitable, by looking at how the technical and physical characteristics influence its applicability. Answering this sub-question will evaluate the AVIA's characteristics and help identify its usefulness across different environmental monitoring tasks.

3. How do environmental factors like vibrations influence the performance and accuracy of the AVIA?
This question investigates the stability of the sensor in outdoor conditions. By considering how environmental factors have an influence it becomes possible to understand real-world limitations and necessary mitigation strategies.

4. What are the practical requirements for deploying the AVIA in *static* setups for capturing *dynamic* environments?
This question helps examine how to setup and configure the AVIA for stable monitoring in dynamic outside environments and will make it possible to make setup recommendations.

5. How does the AVIA's design compare with other LiDAR systems in similar use cases?
This question evaluates the AVIA relative to existing terrestrial laser scanners, identifying scenarios where the sensor offers advantages or faces limitations. The comparison will help clarify position of the AVIA with these other terrestrial laser scanners.

1.2 Thesis structure

In Chapter 2 the current state of terrestrial laser scanning is introduced followed by a coverage of the AVIA's specifications. Chapter 3 describes how the factory specifications will be analysed and discusses the influence of environmental factors on the AVIA. Next to this it introduces the fieldwork studies, the related workflows and the tools that were created for these data processing workflows. To help with making, debugging and improving the overall clarity of my Python scripts, I made use of AI assistance. In Chapter 4 the results of the specification and environmental influence analysis are discussed followed by the results of the fieldwork studies. Chapter 5 summarises the overall findings and goes over the found strengths and limitations of the AVIA. Finally, in Chapter 6 the thesis is concluded, the research questions are answered and final recommendations for future work are given.

Chapter 2

Background

2.1 Terrestrial Laser Scanning

Like stated in the introduction, LiDAR technology has experienced a lot of development over the past decade, big drivers have been the automotive and robotics industries [10], where compact, lightweight, and high-frequency scanners are essential to for example act as digital eyes. These advancements have made LiDAR scanners smaller, faster, more power-efficient and a lot more affordable, enabling new applications that were previously impractical or impossible with traditional surveying Terrestrial Laser Scanners (TLS). Traditional TLS systems are capable of achieving millimetre-scale accuracy over large field-of-views (FOV) at long distances [11, 12], whereas automotive/drone-grade units like the Livox AVIA [9] prioritise high temporal resolution and compact form factors, at the expense of measurement noise, resolution, and FOV.

Existing work and manufacturer provided specifications show that these two types of scanners each have clear strengths but also distinct shortcomings when used in dynamic environmental monitoring. Large TLS provide the accuracy needed to measure subtle environmental change but are slow, heavy, and generally unpractical for repeated or long-term deployments in dynamic and remote environments. In contrast, small fast scanners from the automotive or robotics sectors can scan at higher temporal resolution and be deployed almost anywhere, but typically offer lower precision and non-uniform coverage. Whether the gap between these systems can be bridged and whether the smaller faster scanners can be adapted for dynamic environmental monitoring is the motivation for this research.

Traditional Terrestrial Laser Scanners

Terrestrial Laser Scanners are proven tools in surveying, geomorphology studies, and structural monitoring. Their strength are producing highly accurate, high-density point clouds at ranges of up to thousands of metres. Modern TLS instruments such as those developed by RIEGL or Leica reach millimetre precision at 50–100 m [11, 12]. However, these capabilities come at the expense of portability and speed, a single full 360° scan typically requires minutes to complete, making TLS impractical for capturing fast environmental dynamics or motion. TLS units are also bulky, power hungry, expensive, and require stable mounting, limiting their suitability for rapid or autonomous deployments in exposed or hard to reach environments. TLS are highly effective for static and structural measurements but less feasible for monitoring processes that evolve over seconds to minutes.

Recent (Terrestrial) Laser Scanners

In contrast to current common TLS, LiDAR scanners developed for automotive or robotic applications are designed for continuous and fast data acquisition as they are usually mounted on moving platforms [13]. These scanners have become smaller, cheaper, and a lot more accessible to use and work with, recent studies show these smaller LiDAR units being used more and more for scientific monitoring purposes. For example in [14] where they installed an AVIA on a fixed mount to perform permanent scanning of a target area. They found the AVIA captured geomorphic changes comparably to a high-end RIEGL VZ-2000i TLS, demonstrating that the smaller and cheaper AVIA can compare to the more expensive TLS. The open-source SDKs and software for the new generation of LiDAR scanners makes it a lot easier to develop custom deployments. Other field trials support this potential [6, 15]. In short, initial research indicates that newer cheap and fast LiDAR scanners can suffice for many monitoring tasks, albeit generally with larger noise and narrower FOV coverage than TLS.

However, a gap can be noticed, the monitoring of dynamic environments ideally requires the precision and reliability of TLS, but also the speed, efficiency, and portability of modern automotive or robotics-grade scanners. Current TLS systems are too heavy and slow for repeated high-frequency scanning, while small fast LiDAR scanners lack the uniform coverage and accuracy required for detailed environmental analysis. Moreover, automotive and robotics LiDAR units are not developed with the goal of static monitoring of dynamic environments, meaning that their default operating modes, mounting configurations, and software ecosystems do not directly support these applications.

This motivates the development of a setup that takes advantage of these newer LiDAR units, making use of the small size and power-efficiency, and being capable of rapid repeated scanning with sufficient point density. Such a system should provide:

- Fast consecutive scans suitable for 4D (space + time) monitoring
- Sufficient accuracy and point density for this dynamic analysis
- Ease of use and deployment, even in remote environments
- Compact and portable hardware with autonomous operation capabilities

It shows the need for a dedicated setup that uses the strengths of a compact LiDAR scanner while understanding its shortcomings. The system developed for this thesis aims to fill this need and evaluate whether specifically the Livox AVIA can be reliably used for dynamic environmental monitoring tasks that were otherwise impractical or impossible with the use of traditional TLS.

2.2 Livox AVIA Background Information

In this section, the Livox AVIA scanner and its specifications will be introduced, starting with an explanation on its main purpose and use case according to Livox.

The AVIA is a small and lightweight LiDAR scanner that is manufactured by Livox, a Chinese company that develops a range of different 3D LiDAR scanners. A large part of their scanners is developed

specifically for the automotive and autonomous robotics industry. However, most of their products can also be utilised for other applications, like how the AVIA will be used in this thesis.

The AVIA falls under Livox' "Industrial-Grade LiDAR" range according to the Livox AVIA webpage [16], and is advertised mainly for applications such as: Power line surveying, forest surveying (drone bound), mobile mapping (Simultaneous Localization and Mapping or SLAM) and for use in smart city projects (static setup, dynamic monitoring). The main selling points are: A large unit production size, its eye safe certification and a self declared 'high work to cost efficiency' (performance to price ratio).

Real life use cases are the aforementioned examples like the SLAM system and snow depth monitoring setup [5, 6]. Other cases include: robot mounted systems that help the AVIA map buildings and sites [16] or drone bound terrain surveying [8].

In the manual that is provided for the AVIA, a list of specifications and internal components is provided. This list can also be found on the Livox website [9]. In the paragraphs below some specifications and components from this list will be discussed and examples will be provided.

2.2.1 Points Per Second (PPS)

Starting with the amount of PPS the AVIA is able to measure. The AVIA emits 240,000 individual laser pulses per second (at a wavelength of 905 nm), meaning that it is capable of measuring up to 240,000 PPS. By looking at the return signal of the laser pulses, it is possible to increase the amount of PPS measured. This is possible because sometimes part of the initial signal continues further and is then reflected by a second or even third object. This can be seen in Figure 2.1 which shows how single and multiple return modes work.

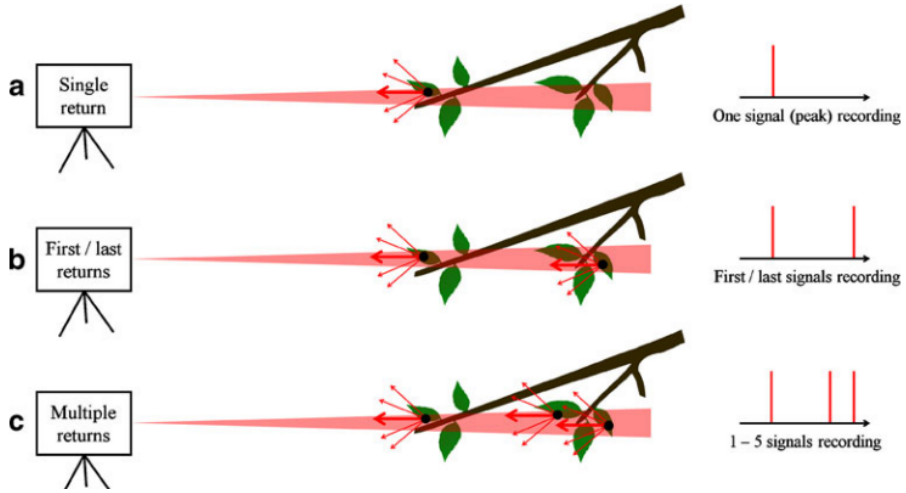

Figure 2.1: Different LiDAR return modes [17]

The number of PPS that can be measured, generally depends the on return mode that is used. The AVIA can use 4 different return modes, Single First, Single Strongest, Double and Triple return. It must be noted that the provided amount of PPS that can be measured, is under ideal circumstances. This is because if a emitted pulse does not return back, it is not registered/measured. As an example: if 1000 pulses are emitted and only half return, although it 'can' measure at 1000 PPS, in reality the resulting data will only include the returned 500 points.

Furthermore, if a higher return mode it used, but all the signal is returned by the first object hit, there cannot be any second and third returns, which also results in a lower real value of PPS than what is theoretically possible. The optimal number of PPS the AVIA can measure with its different return modes can be seen in Table 2.1 below.

Table 2.1: AVIA's Optimal Point Rate for Different Return Types

Return Mode	Point Rate
First or Strongest Return	240,000 points/s
Dual Return	480,000 points/s
Triple Return	720,000 points/s

2.2.2 Scan Mode

Next to the different return modes that the AVIA can use, there are 2 distinct scanning modes the AVIA can utilise, these are the Repetitive and Non-Repetitive scanning patterns. The coverage of the 2 modes can be seen in Figure 2.2.

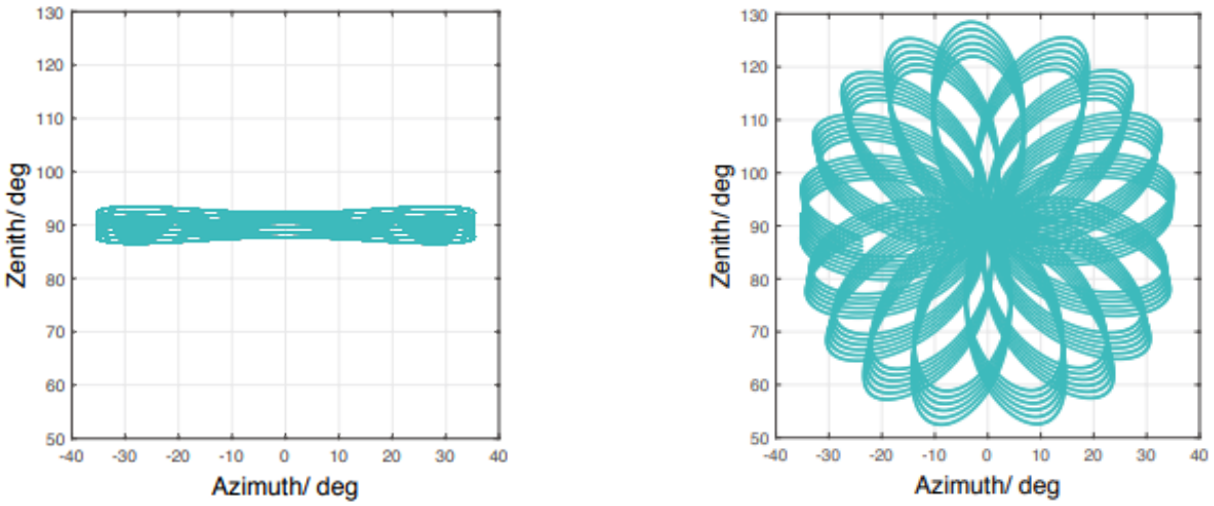

(a) Repetitive scanning pattern

(b) Non-Repetitive scanning pattern

Figure 2.2: AVIA scanning patterns (images from the Livox manual [4])

The repetitive scan mode has a repeat cycle of 0.1 seconds, while the non repetitive scan mode has no exact repeat cycle and draws a slow counter-clockwise rotating flower-shaped pattern (like a Risley Prism Scanner, as discussed by A. Ortiz et al. [18] and V. Duma er al. [19]). Both scan modes have a set Field of View (FOV) in which points can be measured, the repetitive scan mode is smaller than the FOV that is used for the non-repetitive scan mode. The effective FOV of the AVIA is 70.4° horizontally and 77.2° vertically, but for the repetitive scanning mode the vertical FOV is squished down to between 4.5 and 6.8°.

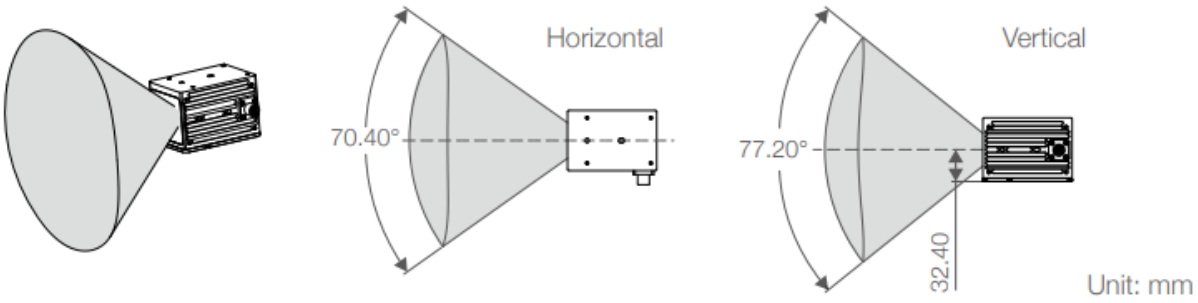

Figure 2.3: The effective FOV of the AVIA using the Non-Repetitive scan mode (image from the Livox manual [4])

Table 2.2: Scan Mode Characteristics

Scan Mode	Repeat Time	FOV Dimensions
Repetitive	0.1 s	70.4° (H) & $4.5 - 6.8^\circ$ (V)
Non-Repetitive	–	70.4° (H) & 77.2° (V)

The coverage of the FOV for the non-repetitive scan mode depends on the total scan duration, as it takes time for the pattern to rotate over the FOV and cover the entire area different parts of the FOV require more time to be covered than others. This is shown in Figure 2.4 below. Livox calculates its coverage percentage using Equation 2.1 [20, Section 2.1]:

$$C = \frac{\text{Total area illuminated by laser beams}}{\text{Total area in FOV}} \times 100\% \tag{2.1}$$

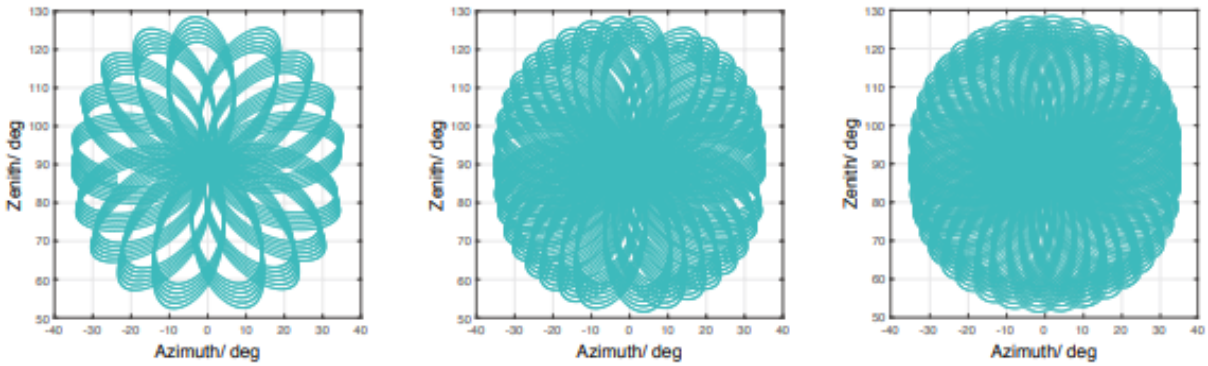

Figure 2.4: Scan duration VS FOV coverage (image from the Livox manual [4])

2.2.3 Scan Quality

The scan accuracy of the AVIA depends on several parameters that affect the precision of the distance and angular measurements. One main parameter is the distance random error (DRE). This error indicates the uncertainty in distance measurements; for example, when the AVIA measures a target at a distance of 20 meters, the random error follows a normal distribution, meaning that approximately 68% of the measurements (corresponding to 1σ) will be within 2 centimetres of the actual distance.

Another important parameter is the angular random error, which describes the variations in the measured angles due to noise or mechanical factors. With an angular random error of $1\sigma < 0.05^\circ$, the measured angles will closely match the true angles within this small uncertainty range.

Finally, the beam divergence of the laser defines how much the beam spreads as it travels. For the AVIA, the vertical beam divergence is 0.28° while the horizontal beam divergence is only 0.03°, indicating a wider spread vertically than horizontally. This divergence plays a role in the effective footprint of the laser beam at various distances and will help with understanding the FOV coverage.

Table 2.3: Scan Quality Specifications

Parameter	**Specification**
Distance random error (1σ at 20 m)	< 2 cm
Angular random error (1σ)	$< 0.05^\circ$
Beam divergence	0.03° (H) & 0.28° (V)

2.2.4 Detection Range

The maximum detection range of the AVIA is provided for 2 illuminance examples, at 0 lux and at 100 kilolux (klx). Outside on a bright summer day an illuminance close to 100,000 Lux or 100 klx can be achieved [21], perfect darkness describes a 0 lux environment. The optimal detection range of the AVIA for these examples as provided by Livox can be shown in Table 2.4 below. Showing that in complete darkness the AVIA should be able to detect up to 130 meters further than during a bright day. It also becomes clear that the reflectivity of a scanned object has a big influence on the detection range as well. Lastly, the scanner has a minimum detection range, objects closer than 2 meters can be distorted, and below 1 meter the scanner is 'blind' [4].

Table 2.4: Detection Range at Different Illuminance Levels

Detection Range	**10% Reflectivity**	**20% Reflectivity**	**80% Reflectivity**
0 klx	190 m	260 m	450 m
100 klx	190 m	230 m	320 m

2.2.5 Inertial Movement Unit (IMU)

The AVIA's internal IMU has a frequency of 200Hz which means the data is updated 200 times per second, it houses an accelerometer and a gyroscope, with these it can measure its movement and determine its orientation. Gyroscopes are used to measure the AVIA's rotational velocity and the accelerometers

measure linear its acceleration along one of the 3 axes that can be seen in Figure 2.5. The IMU is the 'BMI088' manufactured by Bosch, the resolution and noise density of the BMI088 can be found on the Bosch website [22] and can be seen in Table 2.5.

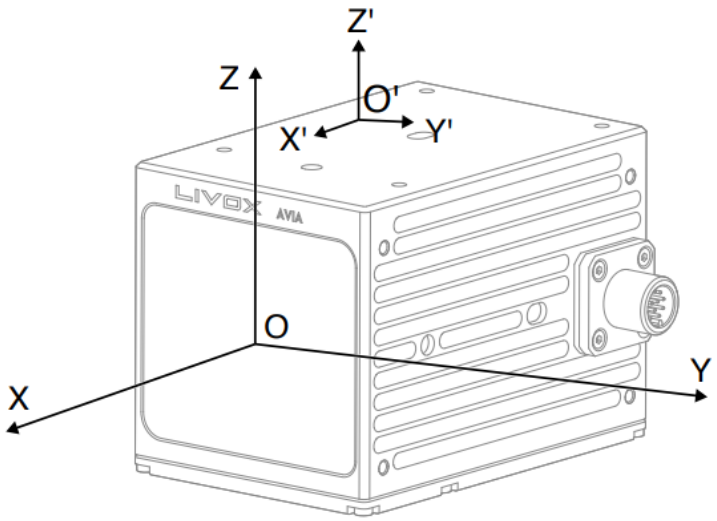

Figure 2.5: Orientation of the X', Y', Z' axes of the AVIA's internal IMU (image from the Livox manual [4])

Table 2.5: IMU Resolution Specifications

Parameter	**Accelerometer**	**Gyroscope**
Nominal Resolution	0.09 mg	0.004 °/s
Noise Density	175 μg/$\sqrt{\text{Hz}}$	0.014 °/s/$\sqrt{\text{Hz}}$

The nominal resolution indicates the smallest measurable change in acceleration in milli-g (where g = gravitational acceleration $\approx 9.81 m/s^2$) for the accelerometer. While for the gyroscopes this unit is angular rate in degrees per second. The noise density indicates how much background "static" is present in the IMU's readings over a range of frequencies by measuring the inherent noise level per unit of bandwidth. So, the noise density shows the practical smallest detectable signal for the accelerometer and the gyroscope. By filling in the IMU's update frequency into the provided noise density specs this can be calculated for both the gyroscope and the accelerometer:

$$\text{Accelerometer: } \frac{175\mu g}{\sqrt{Hz}} = \frac{175}{\sqrt{200}} = 2.475 \text{ milli-g} = 0.02427 m/s^2 \tag{2.2}$$

$$\text{Gyroscope: } \frac{0.014\ ^\circ/s}{\sqrt{Hz}} = \frac{0.014\ ^\circ/s}{\sqrt{200}} = 0.19799\ ^\circ/s = 0.00346\ rad/s \tag{2.3}$$

Chapter 3

Methodology

This chapter outlines the methodology and can be divided into two main parts. The first part, Sections 3.1 and 3.2 focus on the validation of the performance of the AVIA through a series of controlled tests, to establish its capabilities and limitations before deploying it in dynamic environments and to compare the provided specs with the normal use test results.

The second part, Sections 3.3 and 3.4 introduce the developed setup, the fieldwork, and the corresponding data processing workflows. Together, these sections describe how the system was deployed, built and analysed.

3.1 Analysing the Livox AVIA Specs

This section describes the method of how the specifications provided by Livox will be compared with the real-world performance of the AVIA sensor. Short tests and developed Python scripts are used to analyse the specs, the impact of environmental influences to provide a better understanding of the capabilities of the AVIA.

The tests aim to validate a selection of key specifications from Section 2.2, relevant to the intended application of the AVIA for the scanning of dynamic scenes. These include the maximum Points Per Second (PPS), the Field of View (FOV) coverage time in non-repetitive scan mode, point density uniformity, scan quality at a specified operating range, and detection limits under varying conditions and distances.

The specifications provided by Livox, are listed in Table 3.1 and offer valuable guidelines. However, they are likely derived under controlled (ideal) conditions. In practice, external factors such as surface reflectivity, ambient lighting, scan angle, vibrations and distance can significantly influence sensor performance [23].

The purpose of the analysis is not only to confirm whether the provided specification numbers can be achieved, but also to get a feeling for using the sensor and to understand how and why the sensor performs differently in real-world scenarios. Where applicable, references are made back to the background chapter and the specifications in Table 3.1 for clarity the results of the described methods can be found in Chapter 4. The section structure follows the order of the specs table.

Table 3.1: Livox AVIA Sensor Specifications [9] [22] (Combined Overview)

Category	Specification	Value
Point Rate & Returns	Single return (First or Strongest)	240,000 points/s
	Dual return	480,000 points/s
	Triple return	720,000 points/s
Scan Modes	Repetitive mode repeat cycle	0.1 s
	Non-repetitive mode repeat cycle	–
Field of View (FOV)	Repetitive FOV	70.4° (H) $\times$ $4.5-6.8^\circ$ (V)
	Non-repetitive FOV	70.4° (H) $\times$ 77.2° (V)
Scan Quality	Distance random error (1σ at 20 m)	< 2 cm
	Angular random error (1σ)	$< 0.05^\circ$
	Beam divergence	0.03° (H), 0.28° (V)
Detection Range	**0 klx** @ 10% reflectivity	190 m
	0 klx @ 20% reflectivity	260 m
	0 klx @ 80% reflectivity	450 m
	100 klx @ 10% reflectivity	190 m
	100 klx @ 20% reflectivity	230 m
	100 klx @ 80% reflectivity	320 m
IMU (BMI088)	Update frequency	200 Hz
	Accelerometer nominal resolution	0.09 mg
	Accelerometer noise density	$175\,\mu g/\sqrt{Hz}$
	Gyroscope nominal resolution	0.004°/s
	Gyroscope noise density	$0.014^\circ/s/\sqrt{Hz}$

3.1.1 Point Rate & Number of Returns

As mentioned in Subsection 2.2.1, there can be a significant difference between the maximum number of Points Per Second (PPS) the sensor is capable of emitting and the number of returns actually recorded. In the case of the AVIA, it became clear during data processing that when a laser pulse fails to return, the corresponding point is still logged but with coordinates (0, 0, 0) and an intensity of 0.

This explains why, when using the Livox Viewer, the software includes all emitted pulses in its PPS count, regardless of whether a valid return was received. As a result, the displayed PPS value reflects the theoretical maximum, not the actual number of meaningful points captured. In practice, this means the initial point cloud appears much larger than it truly is. Independent of the return mode, and depending on scanning conditions, large percentages of points need to be discarded due to being (0, 0, 0) entries.

When using the AVIA LiDAR sensor in triple return mode, it is possible to distinguish the return number of each point during post-processing. This means that even though the scan was performed in triple return mode, it is possible to replicate the results of dual or single first return modes afterward.

While this results in larger data sets (more points), it also offers greater flexibility and control during processing, allowing users to choose the most suitable return configuration retrospectively.

Overall, since the return mode can be in a way 'selected' during processing (with the exception of strongest-return mode), scanning in triple return mode provides the most comprehensive data and the widest range of processing options.

3.1.2 Non-Repetitive Scan Mode FOV Coverage

The focus of this subsection is on the non-repetitive scan mode, it will be used as the default operating mode of the AVIA as it is the most relevant for typical scanning applications. Unlike repetitive scanning, which follows a fixed pattern, the non-repetitive mode continuously varies the laser beam path, enabling full FOV coverage over time.

Since the manufacturer specifies that the AVIA should achieve 100% FOV coverage within 800 ms in this mode [9], verifying this claim provides valuable insight into the sensor's practical performance, particularly when the goal is to capture data at higher temporal resolutions. To assess this, a Python script was developed to calculate the FOV coverage based on the sensor's laser beam footprint and measured point coordinates of a flat surface.

FOV Coverage Percentage

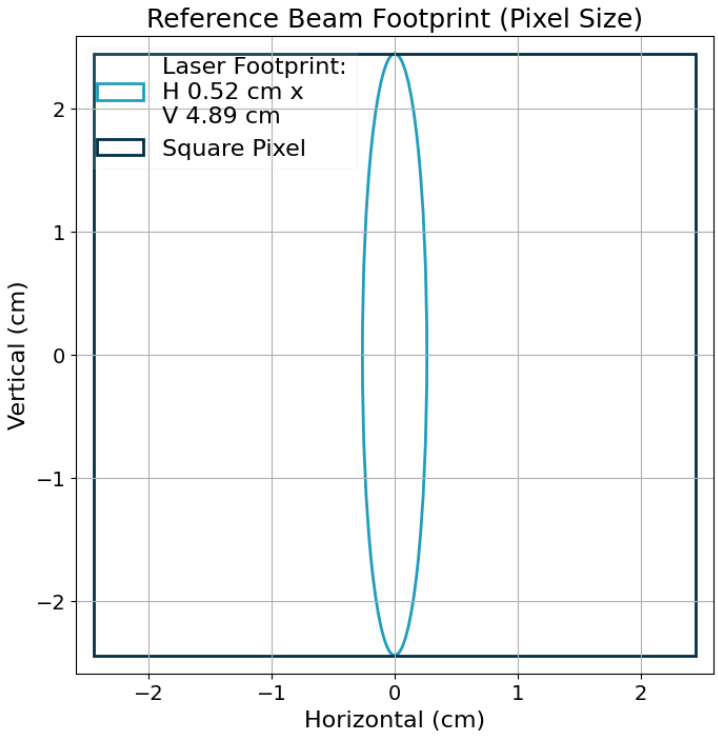

Figure 3.1: Laser beam footprint of the AVIA at 10 meters

The FOV is discretised into a grid with square "pixels" whose side lengths equal the laser beams elliptical footprint, specifically, the largest diameter (based on the semi-major axis) at a given distance. By using the given laser divergence angles it is possible to calculate that for example, at 10 m the AVIA's beam footprint has a semi-major axis of 2.44 cm and a semi-minor axis of 0.26 cm (Figure 3.1). It must be noted that the square pixel simplification does overestimate the horizontal beam width by nearly a factor of 10, the real footprint is a narrow ellipse meaning that the model will predict a quicker coverage.

The script reads the coordinates from a flat-surface scan (obtained by scanning the ceiling at a distance of 2.21 m) *.las* file, from which each recorded point on this surface is assigned to a corresponding pixel on a grid. As soon as a pixel contains at least one point, it is marked 'covered'. By going over all the points in the scan file, it is then possible to calculate the percentage of covered pixels over time.

In order to calculate the FOV coverage %, another ellipse was created using the FOV divergence angles of the AVIA (Table 2.2). This revealed that the actual scan data extends slightly beyond this fitted ellipse at the edges (see Figure 3.2), indicating that the AVIA has a marginally larger FOV than this 'perfect' ellipse. For consistency however, the perfect ellipse was used when computing percentage coverage, which in turn will slightly overstate actual coverage.

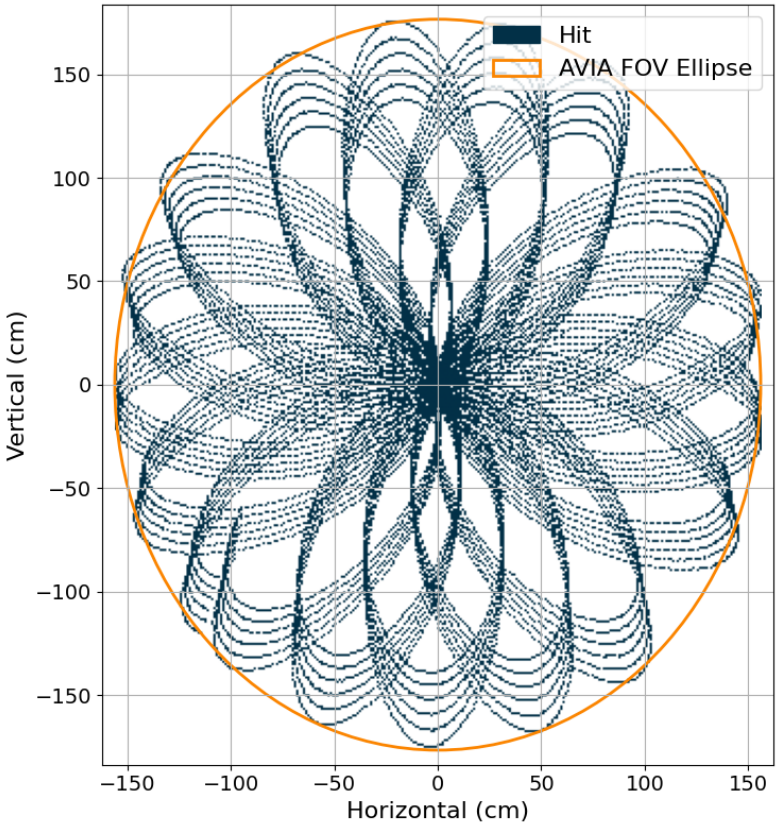

Figure 3.2: AVIA FOV grid-coverage example

The results will be compared with Livox' own method described in the Wiki [20, Section 2.1], next to this the coverage percentage was also calculated using thin rectangular pixels that perfectly fit around the laser footprint (instead of square ones). This is expected to provide a more realistic understanding of the coverage but does differ from how Livox calculates the coverage. The results and discussion on the FOV coverage percentage can be found in Section 4.1.1.

Pattern Development Over Time

To visualise how the AVIA's non-repetitive scan pattern develops during a scan, plots are made using the same scan data as before where the scanned points are coloured sequentially by acquisition time and plotted into the FOV pixel grid. With this method, plots with representative timestamps (50 ms, 500 ms, 1000 ms) are created to show how the pattern slowly covers the FOV. The results of this analysis are shown and discussed in Section 4.1.1.

FOV Point Density Heatmap

To analyse the spatial distribution of 'hit' points within the FOV over time, heatmaps were created using the ceiling scan data. The FOV coverage ellipse is discretised using the same pixel grid as in the coverage analysis, and for each pixel the number of returns accumulated during the scan is recorded to be able to see which areas of the FOV obtain the most hits.

The heatmaps were produced for several timestamps between 100 and 5000 ms to illustrate how the point density develops during a scan and they are shown in Section 4.1.1. These heatmaps can be used in further assessment of the spatial variations in point distribution across the FOV.

FOV Point Density Distribution

The uneven point distribution property is important to consider for applications requiring consistent point density, so that the scan duration or scanner orientation can be adjusted. To find out how uneven the points are distributed, the FOV was divided into 50 elliptical rings with equal thickness (Figure 3.3. Using the same flat surface scan data as the sections above, the number of points in each ring is computed. For each ring, the area is calculated so that the point density in Points Per Square meter (PPm2) can be derived. The resulting PPm2 values are visualised in Section 4.1.1 using both a logarithmic-linear histogram and a 3D surface plot to show how the point density varies over the FOV.

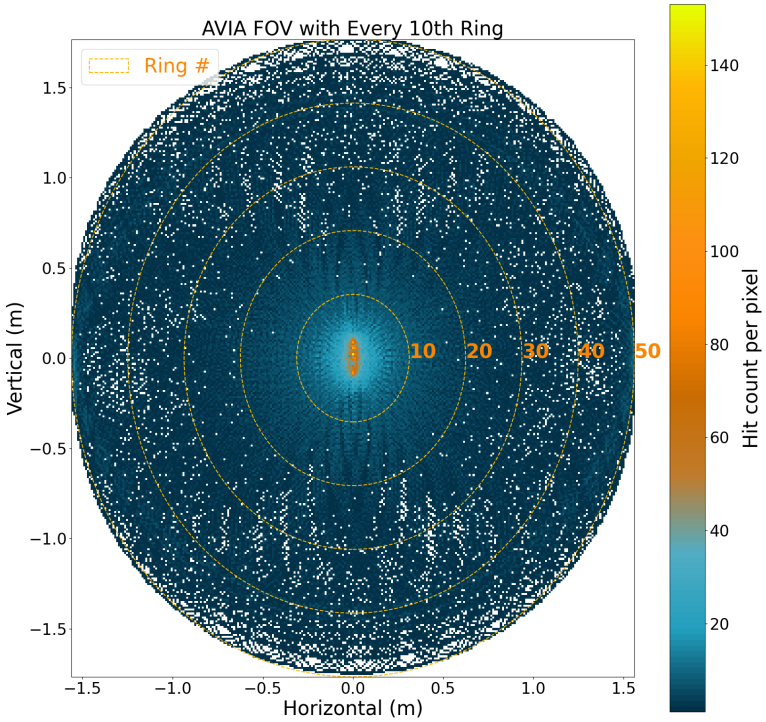

Figure 3.3: FOV plot showing every 10th ring

Regional FOV coverage percentages

The non-uniform point distribution of the FOV coverage could be taken advantage of by applications that require higher temporal resolutions. As the centre region of the FOV obtains a higher amount of 'hits' per unit of time, higher temporal scan resolutions can be achieved by considering only points from this region. A smaller region around the FOV centre will achieve a near 100% FOV coverage way before the entire FOV is covered meaning that although the FOV coverage footprint will be much smaller, higher temporal resolutions can possibly be achieved.

In order to figure out if it is possible, the initial FOV coverage Python script is adapted so that the coverage percentages and durations for circular regions within the FOV could be easily calculated. The radius of the circular regions is determined by taking a percentage of the semi-minor axis of the original AVIA FOV. In Figure 3.4 the size of circular regions ranging from 20% to 80% of the overall FOV are shown so that their scales can be understood.

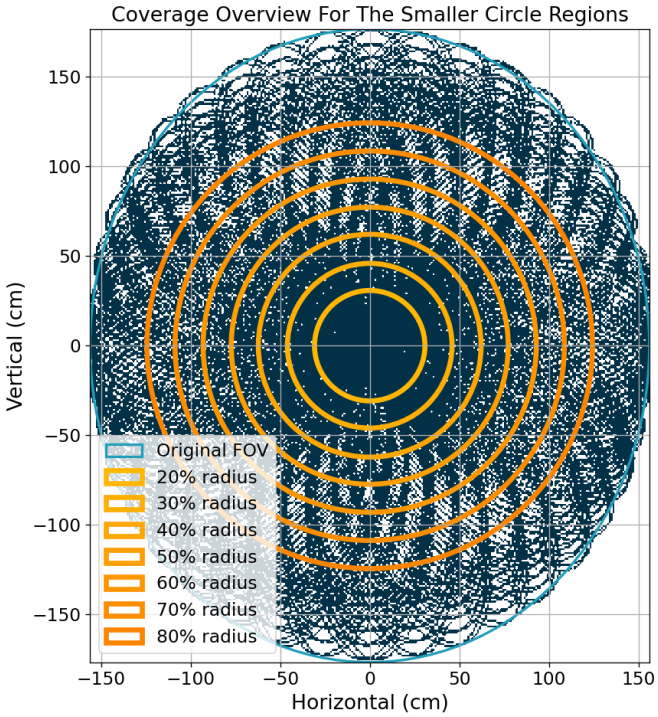

Figure 3.4: Overview showing the size of the different circular regions

For each region size, the script calculates the number of pixels covered over the duration of the scan using the same method as the coverage time calculations defined at the start of the chapter. Using the results, coverage vs time curves could be plotted for each region to assess how the region size influences the coverage time. In addition to the coverage time plots, a parameter selection diagram was made to relate region size, coverage threshold %, and achievable temporal sampling frequency with each other. The diagram makes it possible to figure out the possible temporal resolution for each region size at a given threshold limit and can be found in Section 4.1.1.

3.1.3 Scan Quality

Distance random error

To evaluate the specified Distance Random Error (DRE) found in Table 2.3, a test is conducted with as goal to determine whether the advertised level of precision could be reliably achieved in an uncontrolled environment, and to assess whether distance noise varies across the AVIA's FOV.

A standard tripod was used to mount the AVIA scanner, for a target, a TE109 Logarithmic Gray Scale Test Chart (see Figure 3.5b) was used for to its planar surface and geometry. The chart was positioned at 20 meters from the scanner.

To assess the uniformity of the DRE across the FOV, multiple scans were made with the target placed at different positions: the center, 50% and 75% offsets towards the right edge, with similar steps downward toward the bottom edge of the FOV as can be seen in Figure 3.5a. The goal is to test whether the DRE increases further away from the center, possibly due to angular distortion or signal degradation at the edges.

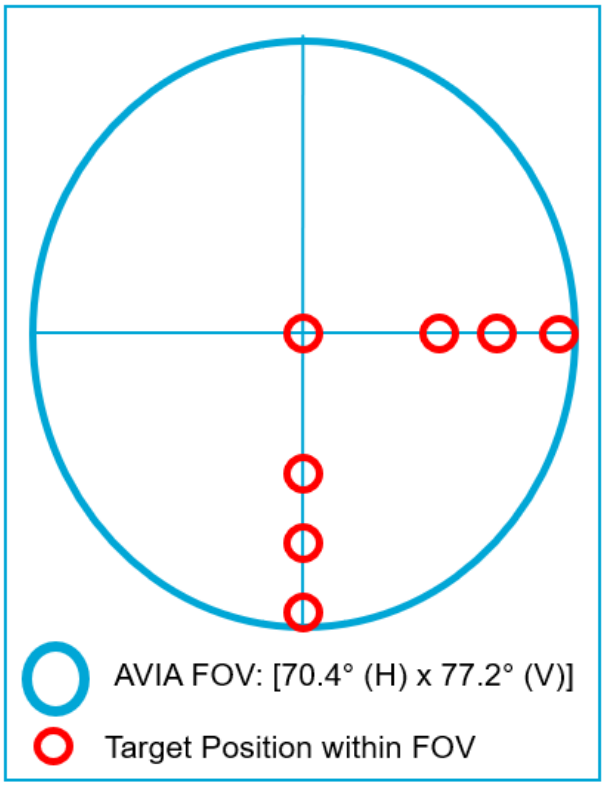

(a) Position overview of target placement within the FOV

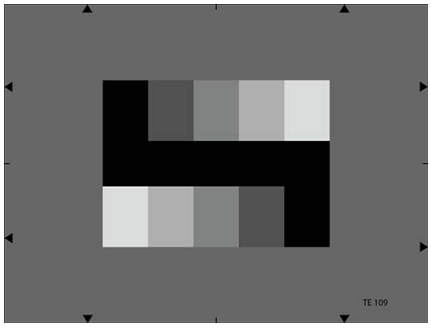

(b) TE109 Logarithmic Gray Scale Test Chart (dimensions: 36.5 cm × 30.5 cm) [24]

Figure 3.5: Target positions and target example

To do this, first a Principal Component Analysis (PCA) is performed to estimate an initial best-fit plane through the scanned points, significant outliers (+20 cm) are removed. A second PCA is then applied to the filtered dataset to obtain a refined plane estimate (an example is shown in Figure 4.10a). Finally, the beam-direction (radial) residuals, representing the difference between the measured distance and the ideal distance to the fitted plane are calculated. These residuals reflect range measurement accuracy along the scanner's line of sight. The standard deviation of the residuals is reported as the measure of DRE. After calculating the DRE values, 3D visualization of the points and their fitted planes and histograms of the centered radial errors are created which can be found in Subsection 4.1.2.

3.1.4 Point Density and Footprint Size over Distance

To assess how the AVIA's general point density decreases with increasing distances, theoretical point density values were estimated for a 1 second scan time. By using the same method to calculate the Points-Per-Square-meter (PPm2) as the FOV coverage analysis (Section 3.1.2), the average density was computed across the full FOV and separately for the both the inner and outer 50% FOV regions.

The laser beam footprint size at increasing distances was derived using the specified horizontal and vertical beam divergence angles (Table 2.3). These footprint size estimates can be used to provide context for interpreting coverage at longer distances.

All results are discussed and visualised in Subsection 4.1.3, using a log-linear PPm2 vs distance plot to show the point density change over distance and a footprint-size vs distance plot to indicate the actual dimensions of the footprint at ranges up to 200 meters. These visualisations support the later analysis of the sensor's effective operational range and expected spatial resolution at different distances.

3.1.5 Detection Range

While using the AVIA throughout this thesis, a lot of scans were acquired at many different locations. Although a specific range test was not directly performed, as a result of these other tests, findings about the detection range and some specific scanner characteristics while in the field can be discussed.

The assessment of the AVIA's scan range focuses on identifying the distances until which returns are common. It looks at the number and characteristics of the returns at higher distances and considers factors that could influence the detectability of objects at higher distances, such as the effect of beam divergence and incidence angles.

In addition to the outside observations, a controlled experiment was performed in a long corridor of the faculty basement to investigate how the AVIA's elongated footprint affects the representation of distant objects. Two orange cones (Figure 3.6) were placed 90 m from the scanner with one wrapped in reflective tape to so that different reflectivities could also be considered. The cones were scanned twice, once with the AVIA in its standard upright orientation, and once rotated 90° around its optical axis. This allowed comparison of directional footprint effects on point density and apparent object geometry. Hit counts and object shapes in both orientations were examined in CloudCompare to quantify distortion patterns. The results from the detection range analysis and test can be found in Subsection 4.1.4.

Figure 3.6: A comparable example of the cones that were used in the range test

3.2 The Influence of Environmental Factors

Understanding how external conditions affect LiDAR measurements is essential when using the AVIA in outdoor environments. Factors such as mechanical vibrations, illumination, and airborne particles (rain, dust, or snow) [25] could all occur during a scan and can each influence the accuracy of point cloud data. By analysing both empirical tests and literature findings, this section aims to describe how these factors influence the results and if/how these effects can be mitigated or anticipated in practical deployments.

3.2.1 Vibrations

The specs of the internal IMU are defined in Subsection 2.2.5. By understanding the IMU's resolution and noise density, the measured rotational velocity and linear acceleration can be used to assess the influence on point cloud data quality by external vibrations. While the AVIA is mounted somewhere outside, it is expected that external forces like the wind cause small vibrations. Initially the best way to mitigate these vibrations is to ensure the AVIA is mounted to a rigid and solid platform. However, this might not be possible at all times, so having an understanding on how vibrations influence the scan quality will give an idea of what to expect when using the AVIA in less than perfect conditions.

One thing to point out is that the AVIA is manufactured with the option of being mounted on moving platforms. So it is expected that small fast vibrations like those caused by drone motors will not cause major disturbances.

Testing the effect of vibrations

Using the data from the internal IMU it is possible to read the orientation and movement of the AVIA every 5 ms (200 Hz). While processing the *.lvx* data, the IMU data is separated into a *.csv* file so that the data from the gyroscopes and accelerometers can be analysed and visualised. During testing, it was found that the IMU update frequency is slightly higher than the indicated 200 Hz (more between 208-220 Hz), seemingly depending on the input voltage that powers the AVIA. This is a minor but noteworthy observation that could be investigated further in future work.

Test Setup

To investigate the impact of vibrations, the AVIA was placed on a tripod and manually tapped at different intervals and magnitudes while scanning. This induced short, irregular vibrations similar to what might be expected from wind gusts or mild mechanical disturbances. IMU data was used to extract the amplitude, and duration of these motions averaged per 1 second frame. So that as a consequence, concurrent point cloud frames could be easily compared to reference frames that have the lowest measured movement. The comparison focuses on evaluating potential degradation in point cloud quality, specifically through changes in the Distance Random Error of planar targets located at fixed distances.

Processing the data

The point cloud and IMU data of a 60 second scan was cut into consecutive 1000 ms intervals, so that each frame can be associated with its corresponding IMU data chunk. From these, five 1 second frames were selected that have the highest, lowest, and most average vibration (Figure 3.7). These frames were then opened in CloudCompare, and three flat-plane regions were cut-out for evaluation (see Figure 3.8). The third cut-out is a very wide rectangle covering a large part of the FOV in order to ensure points acquired throughout the full 1000 ms are included (Figure 4.4c). The results from this test can be found in Subsection 4.2.1.

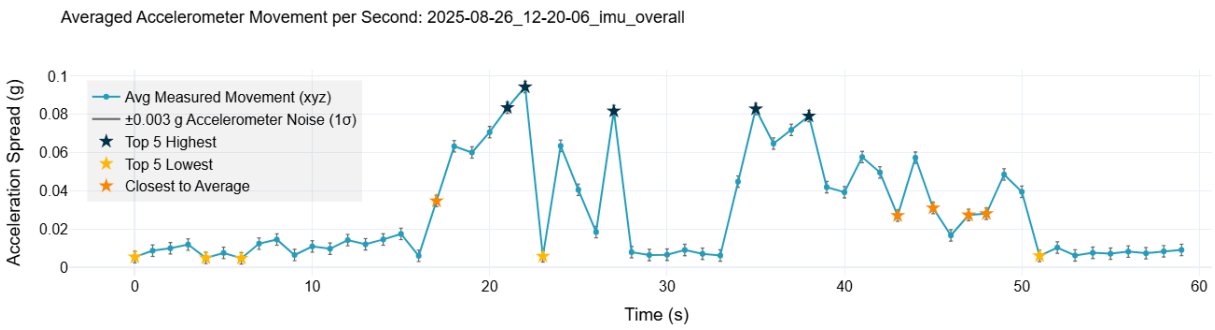

Figure 3.7: Accelerometer data used to select low, average and high movement frames

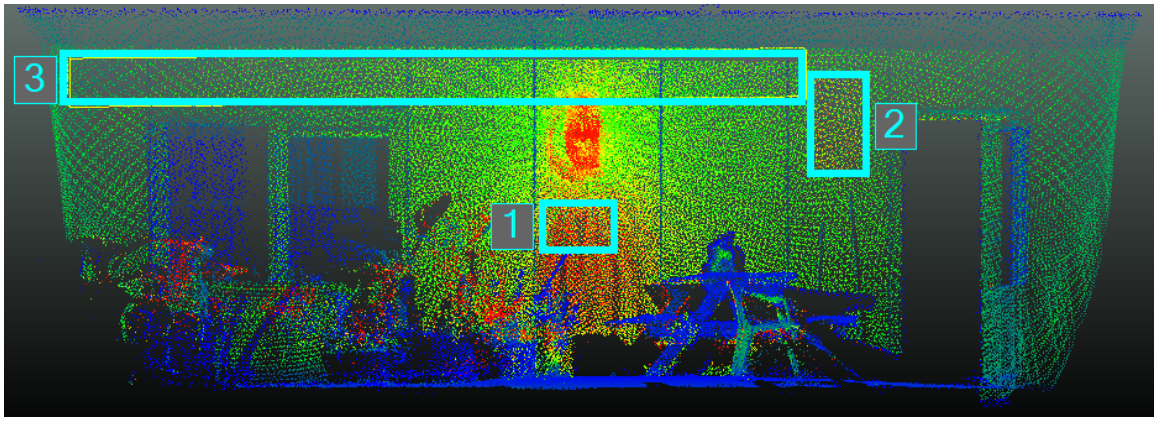

Figure 3.8: Vibration testing cut-outs

3.2.2 Airborne particles

While scanning of dynamic environments, windy (and stormy) conditions will not be uncommon during scans. So it is necessary to consider how rain, dust, and other airborne particles such as sand influence the quality of the data. These conditions can cause partial signal attenuation or scattering, reducing the number of valid returns and affecting both intensity and range accuracy.

Rain

Raindrops can scatter and absorb near-infrared laser beams, this causes signal attenuation and potential range distortion. The AVIA operates at a wavelength of 905 nm, which is more susceptible to scattering by small water droplets compared to longer wavelengths (e.g., 1550 nm). As [26, Section 3] describes, LiDAR systems using higher wavelengths generally perform better in rainy weather, as longer wavelengths penetrate raindrops more effectively, resulting in less signal loss and more stable point detection.

Experimental work on similar 905 nm LiDAR systems, such as [27], shows a consistent decrease in both the number of detected points and the returned intensity under rainfall. In tests, the intensity dropped by up to 70-80% and the number of points by as much as 95% at higher rain rates ($\approx 7L/m^2h$). Minor range variations ($<$20 cm) were observed, but no systematic bias was found, suggesting that most degradation results from signal loss rather than distance error.

The extent of attenuation depended on surface type: reflective materials maintained stronger returns, while darker, rougher surfaces such as asphalt showed greater losses. Overall, these results indicate that even moderate rain can substantially reduce point density and signal strength for 905 nm LiDAR like the AVIA. Because the sensor itself is environmentally sealed, performance limitations under rain primarily stem from atmospheric interference rather than hardware vulnerability.

Other particles

Next to rain, other airborne particles such as snow, sand, or dust can also degrade LiDAR performance and measurement accuracy. These particles differ in size, shape, and optical properties, leading to varying impacts on the emitted and returned laser signals.

The influence of dust and sand was tested by [28, Section 4.1], where they simulated airborne particles to find the effects on LiDAR data. It was found that both smaller dust and lager sand particles, cause attenuation and backscatter of the laser pulse. Higher concentrations lead to reduced point density and signal intensity from distant target objects and more "clutter points" near the scanner. Under bad conditions such as blowing sand or dust storms, the point cloud become sparser at long ranges and objects appear closer than they are, mainly due to occlusion and scattering effects.

For snow, [29] describes the performance of four LiDAR scanners during real snowstorms and found that modern sensors seem to be largely uninfluenced by snowfall. Older models recorded up to 15% of returns from snowflakes, whereas newer units showed less than 1%. Most snow related echoes occurred within 10 m of the sensors, with minimal interference beyond this range.

3.2.3 Stability Between Scans

Finally, it is important to consider how consistent the AVIA performs under repeated scanning over longer durations. In order to test this the AVIA was set up inside on a small tripod and made to perform a 2 second scan every 15 minutes for 36 hours consecutively. From this dataset 2 scans were selected that where recorded almost 9 hours apart that showed no changes in the scene.

Point cloud stability was evaluated using CloudCompare. First, a cloud-to-cloud (C2C) comparison was used to quantify geometric differences between the two scans. Then, the Fine Registration ICP tool was applied to determine the transformation needed to align one scan to the other. This made it possible to evaluate both the translational and rotational deviations between the scans.

In addition to these geometric comparisons, the data from the scanner's internal IMU was also used. For each scan, mean accelerometer readings were compared. Differences in mean acceleration were used as an additional test for detecting any small physical sensor displacements.

This combined approach allowed evaluation of both geometric and inertial consistency across repeated scans and can be found in Subsection 4.2.2.

3.3 Set-Up Design

With the information from the previous sections and chapters, a clear understanding of the AVIA's abilities and shortcomings helps to provide a base for the design of the setup and the planning of fieldwork studies to test it. Designing an effective setup for the deployment the AVIA in static configurations requires translating the research questions and the discussion from Section 2.1 into concrete technical

and operational requirements. The proposed fieldwork applications require a system practical system that is easy to use, can scan fast dynamic environments, has environmental resilience, and is capable of sufficient data throughput. The requirements and additional technical and practical considerations that emerge during development, form the basis for the final configuration.

3.3.1 The Technology Readiness Level of the Set-Up

To assess the eventual maturity of the setup, it is useful to consider its position within the framework of Technology Readiness Levels (TRLs). The TRL system, originally developed by NASA in the 1970s, provides a structured method for evaluating the development stage of a technology from basic discovery and concept validation to full commercial deployment. It is commonly divided into four overarching phases: *Discovery*, *Development*, *Demonstration*, and *Deployment*, encompassing nine discrete levels in total [30].

The AVIA itself, as a commercially available and field-proven LiDAR sensor, can be considered to be at TRL 9. However, this level only reflects the sensor as a bare unit. In practice, the AVIA requires integration into a functional platform such as a UAV, robotic platform, or static scanning station to become operationally useful. The maturity of these integrated systems can therefore vary depending on their intended use. For example, drone-mounted AVIA systems (such as those produced by YellowScan [7]) have achieved TRL 9, while more experimental configurations such as ground-based, static setups for monitoring dynamic environments are much less established and fall into lower TRL categories.

In this thesis, the focus lies on developing and validating a static deployment configuration capable of operating autonomously in dynamic outdoor environments. Existing literature shows that other 'new' setups that use the AVIA (e.g., for SLAM-based mapping [5] or snow depth monitoring [6]) operate around TRL 6–8. The goal of this work is to advance the static AVIA setup to a functional prototype stage (TRL 7–8), meaning it can be demonstrated in an operational environment with consistent performance and reliability.

3.3.2 Practical Set-up Requirements

To ensure the Livox AVIA can be effectively deployed in static configurations across diverse field environments, several practical requirements must be met. These requirements reflect both the technical demands from the AVIA and the goal to answer the research questions. The specific components selected for the system are introduced at the end of each requirement.

Computation and Control: The AVIA requires a dedicated computer to manage scan settings [9], control operations and timing, and handle data acquisition. The setup needs to include a compact computer that is capable of running the Livox SDK [31], which is needed to control the AVIA. The computer must be able to send scanning commands, store incoming data, and manage timers to allow for autonomous operation. It should also support integration of other sensors, and include basic input/output functionality for buttons and indicator LEDs.

For this purpose, a **Raspberry Pi 4B (4GB)** [32] was selected as the main controller. It provides sufficient processing power and flexibility to operate both the LiDAR and supplementary sensors while maintaining low power consumption and a small form-factor.

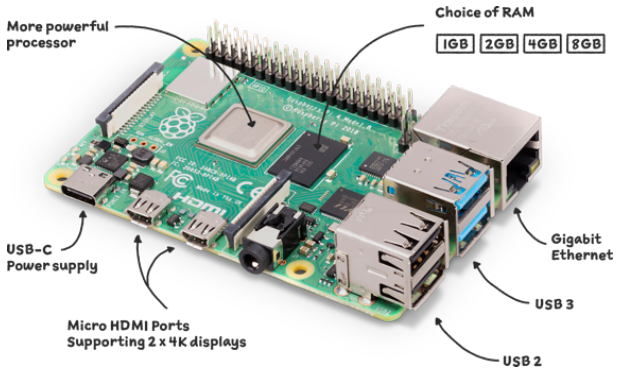

Figure 3.9: Raspberry Pi 4B [32]

Supplementary Sensors: To provide context for interpreting LiDAR data, the setup should include support for additional sensors. As many natural environment dynamics are driven by wind, an anemometer will be needed to record wind speed and direction during scans. The data can then be used together with the LiDAR measurements to link observed dynamics and morphological changes with the environmental conditions. The anemometer that was available is the **WindSonic Option 3** [33] anemometer, which can be powered by 12 V just like the AVIA and is capable of communicating with the Pi using a cheap **DB-9 RS232 to TTL converter**.

Figure 3.10: Gill Instruments WindSonic Option 3 Anemometer [33]

Power: The setup must be capable of operating independently from fixed power for extended periods. The Livox AVIA consumes approximately 10 W during scanning and about 8 W in idle mode, and the Raspberry Pi requires about 3–8 W depending on the load, the anemometer only uses ≈ 0.1 W during normal operations [9, 33, 32]. In general it will require careful power management to avoid excessive battery drain. To achieve this, the setup should include a method to completely cut power to the sensors between scans.

Both the AVIA and the anemometer require a 12 V power supply whereas a Raspberry Pi requires a 5 V source. This means that the system should be designed around either 2 individual batteries outputting these different voltages or contain a single 12 V power source (with a 12 V to 5 V converter), which would simplify the power configuration. Sufficiently large batteries should be selected to provide energy for both short duration and multi-hour to days long autonomous deployments. The power system must include appropriate regulation and protection to ensure stable operation in the field.

To achieve this, a dual-relay control board is used to independently switch power to the AVIA and the anemometer under the control of the Raspberry Pi. Power is supplied by two available external batteries: a **5 V powerbank** for the Raspberry Pi and a **12 V Power Delivery (PD) capable powerbank** for the AVIA and anemometer.

Data Storage and Management: Since the AVIA can produce up to 12.5 MB of data per second (it has a 100 Mbps port [9]) in triple return mode, the system must have sufficient and fast enough storage. The computer needs to be equipped with a fast and reliable storage device (like a USB drive or external SSD) that must be capable of writing data at speeds above 12.5 MB per second and is large enough to hold several hours of scan data without risking data loss. As data retrieval during fieldwork may not be practical, removable storage or an easily accessible data interface is required for the post-fieldwork data transfer. For collecting the acquired data, it was decided to use either the internal micro-SD card, or when available, a fast enough USB drive.

Environmental Protection: The setup must be robust enough to operate in a range of environments. While the AVIA itself is water and dustproof [9], the supporting electronics and components like the Raspberry Pi, relay board, and the power banks, are not.

Therefore, some of the components (not the powerbanks and the AVIA) will be housed within a custom **3D-printed enclosure** that provides basic protection and portability for normal conditions. For longer or more demanding deployments, the entire assembly (except for the AVIA) can be placed within an available **Peli case** [34], to ensure full protection against moisture and dust while maintaining accessibility to all the parts.

Figure 3.11: Example of the available Peli case [34] that can be used to house the non-weather proof electronics

Operational Interface: To provide flexibility for the in-field operations, the system needs to provide two distinct operational modes:

- **Manual mode** - allows the user to manually start a scan using a physical button, suitable for short-term measurements or controlled experiments (e.g., tree motion studies).
- **Autonomous mode** - enables the system to operate independently, performing repeated scans at predefined intervals for unattended monitoring (e.g., during storm events).

To do this, system and operation status are communicated via three indicator LEDs that can display power-on, scanning, idle and error states. This provides immediate user feedback and reduces the need for direct computer access during deployment.

Digital Interface: The scripts and software running on the Pi should be easily understandable, so that new users can easily change scan modes, scan settings and timers. To do this, the system should provide a clear and centralised control interface. For example, a single landing page that presents all changeable parameters in one place. From this interface, users can then modify the scan configurations and switch between manual and autonomous modes. This means that new users should be able to configure and deploy the system with minimal reading or understanding.

3.3.3 Set-up Overview

The system designed to meet these requirements is referred to as the **Central Observations Recorder (COR)**. The COR (see Figure 3.12) integrates control, data acquisition, and power management for both the Livox AVIA and the anemometer into a compact and portable unit.

The components are all mounted within a 3D-printed housing. For extended outdoor deployments, the unit can be placed inside a weatherproof Peli case. The Raspberry Pi is powered by a 5 V powerbank over its USB-C port, while the Livox AVIA and anemometer share a separate 12 V powerbank connected to a jack-plug connector. Internally, the 12 V rail is split and routed through the relays so that power to the jack-plugs for the sensors can be individually controlled. Other/extra sensors could be added but are limited to the remaining USB ports and Pi GPIO pins, meaning that sensors that cannot connect to these cannot be simultaneously connected in this configuration.

Figure 3.12: Rendered example of the Central Observations Recorder

When all the components are connected (the powerbanks, COR, and the 2 sensors) the final setup will follow the structure of the diagram below. This figure shows how everything is connected with each other.

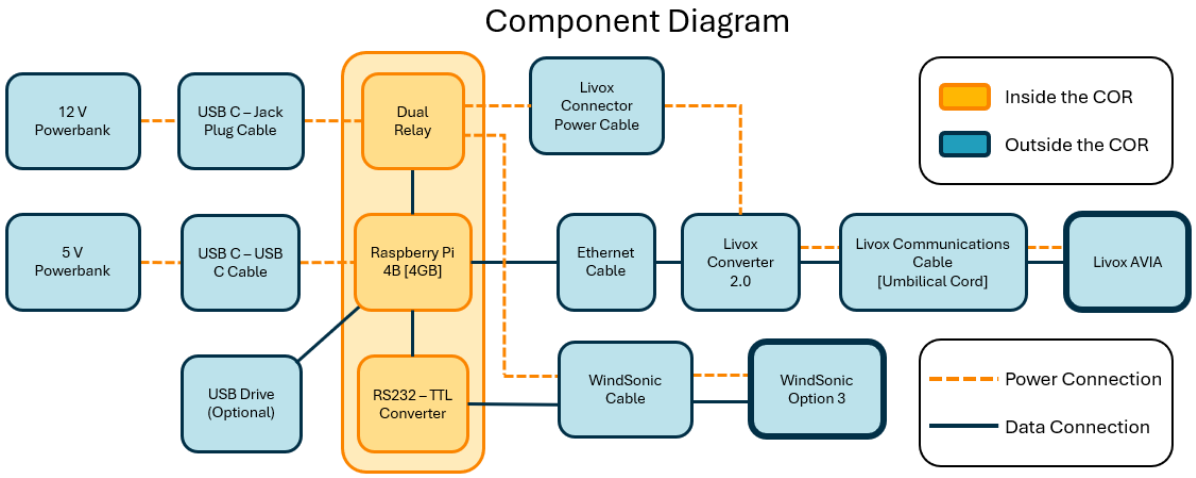

Figure 3.13: Overall setup component diagram

3.4 Setup Prototype Validation

With the setup finished, in order to be able to answer the main research question: ”What is the added value of the LIVOX AVIA LiDAR sensor for terrestrial application in dynamic environments?”. The fieldwork plans involve setting up the AVIA statically and having it scan dynamic environments. The resulting data and products derived from this can then be used to examine the AVIA’s value and performance compared to other LiDAR systems.

3.4.1 Fieldwork Plans

In order to test and validate the created setup, two fieldwork plans are considered, ”Wind Induced Tree Movement” and ”Morphological Changes On The Beach”. The subsections below will introduce these plans and motivate why they were selected.

Plan 1: Wind Induced Tree Movement

The first fieldwork plan focuses on assessing how trees move and deform under varying wind conditions. This plan was inspired in part by the ongoing research of Steven van der Linden on urban large eddy simulations [35], which raised the question of how to accurately model and represent the dynamic response and deformation of trees to wind. The AVIA’s high temporal resolution and continuous scanning capabilities likely make it well suited to investigate this phenomenon.

The primary aim of this plan is to explore the temporal deformation of trees and to determine whether the AVIA can capture the subtle changes in structure and motion. Field measurements will be performed during windy conditions, with the AVIA positioned to continuously scan an individual tree, typically around one minute per scan. The resulting point cloud recording can be segmented into discrete frames (of a specific duration, like 500 or 1000 ms), effectively making a “LiDAR video” of the tree’s motion.

These temporal frames, will be analysed to investigate if tree deformation is primarily internal (e.g., bending of branches) or external (e.g., the tree swaying as a whole) and whether this can even be mea-

sured at all. Furthermore, the data can help investigate whether it is possible to infer wind direction, or even approximate wind speed, based on the pattern of motion observed in the LiDAR data. To support this analysis, an anemometer will need to be deployed alongside the scanner to record wind speed and direction throughout the measurements. This will provide an external reference, enabling a direct comparison between wind conditions and the observed deformation behaviour.

To strengthen the results, the plan includes scanning different trees under varying wind conditions. This will allow for comparative analyses of movement patterns, providing insight into how different tree-shapes and structural configurations respond to wind. The findings could contribute both to improving the modelling of vegetation in urban climate simulations and to validate the AVIA's potential in capturing rapid environmental dynamics.

Plan 2: Morphological Changes On The Beach

The second proposed fieldwork plan focuses on the monitoring of morphological changes on the beach. Beaches are highly dynamic environments where rapid changes in morphology can occur over timescales of seconds to hours [36], particularly during high wind events or storms. However, capturing these changes is practically and logistically challenging, as conventional methods such as drone based scanning are not feasible during stormy conditions due to safety and flight restrictions. Furthermore, existing terrestrial LiDAR scanner setups are large, heavy and not always sand and water-proof [12, 11].

The first phenomena that will be looked at is aeolian sand transport [37] it is uncertain if the AVIA is able to measure airborne sand particles reliably, but its fast scanning capabilities are promising enough to try and test this.

The second plan is to deploy the AVIA in a static configuration to provide a practical alternative to drones for data collection of slower (minutes to hours) morphological changes under windy conditions. The AVIA will need to be configured to operate autonomously, performing repeated scans at fixed intervals (for example, every 15 minutes, or even every minute if higher temporal resolution is needed). So that the resulting time series of point clouds can be used to examine the spatial and temporal patterns of erosion and deposition within the measured area. By comparing successive scans, it will be possible to quantify surface change, identify zones of active sand transport, and estimate rates of morphological change.

To better interpret the influence of wind on these changes, an anemometer could be installed near the scanner. This would provide concurrent wind speed and direction data, allowing a more direct comparison between wind forcing and the morphological responses observed in the LiDAR data.

This plan serves two main purposes, first to assess the feasibility of using the AVIA in harsh coastal conditions and second, to evaluate its performance in capturing and quantifying surface changes over time. The results will help determine the AVIA's potential for use in dynamic geomorphological monitoring where environmental conditions limit more conventional measurement methods.

3.4.2 Data Processing Workflows

With the acquired fieldwork data, from the 2 different dynamic environments, the next step is processing everything in order to get results. To make the processing of the data as efficient as possible, workflows were created to help.

Plan 1: Wind induced tree movement

The initial part of the wind induced tree movement fieldwork is the collection of the data. This was done by selecting individual trees, then setting up both the AVIA and anemometer on individual tripods and starting a scan run. Typically a scan duration of 30 to 60 seconds was used for each scan, using the triple return mode.

1. Processing the Raw Data

The output of the AVIA consists out of *.lvx* files. After a scan, these files are written to either the internal micro-SD card or (when present) an external USB drive. After finishing the required scans, the first step is to have the *.lvx* files processed and transformed to a file format that is more common. For this a specific Python tool (available on my GitHub page [38]) was developed. The tool is capable of taking *.lvx* files from a folder and transforming them to *.las* files while also removing the empty 0, 0, 0 entries.

One specific thing that is possible with the tool is the cutting up of the original *.lvx* file. Say the original file is a 60 second long point-cloud 'recording' of the AVIA's FOV, this means that if the tool was to simply change the file format from *.lvx* to *.las*, the LAS file would contain all the points collected over the 60 second scan duration. Instead, the tool allows its user to specify a certain 'frame' duration so that individual frames will be subsampled to contain only the specified duration worth of points. For example if the frame duration is set to 1000 ms the tool will output 60 subsampled frames that each include 1000 ms of points in chronological order. The first frame contains the points that were measured in the first second of the scan and the last frame contains the points measured in the final second of the scan.

The tool allows the user to create frames as short as 50 ms and as long as the total scan duration of the scan. Next to the point-cloud data, the tool also takes the IMU data from the *.lvx* file and outputs a *.csv* file with the data of each individual frame, together with a overall IMU data file that contains the measurements from the full scan.

When the frame *.las* files are all created, they can be opened in CloudCompare so that the scanned tree can be cut out. For the next step in the processing of the data it is important to make sure that the only points remaining in the files are points from the tree that is scanned. Next to this, if during the scan the AVIA was not positioned perfectly horizontal, the tree will show up slanted in CloudCompare. In this case it will also require the user to manually straighten the tree to make sure it points parallel with the Z axis perpendicular to the ground surface.

The measurements of the WindSonic anemometer are written into a *.csv* file in real time, the anemometer samples at a resolution of 1 Hz and gives an indication of the wind speed in m/s and wind direction in degrees (with 0° indicating a northern wind and 180° implying wind from the south). The wind data does not require any post processing, and the *.csv* files can be used pretty much instantly.

2. PlantMove

With the initial scan data processed and cut up into consecutive frames, the next step is to quantify the wind induced movement of a scanned tree between the frames. To do this, a software tool called PlantMove [39] is used. The tool is specifically designed for deriving three-dimensional motion fields of plant structural movement from time series point clouds.

PlantMove works by aligning 3D point cloud data from two separate (usually consecutive) scans using a non-rigid, time-based registration approach. The software first performs a coarse alignment between scans by assuming a roughly correct global alignment of the 2 clouds and then refines it step by step to detect smaller, local movements. In this way, PlantMove can estimate how each point in the scan has moved both in direction and magnitude even when the motion is very small or varies across different parts of the plant.

Within the PlantMove tool, which runs on MATLAB, several key parameters can be adjusted to control the analysis of plant movement. The 'de-noise' parameter regulates the level of noise filtering applied to the point cloud, this helps to remove measurement errors while preserving structural details. The 'dsp' parameter defines the scale at which local displacements are estimated, which controls the ultimate spatial resolution of the motion vectors. The 'k' parameter specifies the number of nearest neighbours used in the local deformation calculation, influencing the smoothness and reliability of the resulting displacement estimates.

For the analysis of wind induced tree movement and after careful testing, these parameters were iteratively tested to optimise performance and results and the final values were set to the following: de-noise = 4, dsp = 3, and k = 5 (K = 10 for large trees). This configuration was chosen to balance sensitivity to small movements and noise while having acceptable processing times. The average processing run takes approximately 1-2 minutes per frame (depending on the size of the point-clouds), so for a batch of 60 frames it can take up to 2 hours to completely process all frames. To make this more usable, a script was created that automates the processing, meaning it is not required to manually input all the frames. The automation scripts can also be found in [38].

2.1 Consecutive VS Comparative

When analysing plant movement using PlantMove, there are two primary approaches to selecting which scans to compare: consecutive and comparative registration.

Consecutive registration involves comparing each scan only with the immediately preceding one, for example, frame *a* with frame *b*, frame *b* with frame *c*, frame *c* with frame *d*, and so on. This approach captures the movement between successive time steps and is particularly effective for tracking small, continuous motions over time.

Comparative registration compares each scan to a common reference frame, typically the first frame, for example, frame *a* with frames *b*, *c*, *d*, etc. This method highlights the total displacement relative to a fixed reference, rather than the stepwise motion between consecutive scans. Comparative registration is useful for understanding the overall movement patterns and the cumulative effect of wind. For this approach it is important to select an initial frame that shows the tree in its 'non moving' state, as otherwise a movement bias will be present in all the comparisons.

In practice, both approaches can provide complementary insights: consecutive registration reveals small-scale temporal dynamics, while comparative registration captures the broader picture of structural displacement over the entire measurement period.

3. Visualizing and Working With the PlantMove Results

After the frames have been processed by the PlantMove tool, the resulting output files can be used to visualise and analyse the detected movements. The output for each comparison is stored as a *.txt* file containing the original point coordinates (x, y, z) of the first frame along with the corresponding displacement components (dx, dy, dz) to the second frame. These files form the basis for visualizing how each point in the scan has moved between two frames.

To facilitate the visualization of these motion fields, two types of plots can be created using the PlantMove outputs. The first plot type is a scatter-plot that displays the original point cloud, where each point is coloured according to the magnitude of its total displacement. This provides an immediate overview of which parts of the tree experienced the greatest movement. The second plot type represents the same data using quiver arrows, these are vectors that originate from the initial point positions and point toward the corresponding calculated displaced positions. These arrows indicate both the direction and the relative magnitude of the motion.

In addition to generating these static plots for each frame pair (whether consecutive or comparative), it is possible to combine them into an animated sequence. This allows for the creation of time-lapse GIFs showing the step-wise movement over time. Beyond just visualization, the *.txt* output files from PlantMove can be further analysed and used to quantify the movement of the tree. Applications include, correlating the per frame movement with the acquired wind data, the generation of 'movement per frame' histograms and an analysis of the movement inside separate individual horizontal slices of a tree. These results will be shown and discussed in Chapter 4.

Plan 2: Morphological Changes On The Beach

This fieldwork plan can be divided into two parts; the test to see if measuring aeolian sand transport is possible and the more common terrestrial scanning setup for the monitoring of deposition and erosion in windy conditions. The data processing workflow for this plan is split up two parts as well.

Measuring Aeolian Sand Transport

The setup for this test involves placing the AVIA down on the beach so that it can scan parallel to the beach surface directly in the plane of the saltation layer. This test has the option of using both the repetitive and non-repetitive scanning modes (Subsection 2.2.2). As the expected dynamic process occurs only in a thin layer above the beach surface, using the repetitive mode could provide advantages over the non-repetitive scanning mode. The non-repetitive mode will collect a lot of points outside the area of interest while the repetitive scan mode only scans in the target plane likely resulting in more meaningful returns.

During the fieldwork test, multiple scans were made using both scan modes so that their performances can be compared. The scans were made by aiming the scanner into, perpendicular to and away from the wind in the plane along the beach surface and scanning for at least 10 seconds. After the test, similar to the tree movement workflow, the *.lvx* data was processed and cut up into individual *.las* frames so that they can be opened in CloudCompare. From this point on the frames can be further analysed and the preliminary results will be discussed in the next chapter.

Measuring Erosion and Deposition

The second setup for the tests on the beach was partially performed like described in the plan 2 introduction. Instead of a longer duration setup plan to also test the autonomous mode of the COR, only a short test could be performed. The test started by placing the setup 20 meters away in front of a large dune ridge, aiming the AVIA towards the ridge and starting a 10 second scan. In order to simulate erosion and deposition over extended time periods during a windy day, after the initial scan, a small amount of sand was removed from the ridge using a shovel after which a second 10 second scan was made so that the two scans could be compared to one-another.

Processing again involved transforming the *.lvx* files into *.las* files, using all the points gathered in the scans (to maximise point density and coverage). The *.las* files can then be opened in CloudCompare so that the area of interest can be cut out and with the use of the built in cloud-to-cloud calculation tool the differences between the two scans can be analysed.

Compared to the wind induced tree movement workflow, these sections are shorter as this fieldwork plan was a later addition for the validation of the setup. Because of this, the results shown in the following chapter will have initial results that are not as worked out as the results from the wind induced tree movement fieldwork.

Chapter 4

Results

The results chapter is divided into 3 sections, the first section shows the results of the specifications validation described in Section 3.1, the second section discusses the results of the vibration effect analysis from Section 3.2 and the third section goes over all results from the fieldwork tests that were introduced in Section 3.4.

4.1 AVIA Specs Analysis Results

This section presents the results of the specification validation tests described in Section 3.1. Each subsection corresponds to one of the AVIA sensor specifications assessed in the methodology, comparing the manufacturer-provided values with the measurements obtained from tests. The results help with performing a solid evaluation of the AVIA's performance and highlight where 'real-world' behaviour deviates from the stated specifications.

4.1.1 Non-Repetitive Scan Mode FOV Coverage

FOV Coverage Percentage

The evolution of FOV coverage over time was analysed using the grid-based coverage estimation method described in Section 3.1.2. Figure 4.1 visualises coverage after 50 ms, 500 ms, 800 ms, and 1000 ms of scanning. After 800 ms of scan time, the coverage is estimated to be (only) 87.29% which is not close to the 100% that is stated in the AVIA's manual.

For a scan time of 1000 ms the coverage is estimated to be 92.24% where a majority of the 'gaps' can be seen in the outer edges of the ellipse (Figure 4.1d), whereas after 800 ms some large gaps can also be seen closer to the center of the FOV (Figure 4.1c). The difference in coverage times can possibly be explained by the equation Livox uses (Equation 2.1 [20, Section 2.1]). For this equation it is uncertain how the "Total Area Illuminated by Lasers" counts pixels that are illuminated/covered multiple times, but it seems that everything is added to a final total, even already covered areas resulting in an overestimation of total coverage. There could be other attributes to this difference but this is hard to tell as the method they use is not described in much detail.

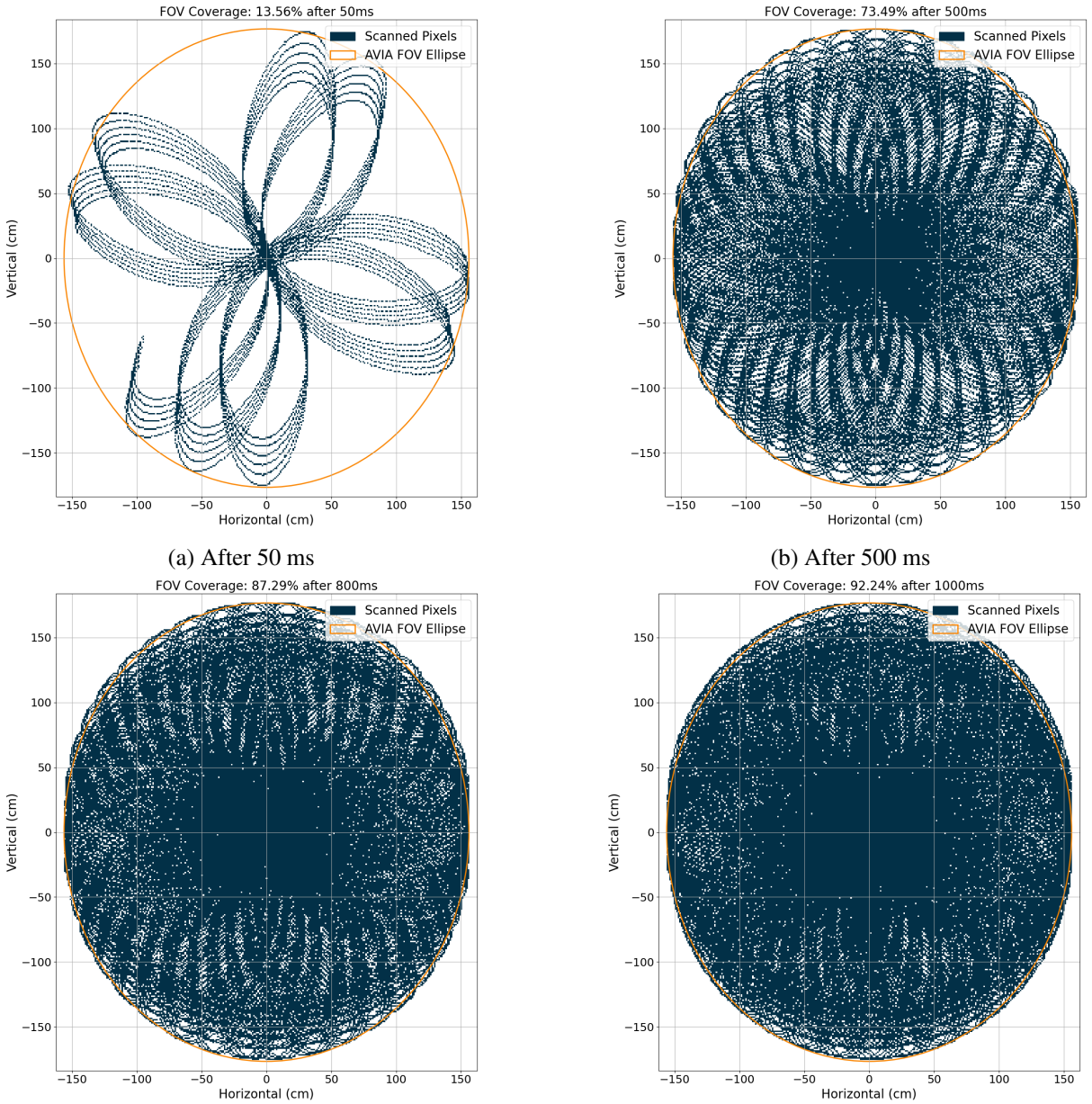

(a) After 50 ms

(b) After 500 ms

(c) After 800 ms

(d) After 1000 ms

Figure 4.1: Evolution of FOV coverage over scan duration.

Both the method from Livox and what is shown in the figures above, use square pixels to calculate the coverage %, if instead rectangular pixels with the same size as the laser beam footprint are used, the calculated coverage is significantly lower as can be seen in Figure 4.2, the coverage only gets to 26.56% which is significantly lower than the 92% for the square pixels. For the rest of the analysis the square pixel grid estimation will be used.

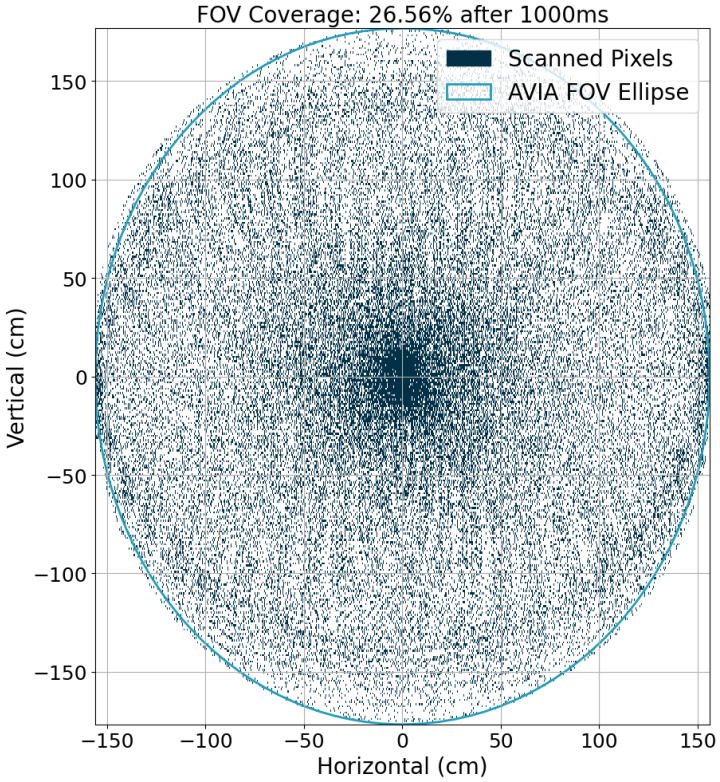

Figure 4.2: FOV coverage after 1000 ms when using rectangular pixels

The total coverage durations for scans, up to 5000 ms were calculated and plotted in Figure 4.3. The figure shows that for the square pixel method, a near 100% coverage can be reached, but only after 2000+ ms.

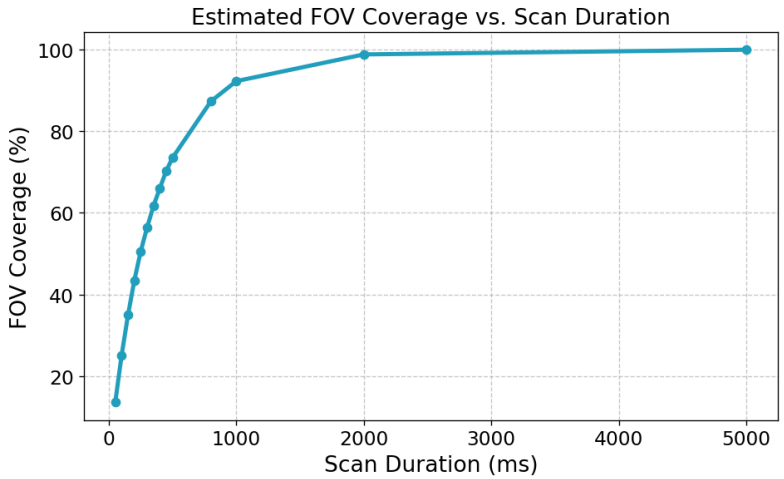

Figure 4.3: Estimated FOV Coverage Percentage for scan durations from 0 - 5000 ms

Pattern Development Over Time

By colouring the scanned points sequentially, a single image can illustrate how the scan pattern evolves across the FOV, and is shown in Figure 4.4 below.

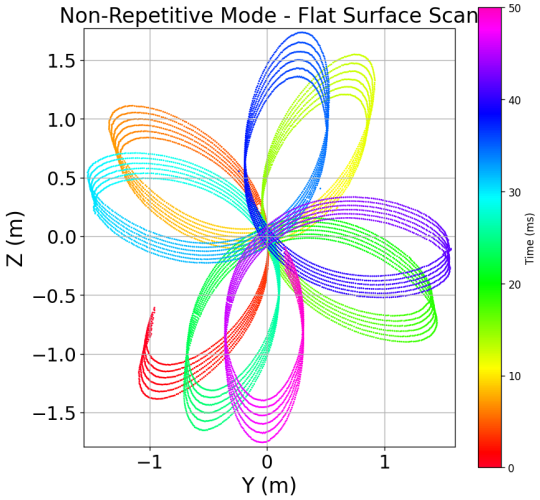

(a) Scan pattern development over 50 ms

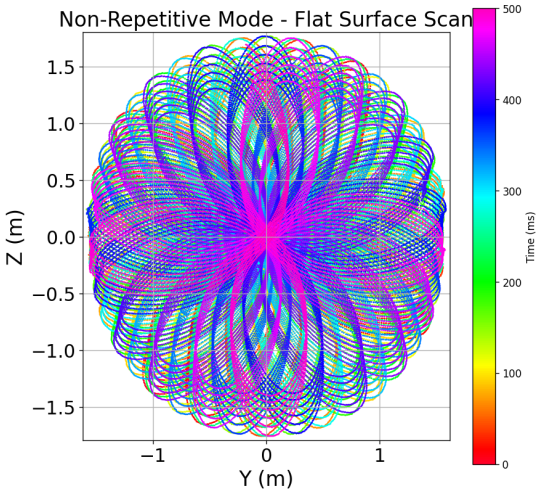

(b) Scan pattern development over 500 ms

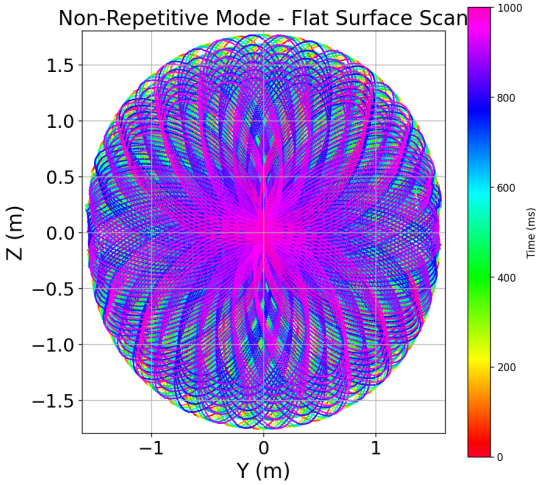

(c) Scan pattern development over 1000 ms

Figure 4.4: Livox AVIA's non-repetitive scan pattern development over time

The figures reveal two key observations. First, the scan pattern prioritizes the central regions of the FOV, producing much denser coverage in the middle compared to the periphery. This is caused by the shape of the non-repetitive scanning pattern, which passes through the center with each new petal. At shorter scan durations (<500 ms), gaps are clearly visible between the petals, particularly in the outer half of the FOV. As the scan progresses, the center becomes increasingly densely covered, while the edges remain comparatively sparse.

FOV Point Density Heatmap

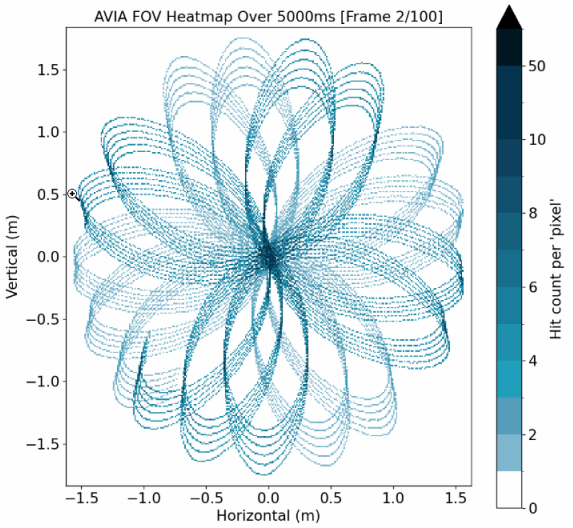

(a) After 100 ms

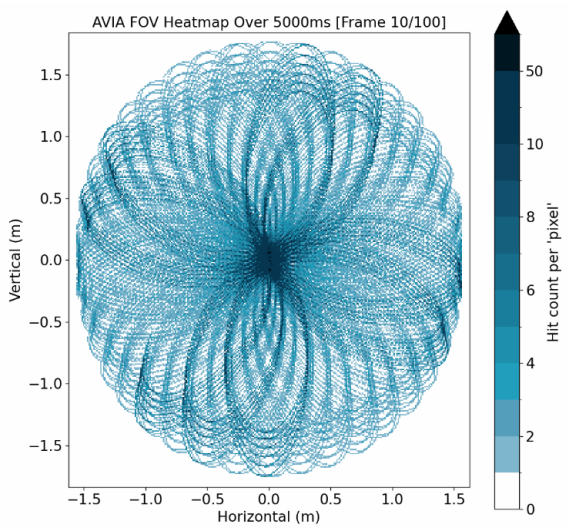

(b) After 500 ms

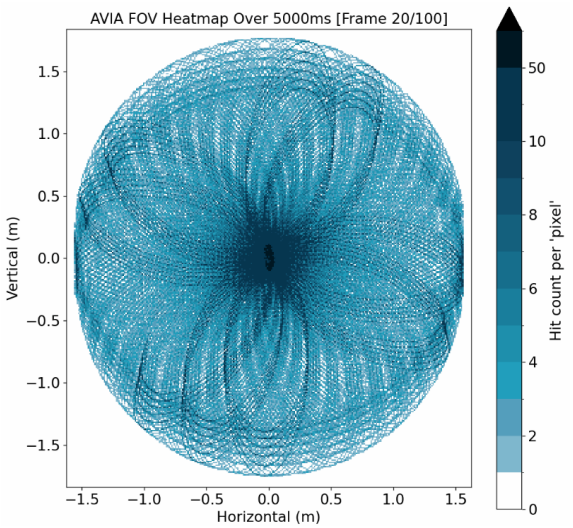

(c) After 1000 ms

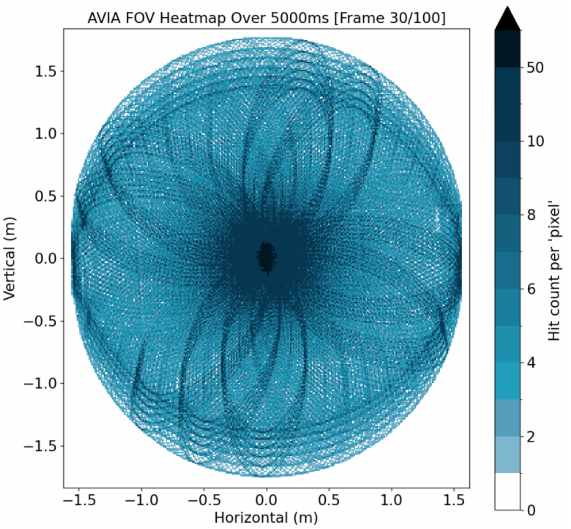

(d) After 1500 ms

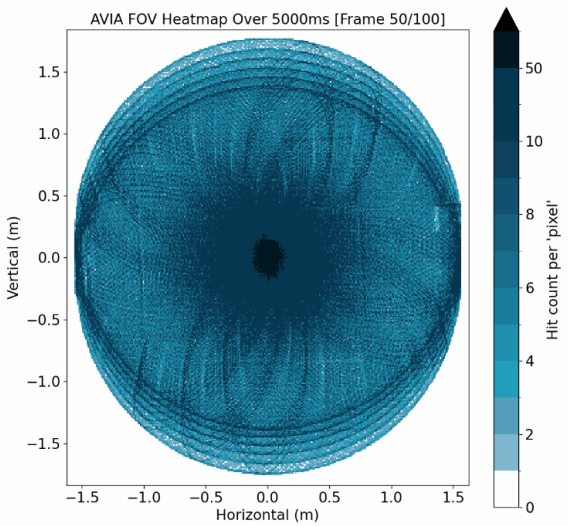

(e) After 2500 ms

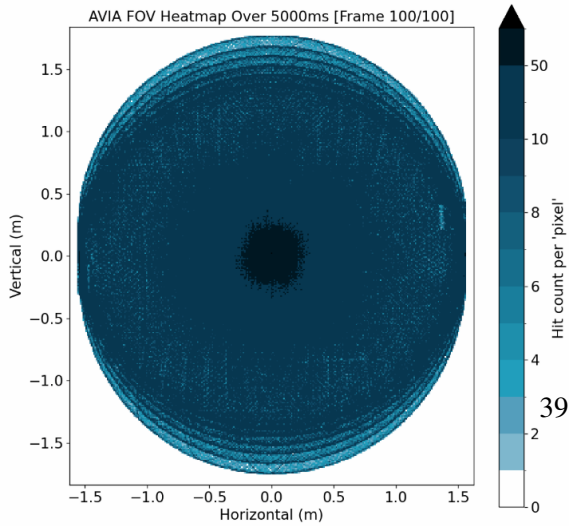

(f) After 5000 ms

Figure 4.5: FOV Coverage Plots over a range of 100 to 5000 ms

The heatmaps reveal the strongly non-uniform distribution of hits across the FOV throughout the scan. Figure 4.5 shows six snapshots from a 5000 ms scan, illustrating that pixels in the centre of the FOV accumulate way more hits, whereas edge pixels especially near the FOV boundary are covered a lot more sparsely.

Combined with the coverage percentage analysis, these results demonstrate that although the AVIA achieves relatively fast FOV coverage, this does not translate to a uniform scan density.

FOV Point Density Distribution

Following the method described in Section 3.1.2, the resulting point density distribution plots show a non-uniform spread over the FOV, as can be seen in Figure 4.6 and Figure 4.7.

Point density is measured to be the highest near the FOV centre and decreases toward the edges of the ellipse, a clear peak appears around ring 40 and seems to correspond to the positions where the rotating "petal tips" of the non-repetitive scan pattern intersect. As the flower shape rotates over 360° in the FOV, the tips create higher density rings that can also be seen in the Heatmaps (e.g Figure 4.5d).

The value of the PPm2 coverage will change depending on the distance of the scanner to the scanned target, the relative distribution will remain equal for all distances as this has to do with the non-repetitive scan pattern itself. Understanding how the points are distributed is beneficial knowledge when aiming the AVIA at a target. Knowing this also provides a platform for figuring out if this non-uniform distribution can be used advantageously.

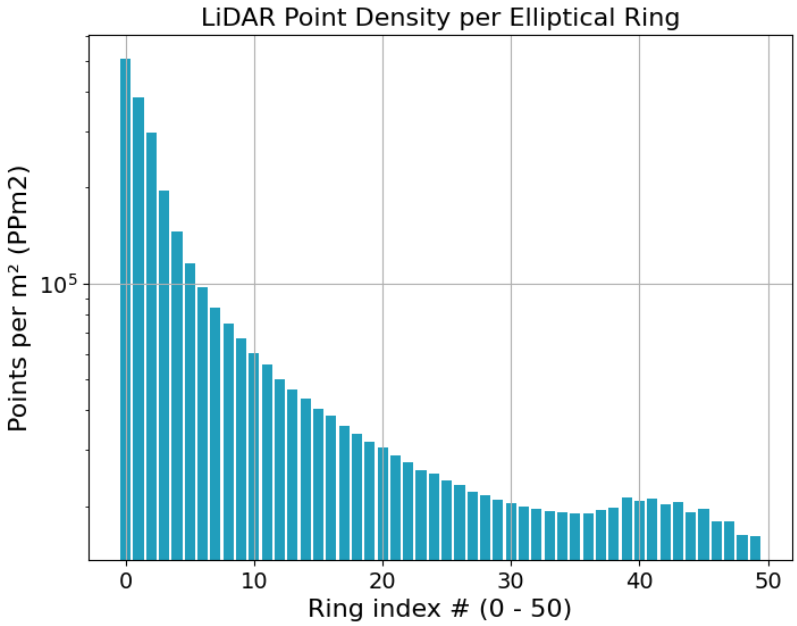

Figure 4.6: Log-Linear histogram showing the points per m^2 of ring 1-50

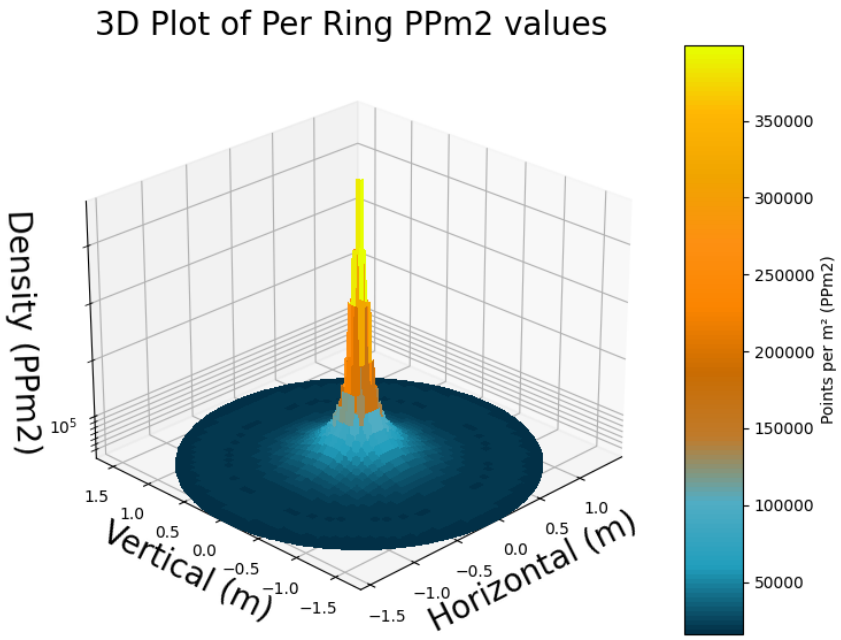

Figure 4.7: 3D plot of the point density distribution using the ring estimated PPm2 values

Regional FOV coverage percentages

The regional coverage analysis shows that smaller central regions of the FOV achieve high completeness substantially faster than the full FOV. Figure 4.8 shows that the region covering the inner 20% of the FOV reaches 100% coverage at just over 450 ms, while larger regions require progressively longer scan durations.

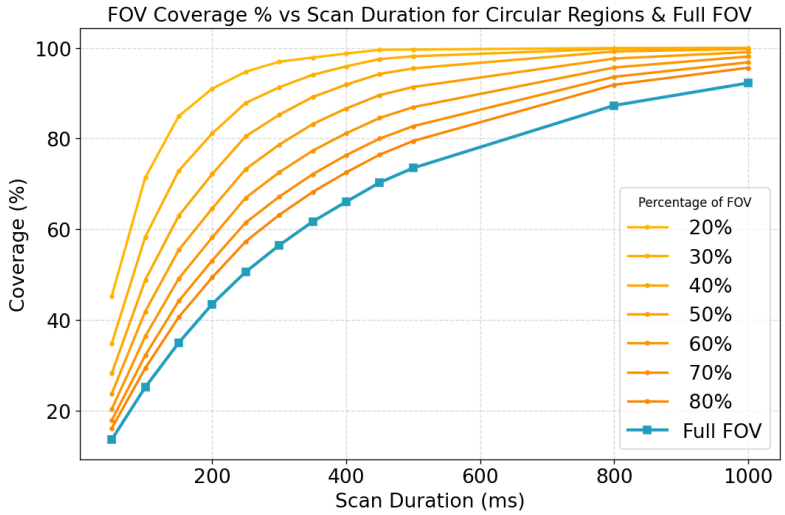

Figure 4.8: Regions FOV Coverage Percentage for scan durations from 0 - 1000 ms

Figure 4.9 illustrates the relationship between region size, coverage threshold, and achievable temporal resolution. The three blue lines represent different minimum coverage thresholds (90%, 95%, and 99%). The horizontal axis corresponds to the region size (as fractions of the FOV semi-major axis, see the circles in Figure 3.4), and the vertical axis shows the time required to reach the respective coverage threshold. The horizontal orange lines indicate the achievable temporal resolution in Hz for different region sizes and coverage thresholds.

For example, if you want to prioritise temporal resolution, you can see that if you accept a coverage threshold of 90%, and a region size of just the inner 20% of the FOV, a temporal resolution of up to 5 Hz can be achieved. Continuing, if you want to optimise for coverage (be able to use a larger region size) but still want to increase the temporal resolution to at least 2 Hz, selecting a coverage threshold of 90% means you can use the inner 50% of the FOV while being able to sample at 2 Hz.

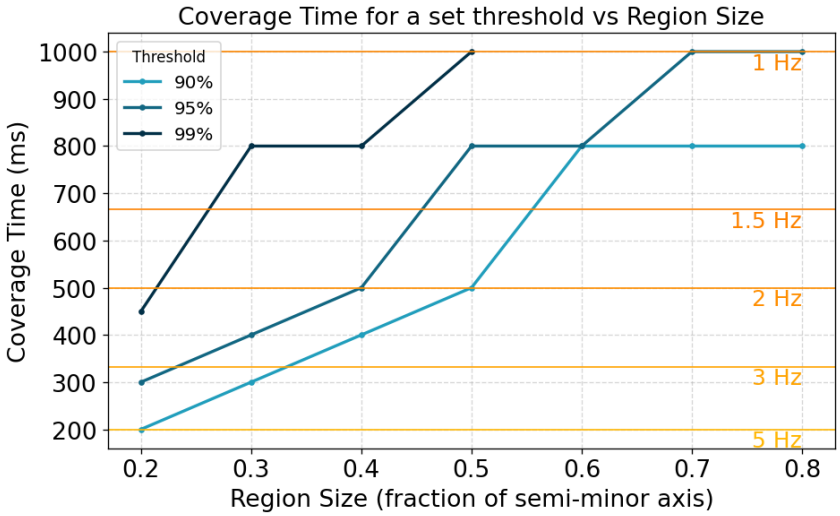

Figure 4.9: Diagram showing the time to coverage for 3 different threshold %, to help select scan parameters for required temporal resolutions (in Hz)

In summary, the scan mode analysis shows that the claim of 100% coverage in 800 ms seems to be a bit too optimistic. Using a scan time of 1000 ms results in a FOV coverage of >92 % which is high enough to be able to compare consecutive frames as at this point only small gaps remain (see Figure 4.1d).

The analysis also reveals intrinsic non-uniformity in point density coverage over the FOV, which makes it possible to consider regions in the center of the FOV where higher temporal resolutions (of up to 5 Hz) can be obtained. Overall, these insights can guide optimal selection of scan duration and where and how to aim the scanner.

4.1.2 Scan Quality

The results of the DRE analysis (described in Section 3.1.3) are summarised in Table 4.1 with an example of the created histogram and 3D representation of the scan shown in Figure 4.10. In the center of the FOV, the standard deviation of the point-to-plane distances is found to be 0.81 cm. The DRE decreased slightly towards the horizontal edge, with the highest recorded value being 0.54 cm. Along the vertical axis, a similar trend was observed, values remained below 0.66 cm, with no significant increase at the bottom edge of the FOV.

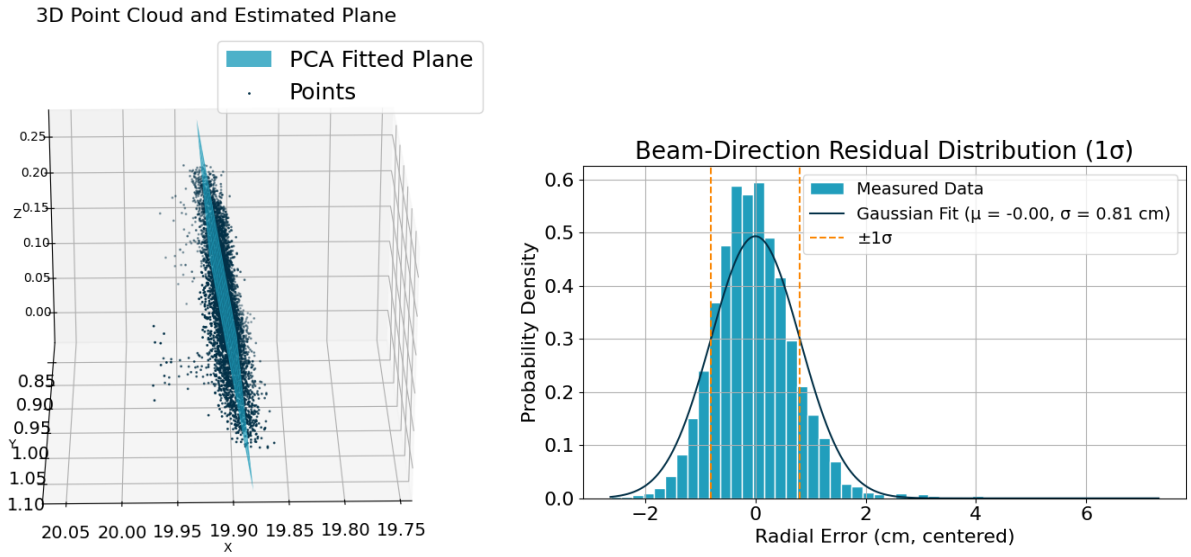

(a) PCA estimated Plane with Points

(b) Distance Random Error Histogram

Figure 4.10: Distance Random Error Estimation Figures

Table 4.1: Distance Random Error at 20 meters for the target placed in different parts of the AVIA's FOV

Target Position within FOV	**Random Distance Error 1σ [cm]**	**Number of Points**
Center	0.81	6446
50 % Right	0.51	945
75% Right	0.51	798
Right Edge	0.54	1482
50% Down	0.55	1152
75% Down	0.61	838
Bottom Edge	0.66	787

This demonstrates that the AVIA maintains a consistent level of range precision across its FOV, with all measurements well within the specified <2 cm at 20 m. Visual inspection of the histogram plots showed clean Gaussian distributions with no bias. Overall, the results suggest that the specification is conservative, and that in normal scanning conditions, the AVIA maintains high distance measurement precision throughout its FOV. For the used scans, 0 points (outliers) were found to be further than 20 cm of the fitted planes, stricter outlier removal will only result in even lower RDE values.

4.1.3 Point Density and Footprint Size over Distance

The estimated point density curves show a large drop in density in the first 20 meters and a clear difference in density between the inner and outer halves of FOV. The inner half of the FOV has substantially higher PPm2 values, reaching up to 2.4 times the density of the outer half. At close range (3 m), the inner region achieves PPm2 values above 22000, at 100 m this decreased to roughly 20 PPm2. The outer region, like expected, shows lower densities, from approximately 9500 PPm2 at 3 m to around 8 PPm2 at 100 m (see Figure 4.11). These values suggest that the AVIA is most effective for close to mid-range dynamic scanning, as long-range applications will be limited by low point densities. This leads to a trade-off where if higher point densities are required, longer scan durations are needed resulting in not being able to scan at a high temporal resolutions.

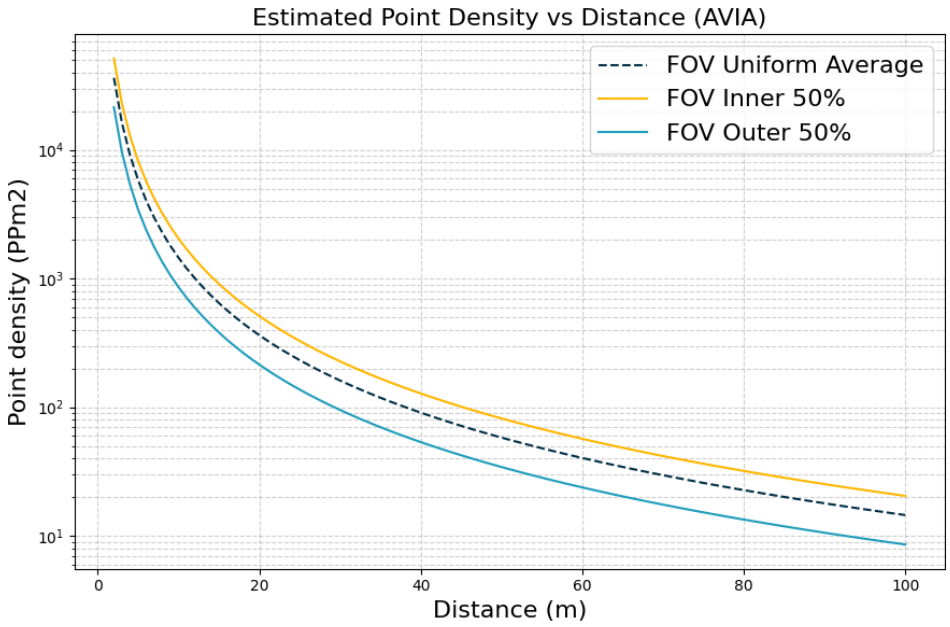

Figure 4.11: Log Linear plot showing the estimated point density (PPm2) of the Livox AVIA over distances from 2-100 meters

The large field of view (70.4° × 77.2°) in non-repetitive mode allows the scanner to capture broad scenes, making it practical for static monitoring setups. The coverage is not uniform and the center of the FOV offers a higher density, this means it is beneficial if the main region of interest or the scanned object are aligned with this zone. Overall, achieving a 92% coverage of the full FOV within 1000 ms provides a practical balance between spatial coverage and temporal resolution, supporting a frame rate of 1 FPS and, for smaller regions even higher.

The footprint growth analysis (Figure 4.12) shows that the large vertical beam divergence (0.28°) causes the illuminated patch to expand a lot with increasing distances. At 100 m, the vertical footprint size is already more than 0.5 m while the footprint is only 5.24 cm wide. The footprint size at higher ranges can be acceptable for general terrain mapping, but it limits applications that require the measuring of small objects or features.

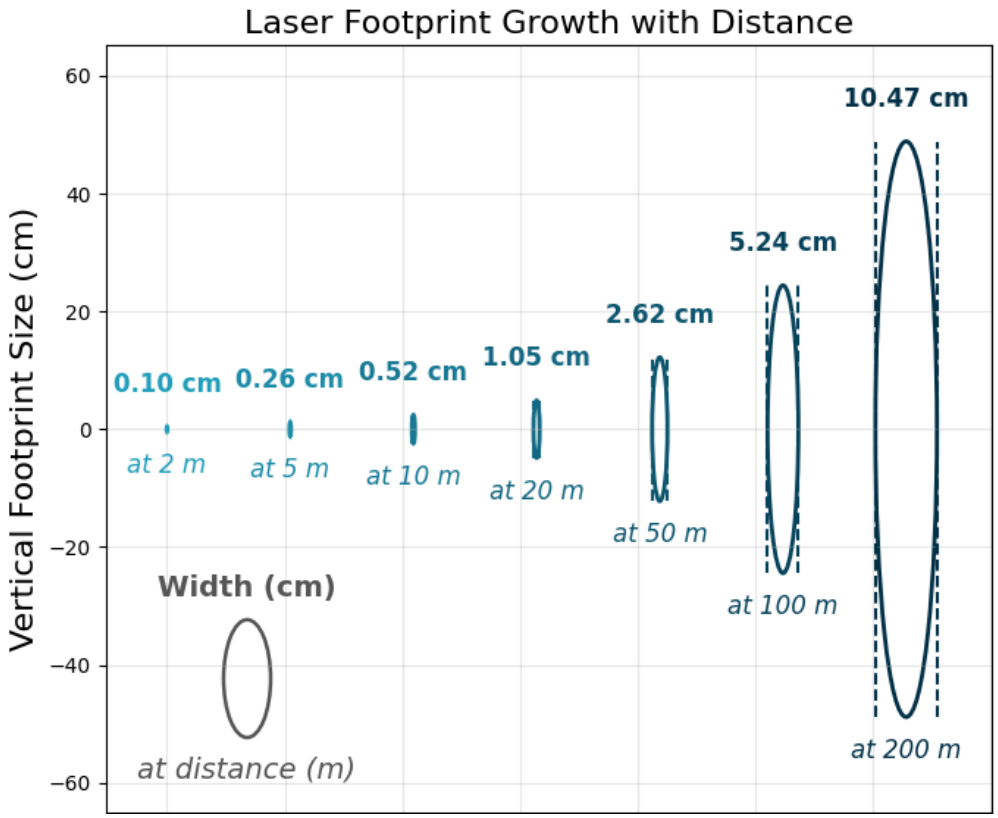

Figure 4.12: Horizontal and Vertical laser beam footprint sizes at distances from 2 to 200 meters

4.1.4 Detection Range

A first and consistent result concerns the short-range blind zone. The AVIA does not return valid measurements below approximately 2 m, below this range it is likely blinded by its own signal. This lower bound was encountered in all experiments and can be regarded as a fixed constraint.

Beyond this blind region, the AVIA performs well within a what can be described as a 'close-to mid-range' window of roughly 2–100/150 m (depending on application). This range corresponds well with the point-density analysis presented earlier (Subsection 3.1.4), where density decreases to very low values at similar distances (100/150 m). Outdoor scans acquired throughout the research reinforce this conclusion. In all tested environments whether on an open beach or in a park more than 95% of all valid returns occurred within 150 m, with the majority concentrated below 100 m.

This can also be seen in Figure 4.13, although isolated returns can be observed beyond 200–300 m (Figure 4.13b), they are extremely sparse an don't provide a clear measured surface. At these ranges the vertical footprint has expanded to over a meter (Figure 4.12), meaning that even when a return is recorded, the size of the illuminated patch prevents meaningful interpretation of small-scale objects or realistic environmental dynamics.

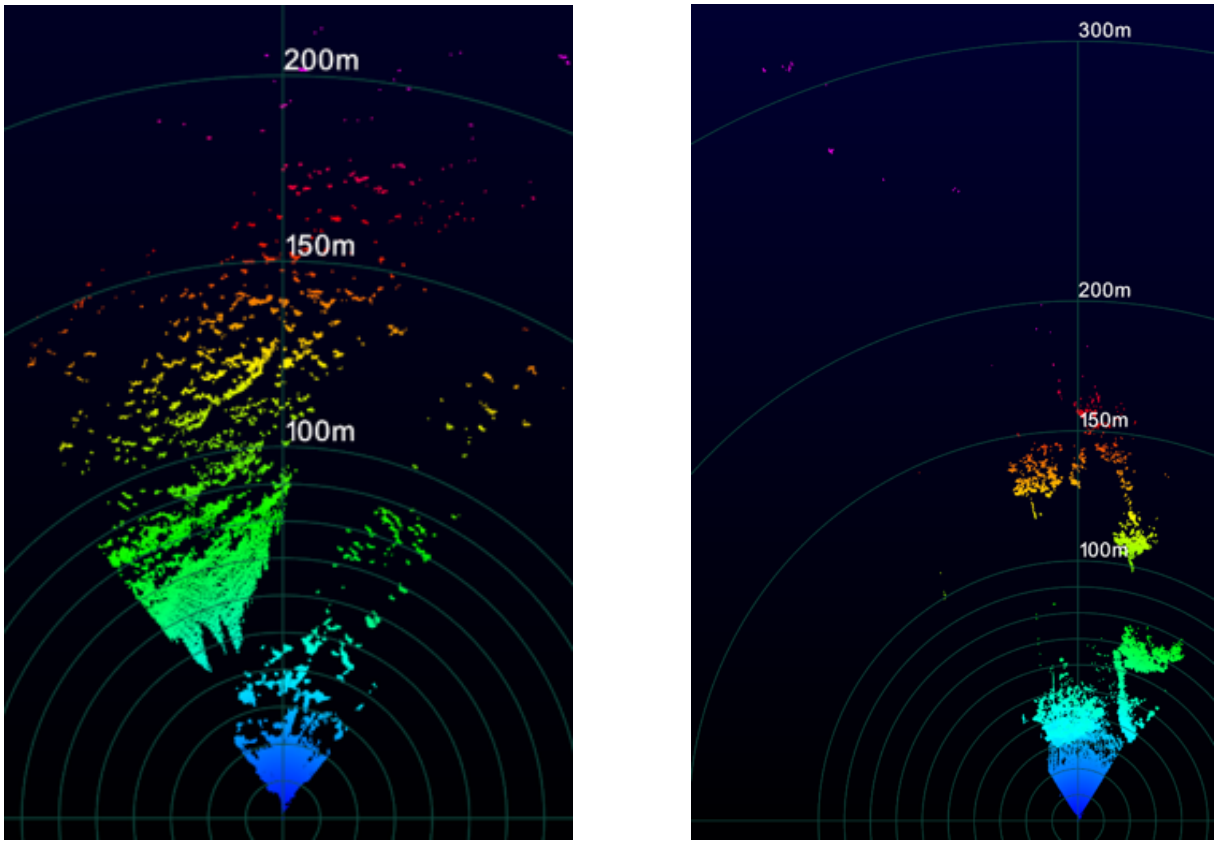

(a) Range overview from a scan on the beach, showing points scanned up to 200 meters away

(b) Range overview from a scan in the park, showing points scanned as far as 300 meters

Figure 4.13: Range overview form different scans acquired throughout the thesis project

The fast decrease in long-range coverage does highlight an aspect not assessed in this thesis that is relevant for future work. This is the incidence angle dependence. In many outdoor scenes, surfaces at large distances are simultaneously illuminated at increasingly oblique angles (Figure 4.14), further reducing the likelihood of strong returns. A controlled experiment isolating incidence angle and reflectivity would therefore be good way to quantify the AVIA's true detection range.

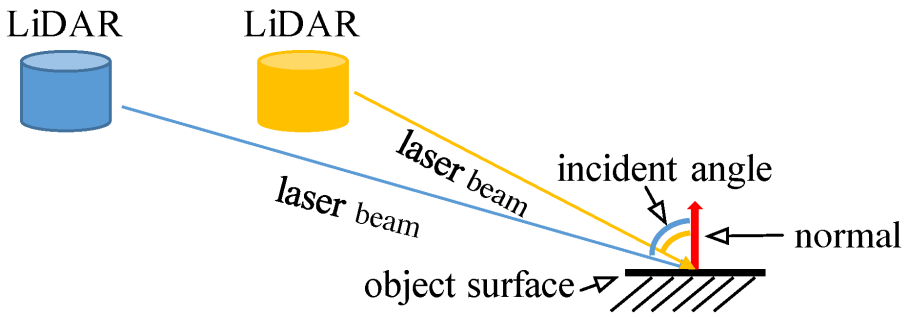

Figure 4.14: Image showing the increase in incidence angle at larger distances [40]

From the controlled corridor experiment described in Subsection 3.1.5, the results show a strong directional dependence of the footprint. When oriented sideways, the sensor registered nearly four times more hits on the cones ($\approx$ 1200 vs $\approx$ 300). Furthermore, the shape distortion is clearly visible in Figure 4.15, in the upright configuration, the cone appears vertically stretched to almost 1.5 m, roughly three times its real height. This deformation corresponds directly to the orientation of the footprint's long axis, which seemingly dominates the sampling geometry at range. For the sideways scan, the results is the exact opposite, here the cones are stretched horizontally and get more than 3 times as wide.

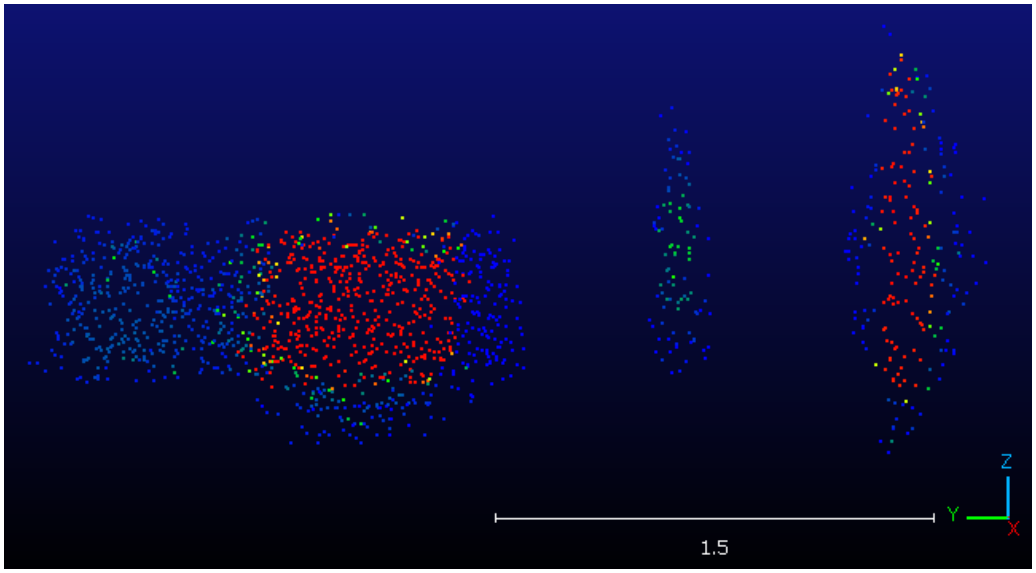

Figure 4.15: The scanned cones side by side, AVIA positioned upright (right) and AVIA positioned on its side (left)

The strong directional stretching seen in both orientations demonstrates that the footprint's large semi-major axis effectively smooths/smears in that direction, causing objects to be elongated along this axis regardless of their actual shape. The difference in hit count between the upright and sideways orientations further points out that long-range detectability is tied to how well the footprint aligns with the physical shape of the object.

4.2 The Influence of Environmental Factors

This section includes the results from the tests described in Section 3.2. These tests were performed to help improve the understanding of the AVIA by looking at how external vibrations affect the measurements and by looking at the general consistency between scans.

4.2.1 Vibrations

Using the test described in Subsection 3.2.1, for each selected frame, the Random Distance Error of these cut-outs is calculated using the same method as described in Section 3.1.3. The resulting values were plotted for visual comparison between the static, average, and high movement conditions.

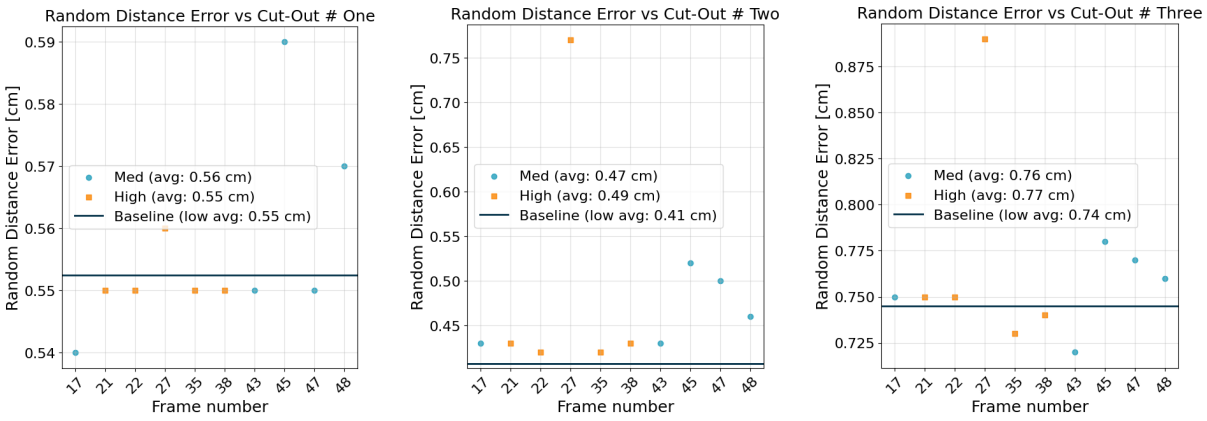

(a) RDE Results for cut-out 1 (b) RDE Results for cut-out 2 (c) RDE Results for cut-out 3

Figure 4.16: RDE Results

The results in Figure 4.16 show that the forced vibrations introduce only a marginal increase in RDE. Across all three cut-outs, the difference between static and moving frames remained below 0.8 mm, well within the expected noise range of the sensor. This suggests that the AVIA's distance accuracy is largely unaffected by small, irregular vibrations typical of outdoor mounting conditions on rigid tripods or poles.

However, several factors could be refined in future testing:

- Using controlled vibration sources with known frequencies and amplitudes would enable more systematic correlation between movement and scan error for the AVIA.
- Extending the analysis to greater scanning distances could determine how the vibration effects scale with range.
- Including slower, low-frequency oscillations could simulate conditions of flexible mounting positions (e.g., long poles or vehicle platforms) with lower natural frequencies.
- Using different non-flat targets and different error estimation techniques, not just RDE.

Overall, the test indicates that under normal mounting conditions and moderate wind exposure, the AVIA remains stable, and its IMU provides sufficient information to identify and potentially correct vibration periods during data processing.

4.2.2 Stability Between Scans

Using the method described in Subsection 3.2.3, the mean distance between the 2 scans is found to be 0.00723 m with a standard deviation of 0.00588 m. These low values indicate that no significant displacement occurred between the scans. Following this, with the use of Fine Registration ICP the transformation matrix was calculated which shows the translations needed to align the two clouds. These values confirm that the scans already aligned nearly perfectly, suggesting that the remaining residuals can likely be attributed to measurement noise rather than scanner movement.

Table 4.2: Transformations needed to align the clouds from Fine Registration ICP between the two scans

	X	**Y**	**Z**
Translation (mm)	0.175	0.263	-0.025
Rotation (°)	0.01006	0.00050	0.00028

Next to the above analysis, an analysis using the accelerometer data from the IMU was used to confirm the conclusion. For this, the mean acceleration in X, Y, Z for each scan was found and used to calculate the difference between scans. This calculation can be seen below.

Table 4.3: Mean accelerometer readings (m/s^2) from both scans, see Figure 2.5 for the orientations of the axes

	X	**Y**	**Z**
First Scan	0.16752	0.01932	0.98049
Second Scan	0.16766	0.01942	0.97996

The mean acceleration vectors for each scan were calculated as:

$$\begin{bmatrix} X \\ Y \\ Z \end{bmatrix}, \quad \vec{a}_1 = \begin{bmatrix} 0.16752 \\ 0.01932 \\ 0.98049 \end{bmatrix}, \quad \vec{a}_2 = \begin{bmatrix} 0.16766 \\ 0.01942 \\ 0.97996 \end{bmatrix}$$

The difference between the two vectors was then computed as:

$$\Delta\vec{a} = \vec{a}_2 - \vec{a}_1 = \begin{bmatrix} 0.00014 \\ 0.00010 \\ -0.00053 \end{bmatrix}$$

with a magnitude of

$$|\Delta\vec{a}| = \sqrt{(0.00014)^2 + (0.00010)^2 + (-0.00053)^2} = 0.00055 \text{ m/s}^2 \tag{4.1}$$

This corresponds to approximately 0.057 mg, which is less than the sensor's nominal resolution of (0.09 mg) and noise floor ($\approx$ 0.024 m/s^2 RMS). These results indicate that the IMU is not sufficiently sensitive to detect motion or rotation at these low movement levels.

The results show that, when securely mounted, the AVIA produces repeatable point clouds over extended periods. Successive scans can be overlapped with minimal adjustment, and residual differences seem to mostly be caused by intrinsic scanner noise rather than mechanical drift. It confirms that the system is suitable for long-term monitoring applications requiring consistency without frequent recalibration when no external movement or vibrations are introduced. It is recommended to repeat this test while the scanner is vibrated periodically in order to see if this does influence the consistency between scans.

4.3 Fieldwork Results

With the setup and workflows described in the previous chapters, the Livox AVIA was deployed to actually collect data in dynamic outdoor environments. This chapter presents the results of the wind induced tree movement fieldwork and discusses the outcomes obtained from the processing workflows introduced in Subsection 3.4.2. The results demonstrate how the AVIA's characteristics such as its rapid FOV coverage and synchronization with an anemometer enables detailed observations of tree motion in varying wind conditions. The results from the second fieldwork topic show the scanners capability to measure aeolian sand transport and dune erosion.

4.3.1 Wind Induced Tree Movement Scans

Using the defined workflows, several scanning sessions were performed to observe the dynamic response of trees to wind. In total, four scans were carried out, three of which included simultaneous wind speed and direction measurements. An overview of these scans and the target trees is provided in Table 4.4 and images of these trees are shown in Figure 4.17.

Table 4.4: Overview of tree scans, including wind data availability, tree type, height, and subsampling parameters.

Name	Wind Data	Tree Type	Height (m)	Subsampling (ms)	Scan-Time (s)
Scan 1	No*	Canadian poplar	∼32	1000	64
Scan 2	Yes	Narrow-leaved Ash	∼10	500, 1000	60
Scan 3	Yes	Canadian poplar	∼27	1000	30
Scan 4	Yes	Birch	∼20	500, 1000	60

* For scan 1 no wind data could be collected, as by the time the anemometer was operational, this tree was cut down.

(a) Tree from scan 1

(b) Tree from scan 2

(c) Tree from scan 3

(d) Tree from scan 4

Figure 4.17: Images of the scanned trees

Displacement Magnitude and Quiver Plots

The first products generated using PlantMove are displacement magnitude and quiver plots. These visualizations depict the magnitude and direction of tree movement between two frames, providing an intuitive overview of motion patterns. They were used to assess both the intensity and coherence of tree deformation across time. Animated sequences of the scatter and quiver plots can be seen in [38].

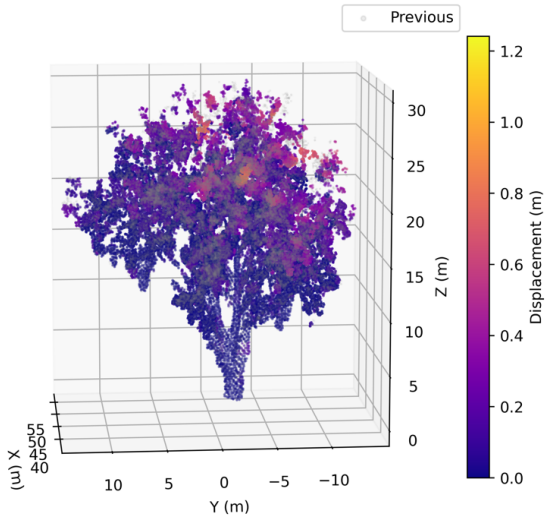

(a) Scatter plot of Tree 1

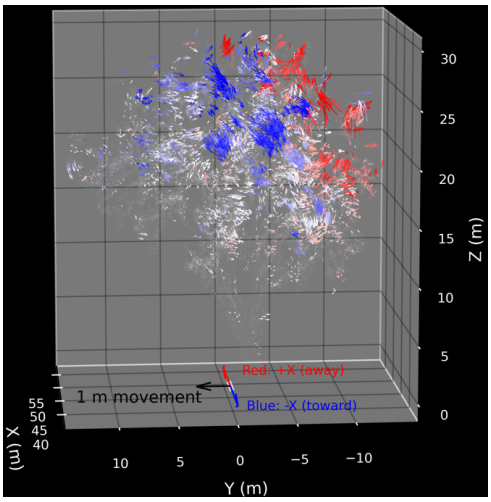

(b) Quiver plot of Tree 1

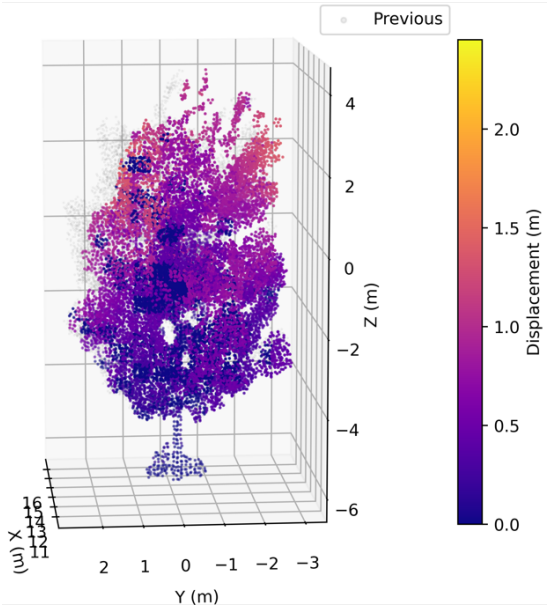

(c) Scatter plot of Tree 2

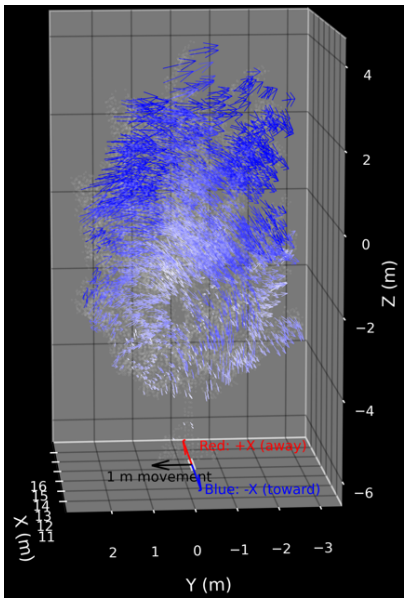

(d) Quiver plot of Tree 2

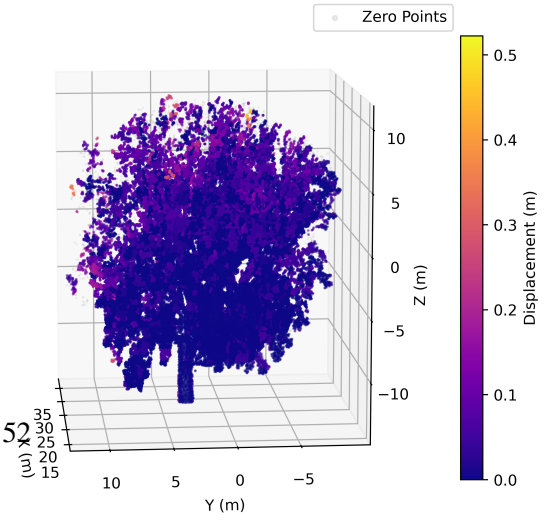

(e) Scatter plot of Tree 3

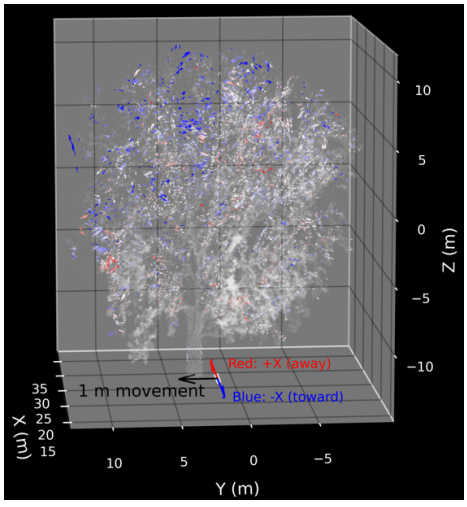

(f) Quiver plot of Tree 3

Figure 4.18: Example Scatter and Quiver plots of scan 1-3

The scatter and quiver plots provide complementary insights into the dynamic response of trees to wind. From the scatter plots Figure 4.18, you can observe the absolute magnitude of displacement for different parts of the tree, allowing for a straightforward assessment of which branches or sections experience the largest movement.

The quiver plots on the other hand, illustrate directional information, revealing patterns of motion that are not immediately evident in the scatter plots. For example, as seen in Figure 4.18b, some branches move in opposite directions, highlighting more complex behaviour such as torsion or bending in response to wind gusts.

When the plots are put together as consecutive frames and viewed in sequence, the movement of the trees over time becomes visible. This makes it possible to observe natural motion patterns, including branch swaying or the entire tree moving, which is not really noticeable in a static single frame. This type of visualization can help with understanding how trees respond to wind and can support studies of tree mechanics or environmental monitoring.

Comparative vs. Consecutive Frame Analysis

When evaluating tree motion using PlantMove, two complementary approaches can be employed: consecutive (frame-to-frame) and comparative (fixed reference) analysis.

Consecutive analysis compares each scan with the immediately preceding one, capturing small-scale temporal dynamics. This approach is effective for visualizing natural, continuous motion, such as branch swaying or gradual trunk bending, without introducing artifacts from an arbitrary reference frame.

Comparative analysis aligns all frames to a common reference. It emphasises overall displacement relative to a static baseline, showing how far the tree moves from its 'normal' position. However, this method is sensitive to the choice of reference frame. If the selected frame already exhibits significant motion, a systematic bias is introduced across all subsequent comparisons.

An example of this bias effect can be seen in scan 1. The selected reference frame includes an initial displacement, causing the comparatively processed results to always show motion, particularly in the top-right portion of the tree, as shown on the next page in Figure 4.19 (a, c, e). The consecutively processed frames (b, d, f), shown in the right column, reveal minimal movement in the same frames.

In practice, consecutive analysis seems to be best for capturing short-term, stepwise dynamics, while comparative analysis provides insight into overall displacement magnitude and directions but this does require a selecting a correct reference frame. Inspecting consecutively processed frames first could help select an appropriate reference, for future work, this can be used to reduce bias by identifying periods of minimal movement in consecutive frames, which can then help pick a good reference for comparative analysis.

One thing that was not considered was to use a significantly longer/denser scan for the comparative PlantMove analysis, while this scan would include more movement, having a denser cloud to compare to might improve the consistency of the results that PlantMove outputs.

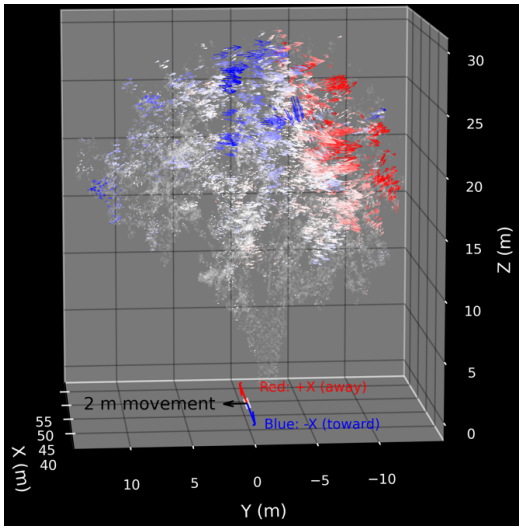

(a) Comparative frame 6

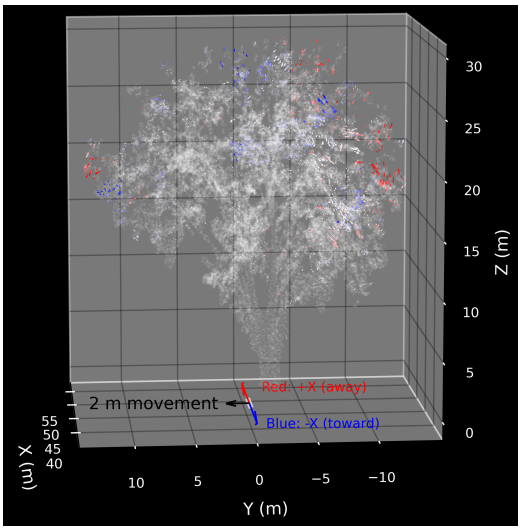

(b) Consecutive frame 6

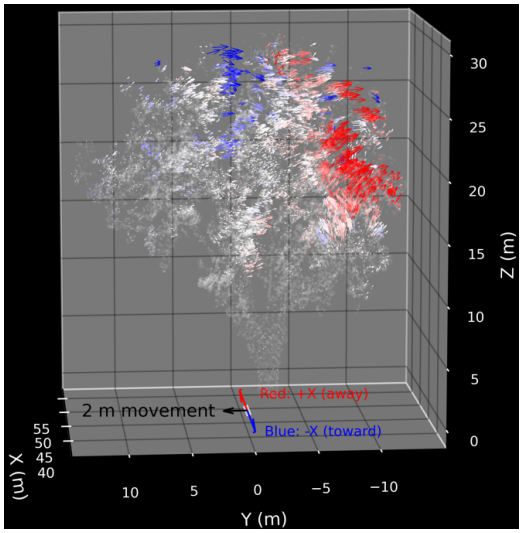

(c) Comparative frame 35

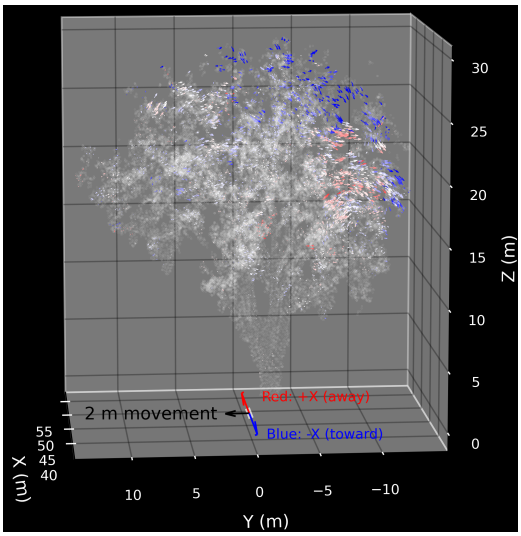

(d) Consecutive frame 35

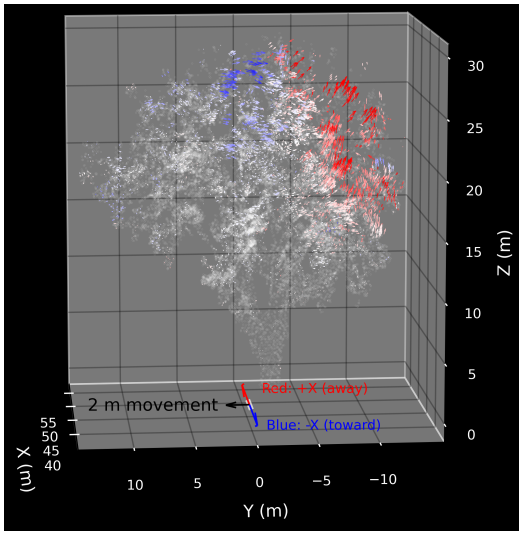

(e) Comparative frame 61

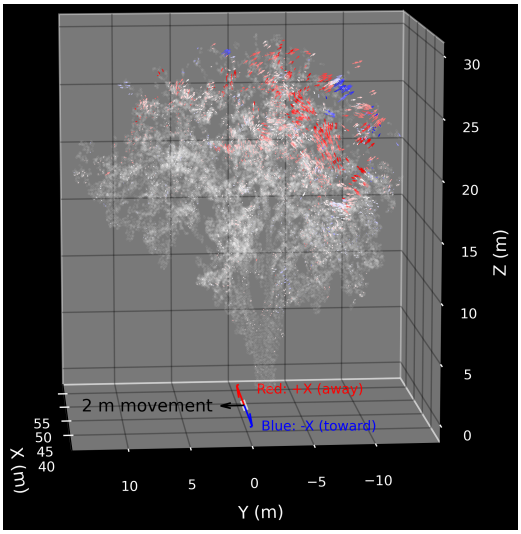

(f) Consecutive frame 61

Figure 4.19: Comparison showing the bias in the comparative frame analysis, compared to the consecutive frame analysis from the same scan

Temporal Resolution: 500 ms vs. 1000 ms Subsampling

Section 4.1.1 showed that objects covering less than 50% of the FOV could be sampled at 2 Hz instead of just 1 Hz. Scan 2 and 4 were used to test and assess the differences between these two temporal resolutions (500 ms and 1000 ms).

It is expected that by subsampling at 500 ms it will be possible to capture smaller and faster movements and be able to produce a smoother motion reconstruction. Although this will be at the cost of increased processing times and the possible appearance of scanning pattern artifacts due to the number of points being halved. In contrast, 1000 ms subsampling is expected to reproduce overall motion trends more accurately due to the larger denser point clouds making it possible to reconstruct the tree a lot more precise while missing out on short term ($<$1000 ms) movements.

In scan 2 (Figures 4.20a & 4.20b), which features a small tree of approximately 10 m height, both the 500 ms and 1000 ms subsampling results show a clear and well connected tree structure. The resulting scatter plots are detailed, even at the outer canopy edges where faster movements are expected to occur. This indicates that for smaller trees, or when the scanner is positioned close enough, higher temporal resolutions can be used to effectively measure short-period oscillations without severe degradation in spatial integrity

The results from scan 4 (Figures 4.20c & 4.20d), cover a taller birch tree of approximately 22 m in height, they demonstrate the limitations of higher temporal resolution processing of larger scanning areas. At 500 ms subsampling, detached or incomplete sections of the tree crown appear more frequently, and the apparent displacement magnitudes become less consistent across consecutive frames. This is an expected effect of halving the acquisition time per frame, larger trees require more time to be sufficiently covered so when this is reduced, the spatial coherence will be worse. Consequently, branches may appear to float and jump between frames which complicates the interpretation of motion.

The lower point densities at 500 ms subsampling also affects the stability of processing in PlantMove. The internal registration and displacement estimation steps rely on sufficient overlap and point distribution between frames. When the point density is reduced, the resulting displacement vectors become noisier and less reliable, particularly in sparsely sampled regions. This increases the chance of mismatched points and can lead to artificial motion artifacts in the results.

The results suggest that the optimal temporal resolution that can be used depends on both the size of the observed tree and the scanning geometry. For small or nearby trees that fit in the center 50% of the FOV, 500 ms subsampling provides valuable temporal detail with acceptable spatial completeness. For larger or more distant trees, 1000 ms subsampling preserves structural integrity of the tree in the point clouds and improves the accuracy of the motion quantification.

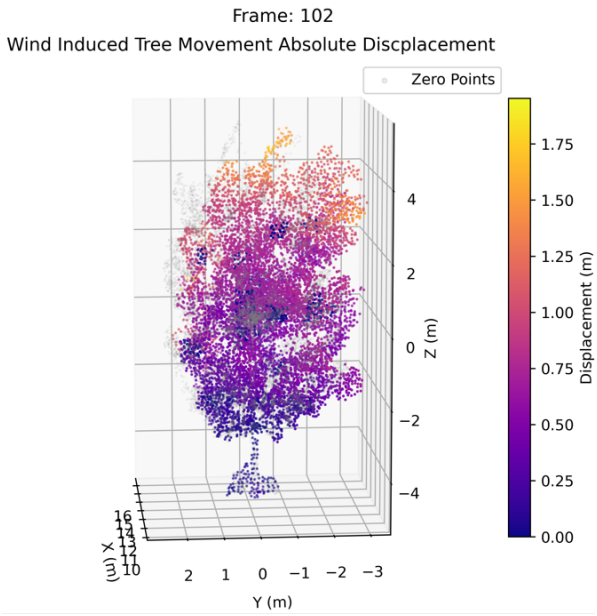

(a) Scatter plot from scan 2 of a frame subsampled at 500 ms

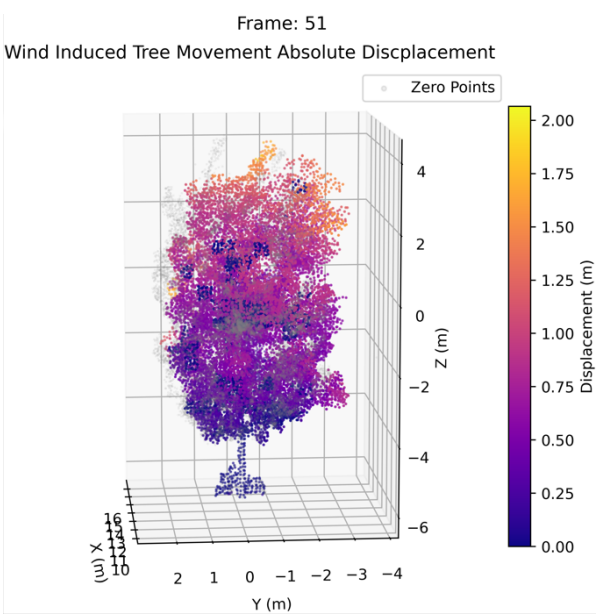

(b) Scatter plot from scan 2 of a frame subsampled at 1000 ms

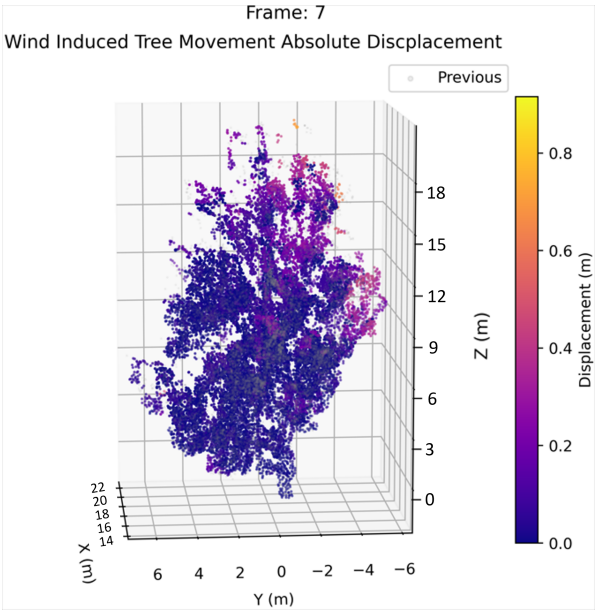

(c) Scatter plot from scan 4 of a frame subsampled at 500 ms

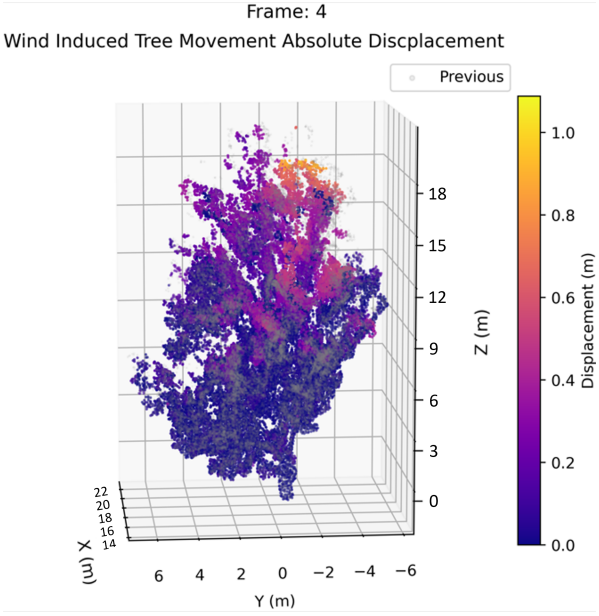

(d) Scatter plot from scan 4 of a frame subsampled at 1000 ms

Figure 4.20: 500 ms vs 1000 ms subsampling comparison plots

Quantifying Tree Movement

Using the processed point cloud frames, the displacement magnitude can be computed for every point in each frame of a scan. This provides a quantitative measure of tree motion per frame and complements the scatter and quiver plots introduced earlier.

By looking at the distribution of displacement values within a single frame or across the entire scan duration it becomes possible to distinguish between rigid and flexible tree sections, and assess the overall intensity of tree response under different wind conditions.

A simple way to summarise the tree motion of a single frame is to plot a histogram with the per point displacement magnitudes. An example is shown in Figure 4.21, which visualises the distribution of absolute point-wise displacements as calculated by PlantMove. The peak near zero indicates the stable regions (like the trunk and central branches), whereas the tail is represented by the more flexible canopy elements that undergo larger motion.

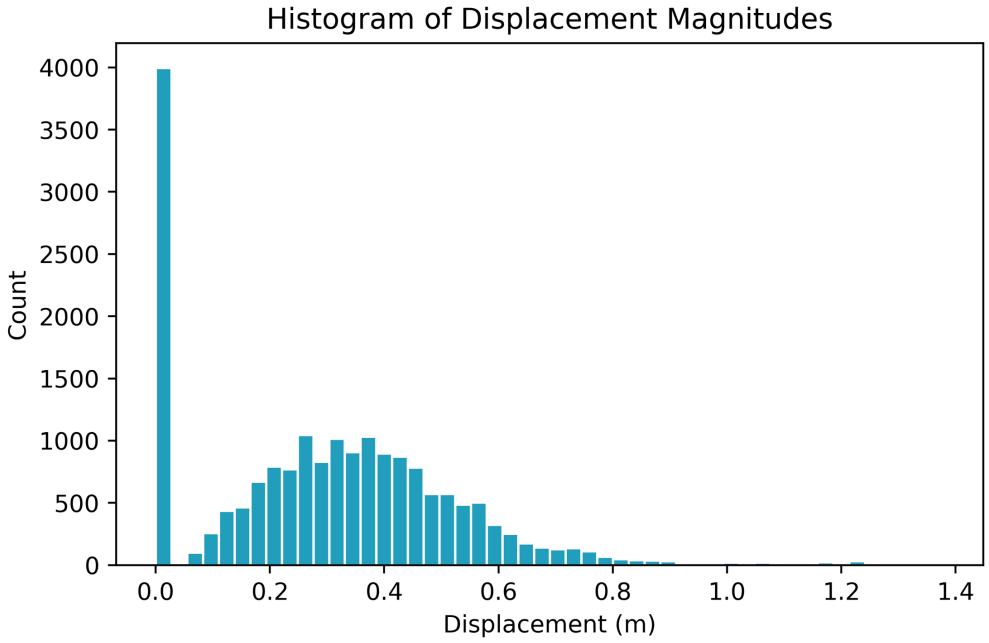

Figure 4.21: Example histogram showing the quantified movement magnitudes of the points in a single frame

The same frame can be visualised through the associated scatter and quiver plots in Figure 4.22. These figures illustrate how the histogram corresponds to the spatial structure of the tree, areas of larger displacement in the histogram align with the upper and outer canopy regions in the scatter plot, while the quiver plot provides additional insight into the movement directions.

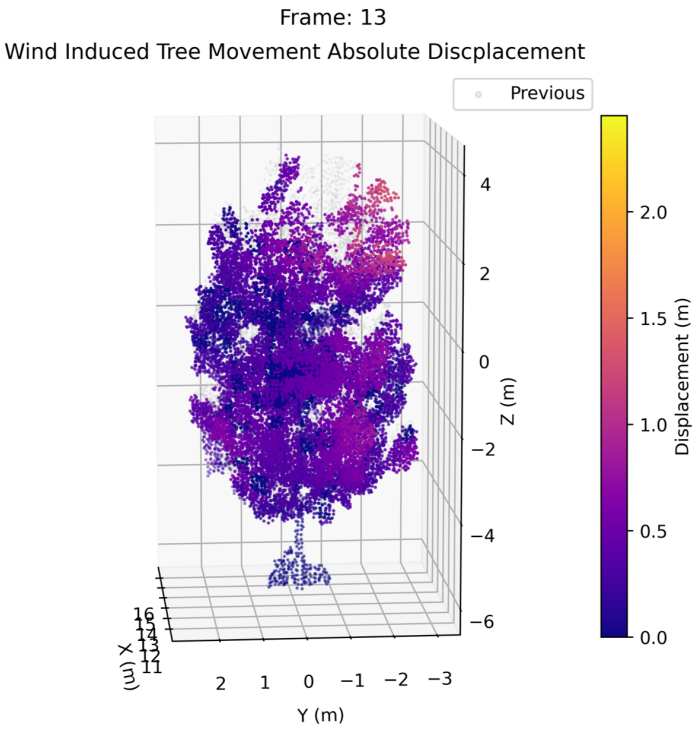

(a) Scatter plot of the same frame used to make the histogram showing the absolute displacement results in 3D

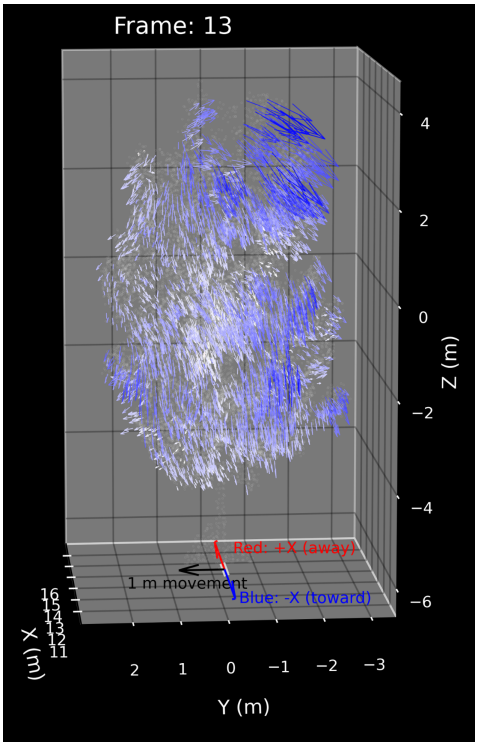

(b) Quiver plot of the same frame used to make the histogram showing the directional displacement results in 3D

Figure 4.22: Scatter and Quiver plots made from the same frame as the histogram in Figure 4.21

While histograms of individual frames are useful for summarizing global behaviour, they do not capture how movement varies vertically throughout the tree. To address this, the tree can be divided into horizontal slices to compute the mean displacement magnitude per height segment. Figure 4.23 shows an example of this slice-wise averaging for a single frame. This representation allows the vertical distribution of movement to be assessed more directly and highlights the structural stratification of wind-induced motion.

Extending this approach to the full duration of a scan results in time-averaged slice movement profiles, shown for two trees in Figures 4.24a and 4.24b. These averages provide an estimate of which height intervals experience the most motion over the entire scan sampling period. For both scan 1 and scan 2, the upper canopy consistently shows the largest mean displacements, while the lower sections remain comparatively stable. This coincides with the expected wind and structural behaviour, as wind speeds generally increase with height (even in urban areas [41]), and the upper branches are thinner and more flexible, so are expected to have larger movements. In contrast, the lower branches are usually thicker and more rigid, and the trunk remains the most structurally constrained as it is fixed in the ground.

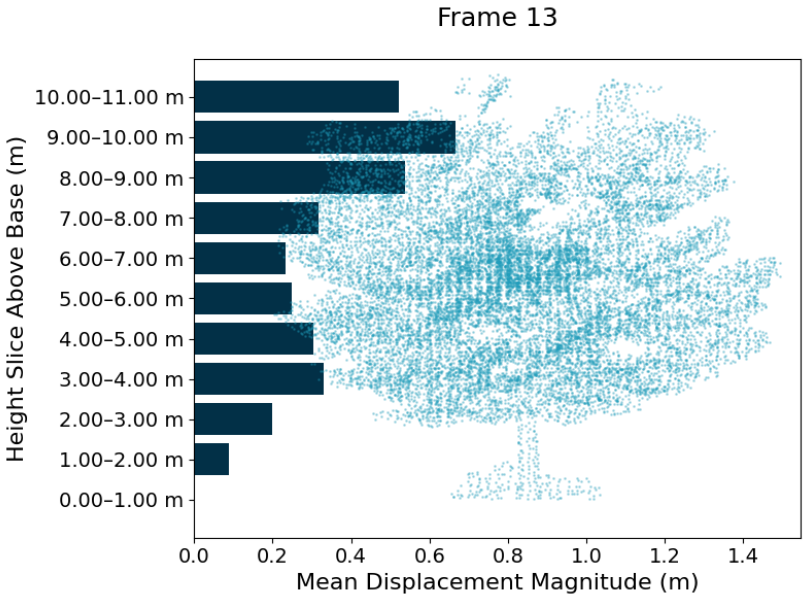

Figure 4.23: Single frame averaged tree movement per 1 m vertical slice of scan 2

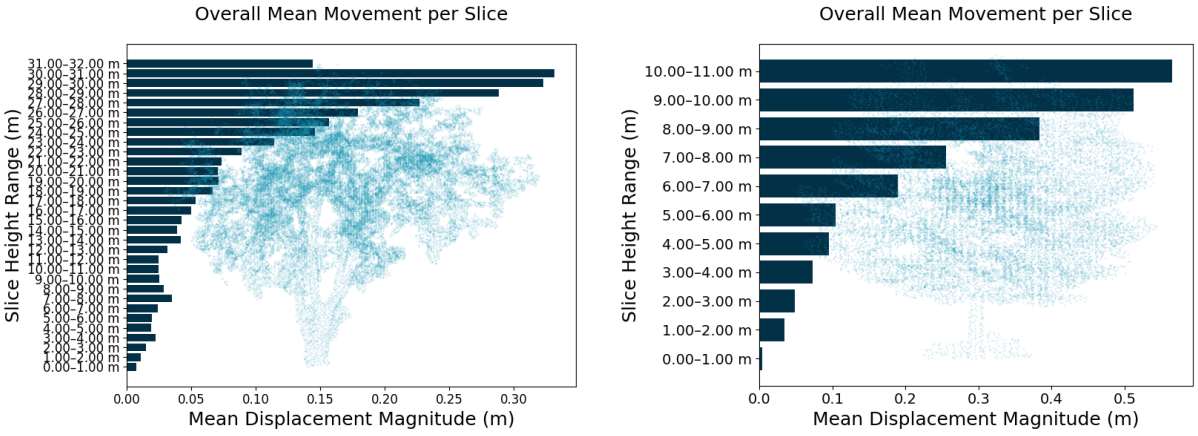

(a) Mean movement per 1 m horizontal slice of scan 1

(b) Mean movement per 1 m horizontal slice of scan 2

Figure 4.24: Mean movement per 1 m horizontal slices of full scans

The slice-based quantification offers a useful metric between full 3D displacement fields and single value statistics. It helps to highlight height dependent behaviour that might not be immediately apparent in the frame-by-frame displacement plots, and it provides a basis for comparing scans of trees with different morphologies, heights, or wind exposure conditions.

Future work could improve the quantification of movement by using more complex segmentation strategies. For example, vertical slices could be used next to the horizontal ones and the workflow could be extended to specifically cut out and compute motions of only specific tree sections (e.g., canopy, trunk, or branches) so that more specific and detailed motion analysis can be done.

Wind Data and Tree Motion

As noted earlier, wind speed and direction data were recorded during scans 2-4. The average wind characteristics during these measurements is summarised in Table 4.5.

Table 4.5: Average Wind characteristics recorded during the scans.

Name	Median speed (m/s)	Peak speed (m/s)	Average Direction (°)	Wind Direction (Cardinal)	Anemometer-Tree distance (m)
Scan 2	5.17	10.57	287	W	~ 11
Scan 3	2.05	3.67	121	SE	~ 20
Scan 4	2.34	5.97	249	WSW	~ 17

Scan Setup Positioning

The relative positioning of the AVIA, anemometer, and target tree varied between the scans. To help interpretation of the wind vs movement results, Figure 4.25 illustrates the configuration and main wind directions during scans 2-4.

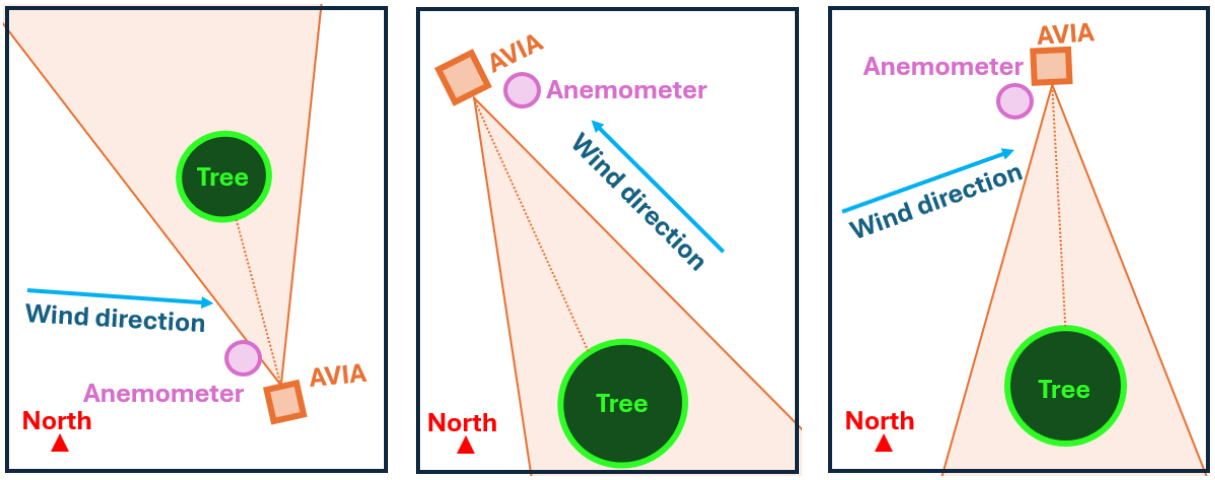

(a) Scan 2 placements (b) Scan 3 placements (c) Scan 4 placements

Figure 4.25: Scan position diagrams for scans 2, 3 & 4 showing AVIA, tree and anemometer positioning and wind directions (not to scale)

Wind Speed vs Mean Movement

By comparing wind speed with mean movement per frame, it is possible to assess the correlation between wind forcing and observed structural response. For this, comparatively processed data subsampled at 1000 ms was used. During scan 2 the strongest wind was measured so this scan will be used when visualising results, Figure 4.26 illustrates the comparison. The script used for calculating the correlations and generating the plots can be found on my GitHub [38]

Since the wind data was collected using an anemometer at a distance of ≈ 11 m from the tree, the measured movement and wind speed signals were not automatically aligned in time. A visual inspection revealed that peaks in movement consistently occurred after peaks in wind speed. To quantify this offset, a cross-correlation analysis was performed. This method systematically shifts the movement data relative to the wind data and calculates the correlation at each possible time lag, identifying the shift that produces the strongest correlation.

In this analysis, the mean movement values were first interpolated to match the timestamps of the wind speed data. Both signals were normalised by subtracting their respective means, removing constant biases and allowing a direct comparison of temporal trends. The cross-correlation between the detrended wind and movement time series revealed that the highest Pearson and Spearman correlations occurred when the movement signal was shifted by 5.08 s, indicating that the tree's response lagged behind the wind forcing by this amount.

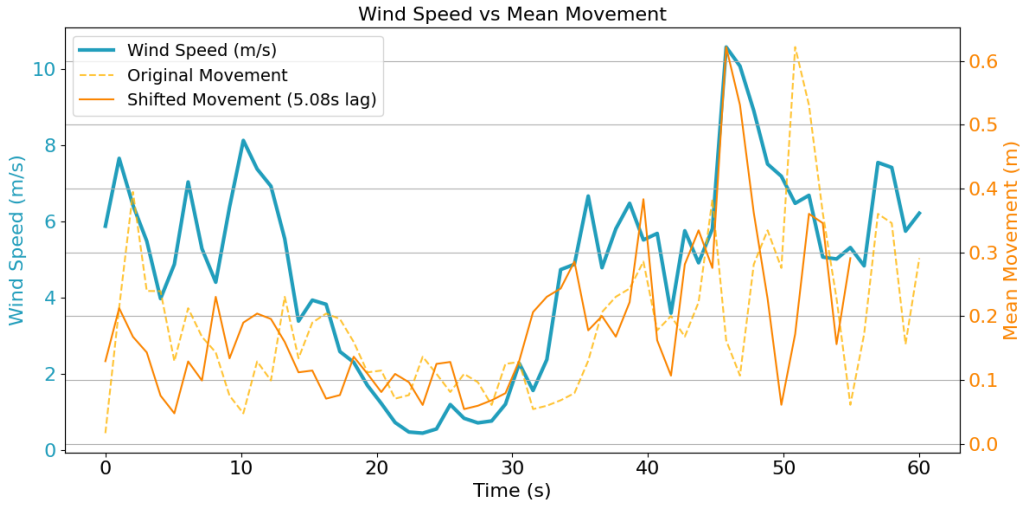

Figure 4.26: Comparison of wind speed and mean movement during scan 2. The movement data has been aligned using a cross-correlation lag of 5.08 s, accounting for the time delay between wind forcing and structural response.

This lag assessment is necessary because structural responses such as tree motion do not occur instantaneously after wind gusts. The delay arises from both the physical difference in propagation of wind between the anemometer and the tree (approximately 15 m apart) and the dynamic inertia of the tree itself, which has a response time before maximum displacement occurs. By shifting the movement data by the computed 5.08 s lag, the two datasets become temporally aligned, allowing a more direct comparison between wind forcing and structural motion.

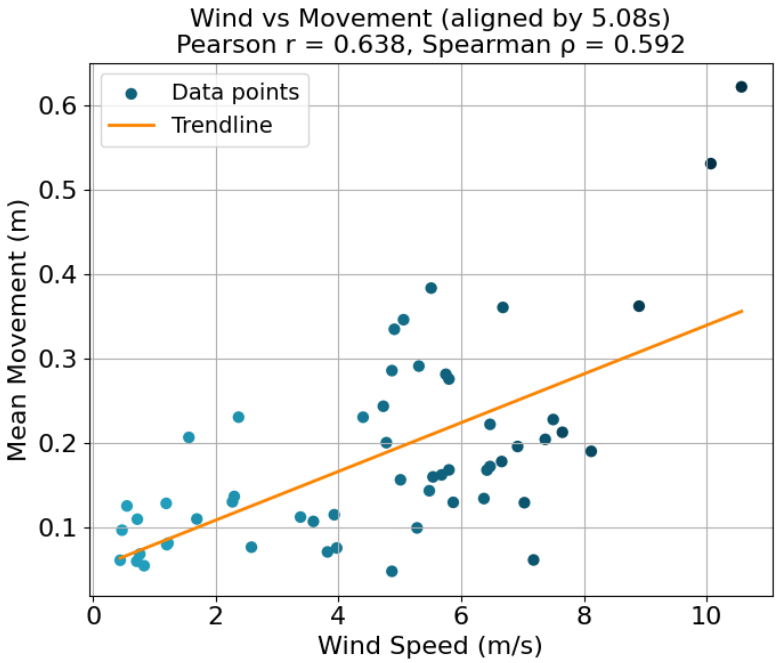

Figure 4.27: Scatter plot of wind speed and lag-corrected mean movement with fitted regression line

After this alignment, the Pearson correlation between wind speed and mean movement was calculated to be 0.638, and the Spearman correlation equals 0.592 (Figure 4.27). These values indicate a moderate positive relationship, confirming that higher wind speeds generally induce greater movement in the tree. Pearson correlation captures the linear relationship, while Spearman correlation accounts for potential non-linear effects or outliers, providing a clear assessment of the link between wind forcing and structural response.

The results from the other two scans with wind data are shown in Table 4.6. A positive lag indicates the movement is estimated to occur later than the measured wind, a negative lag means the movement was measured before the predicted corresponding wind reached the anemometer.

There is no correlation found between the wind and movement in scan 3, this can possibly be attributed to the very low wind conditions resulting in more small and random movements or the distance between the tree and the anemometer. The results from scan 4 show a lower moderate correlation, it must be noted that for the full scan duration (60 seconds) only 500 ms subsampled data was processed. As the tree was later found to be slightly too large for this temporal resolution (Figure 4.20), the lack of point-density could have had an influence on the quality of the PlantMove movement estimation.

Table 4.6: Average wind characteristics recorded during the scans.

Name	Pearson Correlation	Spearman correlation	Best Lag (s)
Scan 2	0.638	0.592	5.08
Scan 3	+- 0.1	+- 0.1	N/A
Scan 4	0.323	0.290	-5.1

Future measurement setups should measure the wind data for at least 10 seconds before and 10 seconds after the AVIA's scans are made so the a better lag estimation can be done. Next to this, future tests could reduce these uncertainties by positioning the anemometer closer to the structure or employing multiple anemometers to capture spatial wind variability more accurately. Such improvements would provide a clearer picture of structural movement to specific wind forcing events.

Wind Direction vs Movement Direction

Another aspect to examine is if the measured horizontal displacement of the tree relates to the recorded wind direction. In principle, when the wind blows from a certain direction, such as from left to right, the tree is expected to sway in that same direction, moving with the wind.

To visualise this relationship, wind rose plots [42] were created from the anemometer data collected during scans 2, 3 and 4 (see Figure 4.28). These plots are followed by figures showing the mean movement direction per frame derived from the LiDAR data of the corresponding scans (Figure 4.29).

In these mean movement direction plots, each bin points to the dominant direction of tree motion using the reference frame of the AVIA. For instance, in Figure 4.29b, where the wind approaches from behind the tree (see Figure 4.25b), the measured displacement points towards the AVIA, illustrating the expected response of the tree bending away from the incoming wind and in this case towards the AVIA.

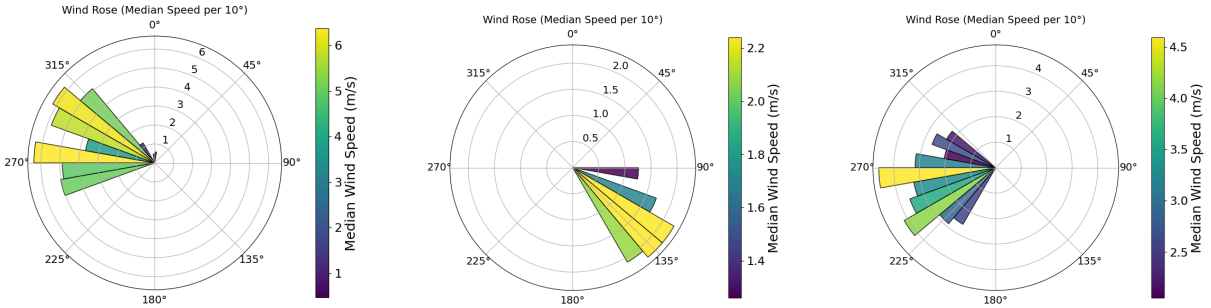

(a) Scan 2 (b) Scan 3 (c) Scan 4

Figure 4.28: Wind rose plots indicating the median speed and wind direction during a scan, bins pointing to 0° indicate wind blowing from the North and 180° indicates wind blowing from the South

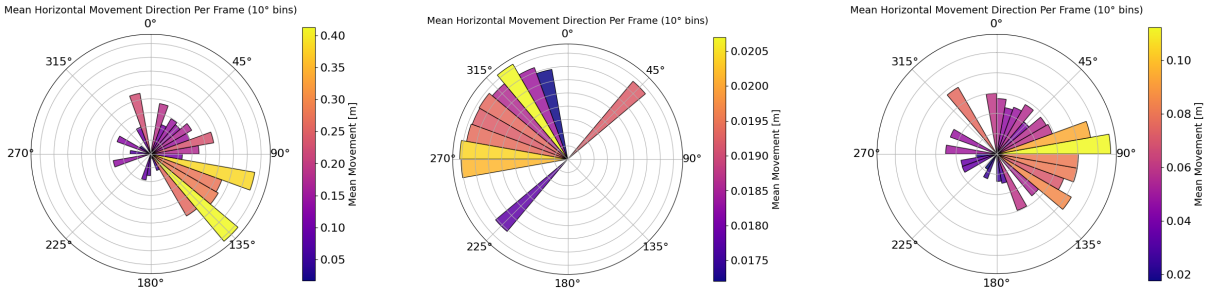

(a) Scan 2 (b) Scan 3 (c) Scan 4

Figure 4.29: Mean horizontal movement direction, bins pointing to 0° indicate movement towards the North and 180° indicates movement towards the South

By correcting the movement plots in Figure 4.29 so that the movement aligns with the same North as used for the anemometer, the measured horizontal movement seems to generally oppose the direction of the wind, just like expected. It does require knowing the pointing direction of the AVIA so that this angle can be corrected.

This is the most prevalent and defined for the higher wind speeds like for scan 2. The lower wind speeds in scan 3 and the resulting displacement directions are a little more dispersed, although they still generally point in the opposing direction as well.

When the scan data is processed consecutively (Figure 4.30), the movement between frames is more random as this method captures the smaller back and forward movements of the tree instead of the movement compared to a reference scan. Looking at a movement direction plot made with these results shows smaller and less unidirectional tree displacements.

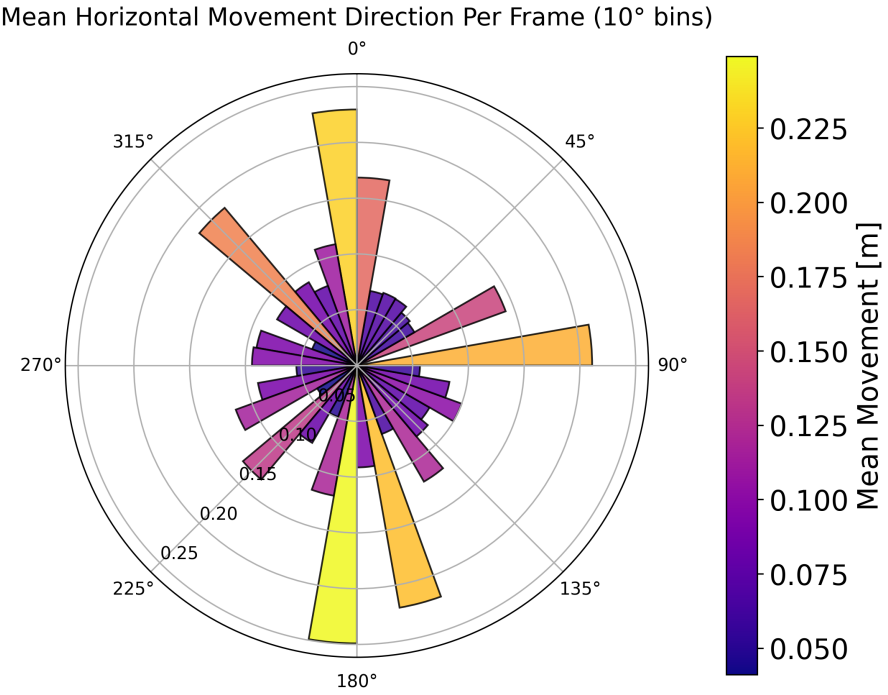

Figure 4.30: Mean horizontal movement direction of scan 2 consecutively processed data (500 ms)

While the current analysis only looks at horizontal (2D) displacement to match the mainly horizontal nature of wind flow, future work could include a full 3D motion analysis. By also looking at vertical displacement, it would be possible to study how different parts of the tree bend, for example how branches or the crown tilt or sag under wind load. This was not done here because the anemometer used only measured horizontal wind components. If a 3D anemometer would be used instead, the relationship between full 3D wind vectors and tree motion could be analysed.

4.3.2 Beach Scans

The scans discussed in this section are used as a proof of concept to evaluate whether the AVIA and setup can capture aeolian sand transport and dune erosion during windy conditions. The data was obtained as a bonus in between scans for other users, primarily to test and find out the capabilities of the AVIA for these specific applications. Despite the non-ideal setups, both tests produced measurable dynamics that demonstrate the potential of the setup on the beach.

Aeolian Sand Transport

Figure 4.31 shows a single snapshot taken during a windy period where airborne sand (shown in blue) is visible above the beach surface (shown in red). By fitting planes through both layers and comparing these, a mean separation of approximately 5 cm between the beach surface plane and the average plane of the saltation layer was found. While looking at the *.lvx* data in the Livox Viewer, a distinct layer points can be seen moving over the beach in waves, an example of this is uploaded as a video on my GitHub [38].

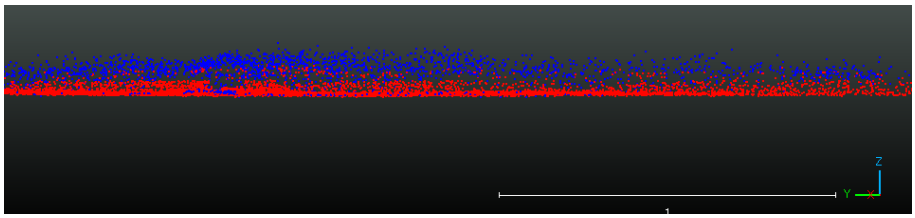

Figure 4.31: Aeolian sand transport (blue) over the beach (red) during a windy day

As discussed in the workflow section (Subsection 3.4.2) The two scan modes have strengths and weaknesses. The repetitive scan mode produces dense and temporally consistent returns in the target plane and therefore offers advantages for tracking the rapid vertical and lateral motion of the saltation layer. However, this mode lacks spatial context, because it samples in a single plane, it is more difficult to reference the saltation layer to the surrounding topography making it harder to fit the airborne layer in a full 3D scene. In contrast, the non-repetitive scans captured a wider spatial extent and therefore made it easier to place the saltation signal within a 3D context but this comes at the cost of fewer returns within the thin saltation layer itself.

Even from these test scans, several quantitative analyses can be planned for future, better worked out fieldwork tests:

- By fitting planes or by computing vertical profiles of return density, an estimation of the mean height and thickness of the active saltation layer can be done.
- Counting discrete sand particle returns per frame can provide a relative measure of airborne particle concentration. With calibration against physical sand traps or actual saltation sensors (like in [43]) this can be converted into mass flux.
- Repetitive scanning allows for an even higher temporal resolution analysis (up to 100 ms) of saltation-layer snapshots enabling the study of gust-driven waves of sand on their onset and short-term variability.

Dune Erosion

The manual dune erosion test results shown in Figure 4.32 demonstrate that the AVIA is capable of detecting centimetre-scale changes in surface elevation over a time interval. The removal of sand with a shovel created a measurable difference between the two 10-second scans.

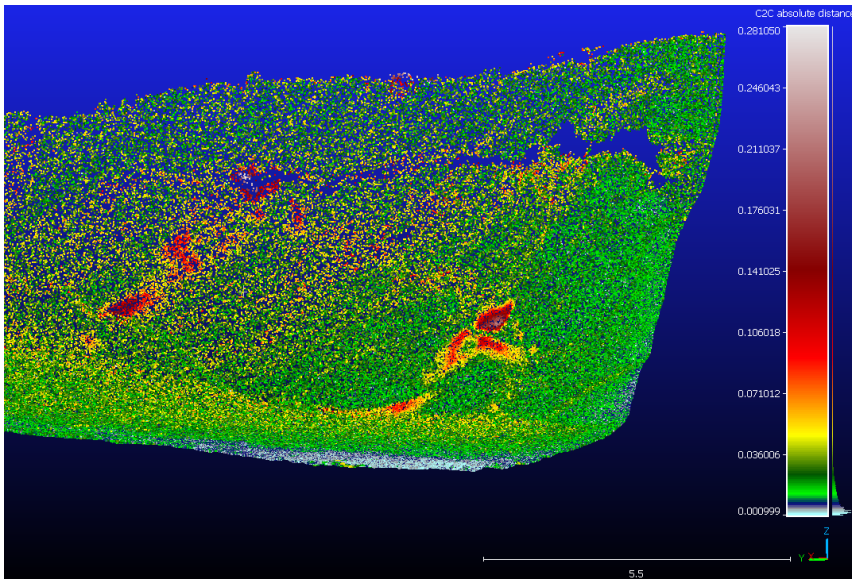

Figure 4.32: Dune erosion measurement test, sand dug with a shovel (in red) showing erosion can be measured

Following this initial detection of surface change, several useful analyses could be derived from the dataset. Most directly, the two point clouds can be converted into small digital elevation models, allowing for volume estimations of the removed or deposited sand. With higher point density or repeated scans, this approach could be extended to map spatial patterns of erosion and deposition of the dune.

Future work can also focus on integrating the AVIA with anemometers. When paired with reliable wind-speed measurements, the observed volumetric changes can be related directly to wind forcing, enabling investigation of the thresholds for sand transport as well as the relationship between wind conditions and patterns of erosion and deposition. In addition, using saltation sensors or conducting repeated scans over longer time periods rather than just a single artificial disturbance, would allow the detected erosion and sediment-transport signals to be used for a fully quantitative assessments of coastal morphological changes.

Chapter 5

Discussion

This chapter discusses the overall findings of the research and reflects on the Livox AVIA's suitability for static environmental sensing of dynamic scenes. It includes insights from the specifications verification, system deployment and field measurements to answer the research questions stated in Section 1.1. The discussion is divided in four parts, a discussion on the AVIA's strengths and limitations for environmental sensing, a short summary of the developed practical setup and workflows, a discussion of the deployment results finished by the comparison to other terrestrial LiDAR systems.

5.1 Strengths and Limitations of the Livox AVIA

The evaluation of the AVIA's technical characteristics (Section 3.1) and field performance (Chapter 4) reveal a set of distinctive strengths and practical constraints. These determine where and how the sensor is best applied within environmental sensing.

5.1.1 Strengths relevant for environmental sensing

Several of the AVIA's specifications stand out as advantageous for scanning dynamic environments. Its relatively high point rate of up to 720,000 PPS (triple return mode) produces dense point clouds, which at short and medium distances translates to high spatial coverage. This was particularly evident in the vegetation scans, where individual branches and canopy surfaces were resolved clearly within the inner 50% of the field of view.

Another important strength is the inclusion of an internal IMU. Even though environmental monitoring often involves static setups, the IMU proved to be capable of identifying periods with external disturbance from wind or vibration (Subsection 4.2.1. This allows motion filtering during processing to improve the overall data quality.

Practical aspects like the open-source Livox SDK [31] and accompanying documentation [20] allow for straightforward control of scanning, synchronization, and data export. This ease of integration, combined with its small size facilitates both manual and autonomous remote deployments together with the use of the COR (Section 3.3).

Lastly, the sensor assigns confidence levels to each sampling point to indicate potential noise, using separate flags to distinguish between low and medium confidence noise categories [20, Section 3.3].

By looking at the standard settings of the AVIA it seems that the sensor is typically set to the strictest noise threshold, meaning it is redundant to apply additional filtering strategies using the same point information from the *.lvx* files. In practice, most scans collected in fair weather conditions contain few erroneous returns, 'ghost points' appear but are rare, this suggests that the internal noise rejection is generally effective.

5.1.2 Limitations and their implications

Despite its strengths, the AVIA has several limitations that affect its applicability. The most notable is its non-uniform scan density. Due to the non-repetitive pattern, short-duration frames produce a 'petal-shaped' point distribution. For applications requiring spatially homogeneous coverage, temporal averaging or careful placement will be required.

Range performance also depends strongly on reflectivity and ambient light. Tests from Subsection 4.1.4 show that outside, targets further than 150 m already have significantly reduced detection rates compared to the maximum 320 m specification according to Livox. This restricts long-range monitoring of low reflectivity or high incidence targets.

Furthermore, the vertical beam divergence of 0.28° causes the laser footprint to expand considerably with distance. At 100 m, the footprint spans nearly 0.5 m vertically, limiting accuracy for small objects such as leaves or thin branches. For environmental sensing, this primarily constrains applications beyond short to mid-range (< 100 m).

5.1.3 Suitable application contexts

The AVIA's specifications make it notably effective for certain monitoring tasks. The small form factor and relatively low power consumption ($<$15 W) provide physical benefits. Furthermore, the high point density, fast FOV coverage (Section 4.1.1) and reasonable scan range align well with operations that requires fast repeated scanning. The paragraphs below outline representative domains where these features are most beneficial.

Vegetation and forestry monitoring

The combination of high point density and reliable short-medium range accuracy makes the AVIA suitable for studying vegetation dynamics. Applications could include canopy structure analysis, detecting seasonal changes in tree growth and short-term movements induced by wind. Because the non-repetitive scanning pattern concentrates point density in the centre of the field of view, repeated monitoring of scenes can yield highly detailed temporal datasets, especially when sensor alignment remains consistent over time.

Static Environmental Monitoring

The AVIA can be deployed in static setups to monitor both natural and man-made environments with high precision. In natural or semi-natural settings, it can track gradual but spatially complex changes, such as snow accumulation [6] or soil erosion. As it it capable of scanning at an interval of at least 1 Hz, it allows detection of short-term changes occurring over seconds. Its centimetre-level accuracy also makes it well suited for identifying small yet meaningful changes in surfaces, from landslide-prone slopes and

river banks [44] to other objects exposed to environmental stress. The ability to overlap repeated scans with minimal corrections (see Subsection 4.2.2 on stability) further provides confidence in using the sensor for long-term, repeated measurements like what is done in the AdaptCoast project [45].

Remote locations

The compact design and modest power requirements of the AVIA make it well suited for scanning in locations where infrastructure is limited or entirely absent. Power can be supplied from portable batteries or small solar panel systems, allowing for autonomous operation over extended periods. Its lightweight housing and minimal footprint further simplify transport and installation, even in constrained spaces or hard to reach terrain. The AVIA can be operated using low-power computing devices such as a Raspberry Pi (Subsection 3.3.2), which keeps overall system complexity low and facilitates the possibility for long-term field deployments in field stations. These characteristics together support the use of the AVIA in (remote) monitoring contexts where conventional LiDAR systems would otherwise be impractical.

5.1.4 Unsuitable applications

The AVIA's achievable temporal resolution (1-2 Hz) limits its ability to capture high-speed or short term dynamics. Motion occurring within the 500-1000 ms frame interval leads to distorted geometries or 'motion blur', as shown in Figure 5.1.

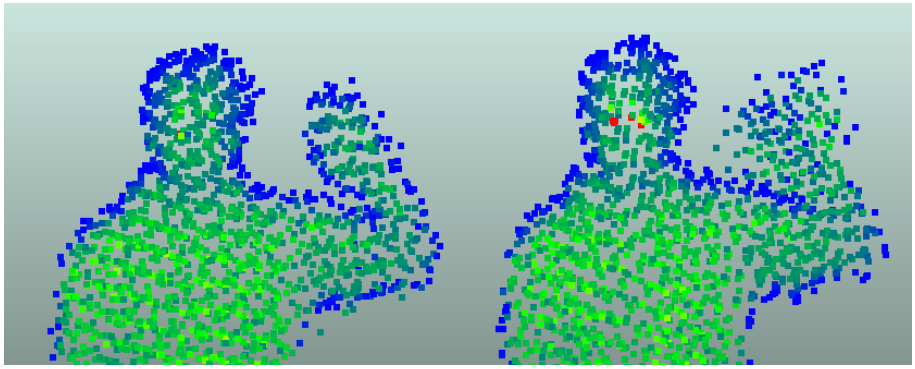

Figure 5.1: Movement distortion shown side by side using 1000 ms point cloud frames showing the difference between no movement (left) and movement (right)

Another example is tree branches moving through the FOV, due to the shape and timing of the non-repetitive scanning pattern, parts of a moving branch will be captured over multiple, spatially inconsistent positions over a single scan. The resulting geometry will resemble stretched or fragmented objects rather than clear, sharp shapes. In practice, this 'motion blur' will limit the AVIA's use for fast moving targets or targets moving with repeat cycles shorter than the frame rate. Since their true positions cannot be reconstructed reliably at these frame rates.

Additionally, at larger distances the expanding footprint and decreasing point density restrict its use for fine-scale measurements or precision engineering applications (Subsection 3.1.4). While using the AVIA is possible for general canopy or terrain monitoring, it is limited in use for applications beyond 100-150 meters in range (Subsection 4.1.4). For cases that require higher accuracy or range, more expensive LiDAR sensors with smaller beam divergence and higher powered lasers remain more appropriate.

5.2 Set-up and Workflow

The developed deployment configuration and data-processing workflow sections, Subsection 3.4.1 & Subsection 3.4.2 address the answers for sub-question 4 on practical requirements and optimization of the AVIA for static monitoring.

System design and practicality

The combination of the AVIA with the COR and anemometer created a low-cost, self-contained measurement system capable of both manual and autonomous operation. From a TRL perspective, this shows advancement from an idea to an experimental configuration and a field-demonstrable and tested prototype (TRL 7–8). The modular design ensures the setup can be adapted for different environmental parameters without significant reconfiguration. In practice, this system has met the operational needs for outdoor data collection, it is portable, easy to set up and use and its low total power draw makes longer term operations feasible even on battery or solar power.

Workflow optimization

The introduced workflow for the wind induced tree movement work includes frame segmentation, PlantMove processing, and subsequent visualization. It proved to be effective at deriving tree motion information from the raw *.lvx* data and the combination of consecutive and comparative frame analysis offered complementary insights. Consecutive registration captured smaller, stepwise displacements, while comparative registration quantified overall deformation relative to a baseline frame. The discussion in Subsection 4.3.1 showed that selecting a proper reference frame (preferably during low wind conditions) minimises bias in comparative analyses.

The Python scripts for visualization and correlation analysis [38] further improve interpretability, enabling the use of wind data and calculation of the corresponding correlation metrics. These steps form a repeatable workflow for future studies using the AVIA for measuring tree movement.

For the scans on the beach a full consistent workflow should still be worked out. The initial results show that dynamic processes on that occur on the beach can be measured but the most optimal way to measure and process should still be figured out.

5.3 Fieldwork Results

The tree-movement and morphological beach change measurement results in Chapter 4 demonstrate the AVIA's capability to capture dynamic structural responses to wind at centimetre-scale precision with temporal resolutions of up to 500 ms.

5.3.1 Wind induced tree motion

The correlation analysis between wind speed and mean movement confirms a moderate, positive relationship, stronger wind speeds consistently result in greater displacement. A lag correction is required to account for both physical separation between sensors and the delayed mechanical response of the tree.

Overall, these findings indicate that the AVIA can reliably quantify relative deformation magnitudes induced by environmental forcing.

The observed directional correspondence between wind and displacement (Figures 4.284.29) further validate this. For the scanned trees, the measured motion vectors generally opposed the wind direction as expected, demonstrating that the AVIA is capable of capturing deformation behaviour.

Temporal resolution and scan coherence

Tests comparing 500 ms and 1000 ms subsampling intervals considered the trade-off between temporal and spatial completeness. While 500 ms frames captured faster and shorter movements, they suffered from incomplete coverage and noisier displacement estimates, especially in large trees extending beyond the dense central FOV. At the same time, 1000 ms subsampling preserved geometry and yielded smoother motion vectors losing out on detecting shorter movements. It assures that for typical environmental monitoring where physical motion occurs on the order of seconds, 1 Hz full-frame capture represents an optimal balance between temporal resolution and spatial integrity.

5.3.2 Morphological Changes On The Beach

The beach tests indicate that the AVIA can capture both aeolian transport and small-scale morphological change. The saltation-layer observations show clear vertical separation from the surface and reveal wave-like bands of airborne sand. The comparison of scan modes confirms their trade-offs, repetitive scans provide high temporal snapshots of fast-moving transport, while the non-repetitive scans offer better necessary spatial context at lower temporal resolutions.

The dune-erosion test further shows that the AVIA could resolve small and isolated surface changes, the manually removed sand scans produced a clear elevation difference results between scans showing that the scanner is promising for use in these monitoring applications.

5.4 Expected results from other LiDAR Scanners

To better understand the Livox AVIA's performance in dynamic, outdoor fieldwork, it is valuable to compare its specifications and design with other LiDAR scanners commonly available for research or industrial use. For this purpose, three other systems were considered: the Livox Mid-70, the Velodyne VLP-16, and the Leica P40.

The Livox Mid-70 was selected as it most closely resembles the AVIA as it is its predecessor, allowing for direct comparison within the same product line. The Leica P40 was chosen because it is available at the faculty, enabling a comparison based on first-hand experience. The Velodyne VLP-16 was included as a similarly compact and affordable LiDAR unit from another manufacturer, providing an external reference point.

Each of these scanners can be used in related contexts such as environmental monitoring, object tracking, or structural documentation, their key parameters are summarised in Table 5.1 and Table 5.2.

Table 5.1: LiDAR scanners: Price, Size, Weight, and IP Rating [9][46][47][12]

Manufacturer	Scanner	Price (new in 2025)	IP Rating	Size (cm)	Weight (kg)
Livox	AVIA	1,600	67	9.1 x 6.1 x 6.5	0.498
Livox	Mid-70	1,100	67	9.7 x 6.4 x 6.3	0.58
Leica	P40	60,000	54	23.8 x 35.8 x 39.5	13.05
Velodyne	VLP 16	<1,000	67	10.3 x 10.3 x 7.1	0.83

Table 5.2: LiDAR scanners: Technical specifications [9][46][47][12]

Scanner Name	Scan Type	FOV (h x v deg)	Range Error	Range (m)	Power (W)	PPS (single return)	+90% FOV Coverage (s)
AVIA	Non-Repetitive	70.4 x 77.2	2 cm at 20 m	320	9	240,000	1
Mid-70	Non-Repetitive	70.4 x 70.4	2 cm at 20 m	260	8	100,000	1.6
P40	Non-Repetitive	360 x 290	0.5 mm at 50 m	270	∼60	1,000,000	>10
VLP 16	Repetitive	360 x 30	3 cm	100	8	300,000	NA (lines)

As a LiDAR scanner, the AVIA sits between compact, lightweight and affordable scanners and large, high-precision terrestrial scanners. Its non-repetitive scanning pattern and relatively high PPS rate (240,000) allow it to reach over 90% FOV coverage in about one second. This combination enables it to record dynamic processes such as wind-induced tree motion, where both spatial completeness and short temporal intervals are important.

The Livox Mid-70 has almost the same non-repetitive scanning pattern as the AVIA but operates at a significantly lower PPS rate (100,000), resulting in longer FOV coverage times. It is slightly smaller and cheaper than the AVIA and could be suitable for slower changing targets. However, its lower sampling rate makes it less effective for scanning short term movement and small deformations. Using the Mid-70 for the scanning of trees would likely lead to reduced motion detail and less stable displacement results. It is however, a valuable option for applications that do not require sub second temporal resolutions but do require a reliable small and practical setup.

The Leica P40 differs substantially from the other scanners. It provides extremely high spatial accuracy (down to 0.5 mm at 50 m) and a very large FOV, but its size, weight (13 kg), and power requirements make it impractical for mobile setups like the COR. Next to this, the P40 requires a considerably longer time to complete a scan, which prevents the capture of any short-term motion. It is therefore best suited to static or slowly changing scenes where precision is more important than high temporal resolutions.

The Velodyne VLP-16 is a line scanner with 16 scan lines. While it can scan up to 300,000 PPS, its vertical FOV is limited to 30°. The repetitive scanning pattern is highly directional, which is practical for mapping or navigation tasks where relative motion is along a single axis, but it is not really suited for scanning complex, irregular motion such as tree sway. The repetitive line structure would result in uneven point distributions and limited coverage, making temporal motion analysis unreliable.

Overall, the Mid-70 and VLP-16 are similar to the AVIA in size, power consumption, and environmental resistance (IP67), but neither provides the same coverage speed. The P40 remains valuable for generating high-accuracy reference models, yet its scanning speed and operational requirements (big batteries) make it unsuitable for bringing along easily. In this context, the AVIA offers a good compromise between temporal resolution, spatial coverage, and portability. It performs well for observing motion on sub-second timescales while maintaining sufficient structural completeness. Future work could focus on controlled, experiments with these or other comparable LiDAR scanners under identical conditions to further quantify their differences.

Chapter 6

Conclusions and Future Work

6.1 Conclusion

In this chapter the main research and corresponding sub-questions will be addressed. The goal of this MSc thesis was to assess the added value of the Livox AVIA LiDAR sensor for terrestrial applications in dynamic environments. Through a combination of controlled specification tests, the development of a setup prototype, and field experiments, the findings show that the AVIA is a highly capable sensor for capturing dynamic natural processes at close- to mid-range distances. Across testing, the AVIA had a reliable performance when used in stationary monitoring setups. The validated specs, stable behaviour in windy outdoor conditions and successful demonstrations in both the wind-induced tree movement study and the beach morphology tests confirm that the sensor provides accurate and dense enough point clouds to measure short-timescale environmental dynamics. Combined with the Central Observations Recorder (COR), the setup proved to be functional in manual and autonomous deployments, showing its added value for future (long-term) field operations and concluding that a TRL level of at least 7 has been achieved.

Overall the discussed properties make the AVIA well suitable for dynamic environmental monitoring tasks that would be impractical with traditional terrestrial laser scanners. Its compact design, low power consumption, and high temporal sampling-rate allow it to fill a practical gap between slow, highly accurate TLS systems and comparable fast, lightweight automotive or robotics LiDAR units. While limitations like low precision at higher ranges or the non-uniform FOV coverage will limit applicability for certain operations, its strengths make it possible to measure dynamic environments in higher temporal resolutions than possible with other TLS.

1. How do the factory-provided specs compare to the real-world performance?
The AVIA's real-world performance closely matches or exceeds most factory specifications. Distance accuracy tests showed the distance random error to consistently be below 1 cm at a distance of 20 m, which outperforms the stated 2 cm spec at this range. The non-repetitive scanning mode reaches approximately 92% FOV coverage within 1000 ms, which is slower that the provided time of 800 ms. Point density analysis revealed a higher concentration in the center of the FOV with a decreasing density toward the FOV edges, which is caused by the shape of the non-repetitive scan pattern. The sensor operates effectively within a practical range of 2-100 m, with returns becoming sparse beyond 150 m due to laser beam divergence and the influence of larger incidence angles.

2. What are the main use cases for the AVIA sensor in environmental sensing applications?
The AVIA's strengths are high temporal sampling (at least 1 Hz), producing dense short-range point clouds, a small form factor and an integrated IMU. These make it well suited for static monitoring of fast dynamic environmental processes. It performs very well in applications where movement occurs in the order of seconds, like for wind-induced tree motion, small-scale structural deformations, or rapid surface changes. Its form-factor and low-power operation make it suitable to be used in (long-term) monitoring in remote environments where traditional expensive and bulky TLS systems are impractical to use. Field experiments demonstrated that the AVIA can capture tree deformation, airborne sand transport, and short-term morphological changes of a dune. These tests confirmed its usefulness in studying dynamic processes that benefit from repeated, rapid scanning.

3. How do environmental factors like vibrations influence the performance and accuracy of the AVIA?
Tests on the influence of external vibrations showed that small, short vibrations like those caused by wind showed to have a negligible effect on the random distance error. The onboard IMU was shown to be able record these disturbances so that in future work post-processing, frame exclusion or correction of data can be performed. Using findings from literature, it is clear that airborne particles can have a much stronger effect. Rain, dust, and sand particles cause signal attenuation and backscatter, reducing point the overall density and causing noise in the measurements. The AVIA maintained stable and consistent scans in normal and windy outdoor conditions, indicating that small vibrations are not a major concern but that airborne particles will be a source of performance degradation.

4. What are the practical requirements for deploying the AVIA in *static* setups for capturing *dynamic* environments?
Practical requirements for the deployment of the setup include, water-proofing, power and sensor management, and data handling. A basic autonomous test demonstrated that the COR and AVIA can operate without any issues for 36 hours, this test also showed that stable alignment and consistent scanning can be maintained without the need for recalibration. The COR integrates the AVIA with a Raspberry Pi for power management, controllability (enabling the AVIA to be used in both manual and autonomous modes) and supports integration of supplementary sensors such as anemometers. The required data processing workflow steps like the transformation to more generic file formats and making it possible to achieve temporal subsampling are used to achieve reliable motion quantification.

5. How does the AVIA's design compare with other LiDAR systems in similar use cases?
Compared to other compact LiDAR sensors such as the Livox Mid-70, the AVIA offers faster coverage of a circular FOV and higher effective point density in dynamic-monitoring contexts. The Mid-70's lower point rate will limit its ability to resolve fast movements, while the VLP-16's narrow vertical FOV and repetitive line scanning structure will reduce its overall coverage and usability in detecting irregular environmental motion. High-end terrestrial laser scanners like the Leica P40 provide superior spatial accuracy and complete coverage but are heavy, slow, and power hungry making them harder to use when scanning dynamic processes. The AVIA occupies a middle ground between the discussed sensors, it offers a compromise between temporal resolution, portability, and ease of use that makes it well suited for statically scanning dynamic environments.

6.2 Limitations

Regardless of the results mentioned above, several limitations should be acknowledged. The non-uniform scan pattern remains the primary constraint when homogeneous coverage is required and the point density decreases rapidly. Furthermore, the influence of strong vibrations or extreme environmental conditions such as heavy rain could not be fully quantified within the scope of this thesis. Although the internal IMU was effective for motion logging, its lower sensitivity restricts the detection of small/subtle orientation drifts over longer durations. Finally, while the COR system proved functional, its current power source (batteries) and data storage capacity limit the duration of fully unattended operations meaning more careful consideration of battery and storage is recommended.

6.3 Future work

Future work could focus on three complementary directions:

Quantifying sensor movement thresholds: The integration of IMU data into the data processing workflow could make it possible to define explicit vibration or motion thresholds for frame exclusion. Establishing these thresholds would enable automatic quality filtering and enhance the temporal consistency of point-cloud time series.

Multi-sensor integration: Combining the AVIA with additional anemometers or more AVIA units would allow for cross-validation of wind and full 3D coverage of object motion and deformation patterns. These multi-sensor networks would improve both accuracy and spatial coverage, and provide better insights of the measured environmental processes.

Extended duration field tests: Extended testing across different settings (e.g., coastal dunes or in urban areas) are needed to evaluate the AVIA's long-term mechanical stability, resistance to environmental stress, and maintenance/upkeep requirements.

Next to these main directions, additional work could also explore automated scan scheduling and real-time data streaming to further improve the AVIA's use in dynamic monitoring setups. Automated scheduling would allow the system to adapt scanning frequency based on environmental triggers, such as changes in wind speed, which could optimise power usage and data relevance during long-term deployments. Real-time data streaming and connectivity, enables continuous remote supervision and control and allows for faster data retrieval. Finally, integrating the AVIA with a camera and other sensors would enrich the contextual interpretation of LiDAR data. Combining the obtained 3D structure with optical or spectral information on surface properties could help improve understanding of the measured dynamic processes.

Bibliography

[1] Actueel Hoogtebestand Nederland. "Ontwikkeling van AHN". In: (Mar. 27, 2023). URL: https://www.ahn.nl/ontwikkeling-van-ahn.

[2] J.L. Irish and T.E. White. "Coastal engineering applications of high-resolution lidar bathymetry". In: *Coastal Engineering* 35.1 (1998), pp. 47–71. ISSN: 0378-3839. DOI: https://doi.org/10.1016/S0378-3839(98)00022-2.

[3] L Langhorst. *A decade of developments in Lidar technology*. Dec. 12, 2024. URL: https://www.gim-international.com/content/article/a-decade-of-developments-in-lidar-technology.

[4] Livox. *Downloads - Avia LiDAR sensor - Livox*. 2024. URL: https://www.livoxtech.com/avia/downloads.

[5] P. Trybała et al. "Designing And Evaluating A Portable LiDAR-Based SLAM System". In: *The International Archives of the Photogrammetry, Remote Sensing and Spatial Information Sciences* XLVIII-1/W3-2023 (2023), pp. 191–198. DOI: 10.5194/isprs-archives-XLVIII-1-W3-2023-191-2023.

[6] P. Ruttner-Jansen et al. "Monitoring snow depth variations in an avalanche release area using low cost LiDAR and optical sensors". In: *EGUsphere* 2024 (2024), pp. 1–20. DOI: 10.5194/egusphere-2024-744.

[7] YellowScan. *YellowScan Mapper+: Compact & powerful LiDAR system for UAVs*. 2024. URL: https://www.yellowscan.com/products/mapper-plus/.

[8] M.O.N. Brandwijk. "UAV LiDAR Point Cloud Acquisition and Quality Assessment". MA thesis. TU Delft, 2023. URL: https://resolver.tudelft.nl/uuid:52c1a143-1f89-4abf-bfcc-473ff98e4163.

[9] Livox. *Specs - Avia LiDAR sensor - Livox*. 2024. URL: https://www.livoxtech.com/avia/specs.

[10] Y Waykar. "Lidar technology: A comprehensive review and future prospects". In: *International Journal of Emerging Technologies and Innovative Research* 9.7 (2022), h164–h172.

[11] RIEGL. *RIEGL VZ-2000I: Long Range, Very High Speed 3D Laser Scanner - RIEGL Austria*. URL: https://www.riegl.com/en-austria/products/detail/riegl-vz-2000i (visited on 11/13/2025).

[12] Leica. *Leica ScanStation P30/P40*. Nov. 11, 2020. URL: https://www.google.com/url?sa=t&rct=j&q=&esrc=s&source=web&cd=&cad=rja&uact=8&ved=2ahUKEwjJ5urm39iQAxXZ2QIHHT_hASsQFnoECBoQAQ&url=https%3A%2F%2Fleica-geosystems.com%2F-%2Fmedia%2Ffiles%2Fleicageosystems%2Fproducts%2Fdatasheets%2Fleica_scanstation_p30-p40_civil_ds.ashx%3Fsc_lang%3Den%26hash%3D4246F396123887148A57B797F039AED4&usg=AOvVaw1R2L-dsTmFQaR-zPVe8geU&opi=89978449 (visited on 11/04/2025).

[13] Xin Wang et al. "The evolution of LiDAR and its application in high precision measurement". In: *IOP Conference Series Earth and Environmental Science* 502.1 (May 1, 2020), p. 012008. DOI: 10.1088/1755-1315/502/1/012008.

[14] Lotte de Vugt et al. "Permanent Laser Scanning and 3D Time Series Analysis for Geomorphic Monitoring using Low-Cost Sensors and Open-Source Software". In: vol. XLVIII-G-2025. Aug. 2025. DOI: 10.5194/isprs-archives-XLVIII-G-2025-359-2025.

[15] M. T. Perks et al. "An Evaluation of Low-Cost Terrestrial Lidar Sensors for Assessing Hydrogeomorphic Change". In: *Earth and Space Science* 11.8 (2024), e2024EA003514. DOI: https://doi.org/10.1029/2024EA003514. URL: https://agupubs.onlinelibrary.wiley.com/doi/abs/10.1029/2024EA003514.

[16] Livox. *Avia LiDAR sensor - Livox*. URL: https://www.livoxtech.com/avia (visited on 04/04/2025).

[17] Mathieu Dassot, Thiéry Constant, and Meriem Fournier. "The use of terrestrial LiDAR technology in forest science: Application Fields, Benefits and Challenges". In: *Annals of Forest Science* 68 (Aug. 2011), pp. 959–974. DOI: 10.1007/s13595-011-0102-2.

[18] A. Ortiz Arteaga, D. Scott, and J. Boehm. "INITIAL INVESTIGATION OF A LOW-COST AUTOMOTIVE LIDAR SYSTEM". In: *The International Archives of the Photogrammetry, Remote Sensing and Spatial Information Sciences* XLII-2/W17 (2019), pp. 233–240. DOI: 10.5194/isprs-archives-XLII-2-W17-233-2019.

[19] Virgil-Florin Duma and Alexandru Schitea. "Laser scanners with rotational Risley prisms: Exact scan patterns". In: *Proceedings of the Romanian Academy - Series A: Mathematics, Physics, Technical Sciences, Information Science* 19 (Feb. 2018), pp. 53–60.

[20] Livox. *Livox Wiki — Livox wiki 0.1 documentation*. URL: https://livox-wiki-en.readthedocs.io/en/latest/index.html (visited on 10/02/2025).

[21] Shashank Kishore Bhandary et al. "Ambient light level varies with different locations and environmental conditions: Potential to impact myopia". In: *PLoS ONE* 16.7 (July 7, 2021). DOI: 10.1371/journal.pone.0254027.

[22] Bosch. *Inertial Measurement Unit BMI088*. URL: https://www.bosch-sensortec.com/products/motion-sensors/imus/bmi088/ (visited on 04/04/2025).

[23] S.S. Soudarissanane. "The Geometry of Terrestrial Laser Scanning; Identification of Errors, Modeling and Mitigation of Scanning Geometry". PhD thesis. Delft University of Technology, 2016. URL: https://resolver.tudelft.nl/uuid:b7ae0bd3-23b8-4a8a-9b7d-5e494ebb54e5.

[24] Esser Test Charts. *TE109 Log. Gray Scale Test Chart*. URL: https://www.image-engineering.de/products/charts/all/447-te109 (visited on 10/02/2025).

[25] M. Kuschnerus, D. Schröder, and R. Lindenbergh. "ENVIRONMENTAL INFLUENCES ON THE STABILITY OF A PERMANENTLY INSTALLED LASER SCANNER". In: *The International Archives of the Photogrammetry, Remote Sensing and Spatial Information Sciences* XLIII-B2-2021 (2021), pp. 745–752. DOI: 10.5194/isprs-archives-XLIII-B2-2021-745-2021. URL: https://isprs-archives.copernicus.org/articles/XLIII-B2-2021/745/2021/.

[26] *LiDAR Comparison: 905nm vs. 1550nm*. URL: https://www.lumimetric.com/en/new/905nm-and-1550nm-LiDAR-Laser-Comparison.html (visited on 10/09/2025).

[27] A. Filgueira et al. "Quantifying the influence of rain in LiDAR performance". In: *Measurement* 95 (2017), pp. 143–148. ISSN: 0263-2241. DOI: https://doi.org/10.1016/j.measurement.2016.10.009. URL: https://www.sciencedirect.com/science/article/pii/S0263224116305577.

[28] Haojie Lian et al. "LIDAR Point Cloud Augmentation for Dusty Weather Based on a Physical Simulation". In: *Mathematics* 12.1 (2024). ISSN: 2227-7390. DOI: 10.3390/math12010141. URL: https://www.mdpi.com/2227-7390/12/1/141.

[29] Sebastien Michaud, Jean-François Lalonde, and Philippe Giguere. "Towards characterizing the behavior of LiDARs in snowy conditions". In: *International Conference on Intelligent Robots and Systems (IROS)*. 2015, pp. 21–25.

[30] Rijksdienst voor Ondernemend Nederland. *Technology Readiness Levels (TRL)*. URL: https://www.rvo.nl/onderwerpen/trl#4-fasen/%2C-9-technology-readiness-levels (visited on 10/16/2025).

[31] Livox-Sdk. *GitHub - Livox-SDK/Livox-SDK: Drivers for receiving LiDAR data and more, support Lidar Mid-40, Mid-70, Tele-15, Horizon, Avia.* URL: https://github.com/Livox-SDK/Livox-SDK (visited on 10/07/2025).

[32] Raspberry Pi. *Raspberry Pi 4*. URL: https://www.raspberrypi.com/products/raspberry-pi-4-model-b (visited on 10/28/2025).

[33] Gill Instruments. *WindSonic – Gill Instruments*. URL: https://gillinstruments.com/compare-2-axis-anemometers/windsonic-2axis (visited on 10/28/2025).

[34] Peli. *1450EU Protector Case — Peli*. URL: https://www.peli.com/be/en/product/cases/protector/1450eu/?sku=1450-001-150E (visited on 10/28/2025).

[35] Agatha Zamuner. "Understanding air pollutant dispersion in a Dutch neighborhood using DALES". July 2024. URL: https://resolver.tudelft.nl/uuid:30518211-e812-4efe-98a1-ab7674024ed1.

[36] Cesar Goso and Gustavo Piñeiro. "An approach to coastline evolution as a tool for coastal management: case study of La Pedrera-Cabo Polonio Bay (Rocha, Uruguay)". In: *Journal of Sedimentary Environments* 5 (Dec. 2020). DOI: 10.1007/s43217-020-00034-3.

[37] Leo van Rijn. *Aeolian Sand Transport Processes, Part 1*. Dec. 23, 2023. URL: https://www.leovanrijn-sediment.com/papers/Aeoliansandtransport2018.pdf (visited on 11/13/2025).

[38] Thomas de Jong. *MSc-Thesis*. Version 1.0.0. Dec. 2025. URL: https://github.com/Thoms-J/MSc-Thesis.

[39] Di Wang, Eetu Puttonen, and Eric Casella. "PlantMove A tool for quantifying motion fields of plant movements from point cloud time series". In: *International Journal of Applied Earth Observation and Geoinformation* 110 (2022), p. 102781. ISSN: 1569-8432. DOI: https://doi.org/10.1016/j.jag.2022.102781.

[40] Weichen Dai et al. "LiDAR Intensity Completion: Fully Exploiting the Message from LiDAR Sensors". In: *Sensors* 22.19 (2022). ISSN: 1424-8220. DOI: 10.3390/s22197533. URL: https://www.mdpi.com/1424-8220/22/19/7533.

[41] Erich J. Plate and Harald Kiefer. "Wind loads in urban areas". In: *Journal of Wind Engineering and Industrial Aerodynamics* 89.14 (2001). Bluff Body Aerodynamics and Applications, pp. 1233–1256. ISSN: 0167-6105. DOI: https://doi.org/10.1016/S0167-6105(01)00159-3. URL: https://www.sciencedirect.com/science/article/pii/S0167610501001593.

[42] Titin Sundari, Boby Samra, and Agus Basri Saptono. "The Use of Wind Rose to Improve the Quality of Site Analysis". In: *IOP Conference Series: Earth and Environmental Science* 469.1 (Apr. 2020), p. 012017. DOI: 10.1088/1755-1315/469/1/012017. URL: https://doi.org/10.1088/1755-1315/469/1/012017.

[43] Douglas Sherman et al. "Measuring Aeolian Saltation: A Comparison of Sensors". In: *Journal of Coastal Research* 59 (Mar. 2011), pp. 280–290. DOI: 10.2112/SI59-030.1.

[44] Daniel Czerwonka-Schröder et al. "AImon5.0: Echtzeitüberwachung gravitativer Massenbewegungen - Eine Fallstudie am Trierer Augenscheiner". In: Feb. 2025.

[45] AdaptCoast and CoastScan. *AdaptCoast. Adaptive coastal monitoring in the Netherlands*. URL: https://coastscan.citg.tudelft.nl (visited on 11/09/2025).

[46] Livox. *Specs - Mid-70 LiDAR Sensor - Livox*. URL: https://www.livoxtech.com/mid-70/specs (visited on 11/04/2025).

[47] Ouster. *Velodyne Downloads — Ouster*. URL: https://ouster.com/downloads/velodyne-downloads (visited on 11/04/2025).